Welding in the World (2021) 65:1235–1306
https://doi.org/10.1007/s40194-021-01116-0

REVIEW ARTICLE

A review of high energy density beam processes for welding and additive manufacturing applications

T. Patterson[1] · J. Hochanadel[1] · S. Sutton[1] · B. Panton[1] · J. Lippold[1]

Received: 3 February 2021 / Accepted: 23 March 2021 / Published online: 20 May 2021

Abstract
High-energy density beam processes for welding, including laser beam welding and electron beam welding, are essential processes in many industries and provide unique characteristics that are not available with other processes used for welding. More recently, these high-energy density beams have been used to great advantage for additive manufacturing. This review of the literature serves to provide an overview of the evolution of the laser and electron beam processes including the fundamental nature of the beam itself and how such a high-energy density beam has been applied for welding. The unique nature of each process regarding weld bead formation and penetration, and metallurgical considerations are covered in detail. In addition, the evolution of monitoring systems for both characterization and control of these beam processes is reviewed. Over 500 references have been cited in this comprehensive review that will allow the reader to both understand the current state-of-the-art and explore in more detail the fundamental concepts and practical applications of these processes.

Keywords Electron beam welding · Laser beam welding · Additive manufacturing · Structural metals · Beam characterization · Process monitoring

1 Introduction

High-energy density (HED) beam processes are widely used in a variety of welding and additive manufacturing applications involving a wide range of materials. This section provides an overview of the HED processes including 1) the history of the development of electron and laser beams, 2) the nature and application of the HED beam processes, and 3) the metallurgical considerations that are important in the application of these processes. Section 1.1 discusses the history and evolution of the different processes, including major developments and benchmarks in the use of electron and laser beams for welding and allied processes. Section 1.2 discusses the nature of specimen beam interactions for both electrons and lasers. Finally, Section 1.3 reviews the metallurgical issues associated with HED beam welding including solidification behavior, grain orientation and growth, temperature gradient effects and microstructure-property relationships.

1.1 History and application of high-energy density (HED) beam welding processes

HED welding is utilized in a large number of industries spanning medical products to aerospace and defense. There are many advantages to HED processes when compared to arc welding processes as listed in Table 1. The main benefits include the ability to produce high depth of penetration at travel speeds greater than other fusion welding processes, thus substantially improving manufacturing productivity and reducing costs. The nature of the highly focused beams also allows for welds that are less than a millimeter in width for sensitive electronics or greater than 50 mm in depth in thick section components.

Although the electron beam welding (EBW) and laser beam welding (LBW) processes are similar in many ways, there are fundamental differences that influence process selection. Table 2 provides a comparison of EBW and LBW.

Recommended for publication by Commission IV - Power Beam Processes.

✉ T. Patterson
patterson.921@osu.edu

[1] Welding Engineering Program, The Ohio State University, Columbus, OH, USA

Table 1 Advantages and disadvantages of HED compared to other fusion welding processes

Advantages	Disadvantages
• Low heat input (<5 J/mm–20 kJ/mm) • Narrow heat affected zone • Deep penetration (>100 mm), • High depth-to-width aspect ratios (<1–25) • Reduced distortion • Non-contact/improved joint access • Joining of small components (electronics/medical devices) • High-energy transfer efficiency (80-90%) • Reduced/no consumable costs	• Precision part tolerances • High solidification rates (<0.1–>100 mm/s) leading to potential issues with cracking, porosity, and undesirable phase transformations • Difficultly in using filler material to improve fusion zone properties • Inspection (NDE) challenges • Higher initial equipment investment

Applications more conducive to EBW include its use on materials that are highly sensitive to oxidation/contamination where welding in a vacuum provides the best joint quality. Sections 1.1.1, 1.1.2, and 1.1.3 respectively describe the historical evolution of electron beam (EB) and laser beam (LB) and other uses of HED processes in manufacturing and material processing applications.

1.1.1 Evolution of the electron beam

Electron beams and EBW have roots dating back to the mid-to-late 19th century with studies of cathode ray tubes and eventually scanning electron microscopy [1]. The first studies of thermionic emission were conducted in 1853 [2]. This was over forty years before the discovery of the electron by Thomson [3]. Before this, electron beams were still studied by Hittorf and Crookes in 1869, when they were known as cathode rays. In 1879, it was seen that they could cause melting [4, 5]. The melting caused by the ray was seen as detrimental since the cathode ray tubes were being destroyed. However, in 1904 Pirani suggested that this heating could be used in a furnace. In 1906, he patented a gas-discharge tube electron beam which he used to join tantalum [1, 6]. For the next 25 years, generation of electron beams was confined to glass tube technology [1]. Busch theorized that the electron beam should follow the optics laws that dictate the behavior of light as he studied mathematics related to magnetic fields. A colleague by the name of Ruska experimented with the electron optics and was able to produce the first magnified image [1, 7, 8]. This advance was further developed by Brüche and Scherzer as documented in *Geometrische Electronoptik* [9, 10]. Only optical target glass images were produced prior to 1935 when the first images of solid samples of silicon iron were produced by Knoll using a scanning electron beam, as shown in Fig. 1.

During this same period, efforts to produce the first scanning electron microscope were underway. Transmission electron microscopy had already been developed, but the first modern scanning electron microscope that was able to focus an image to submicron levels was developed in 1938 by von Ardenne [4, 11]. He utilized the proposed electron optics

Table 2 Comparison between laser and electron beam welding

	EBW	LBW
Process	• High intensity beam of electrons	• High intensity beam of photons
Focusing	• Non-contact lenses • Large depth-of-focus • Electron beam is easily manipulated to various patterns	• Transmissive or reflective optics • Generally, smaller depth of focus • Beam manipulation requires electro-mechanical methods
Efficiency	• High efficiency of input power to electron beam generation	• Low electrical to laser conversion efficiency (maximum at ≈50%)
Material Interaction	• High coupling efficiency between electrons and metals (80-90%) • Negligible influence of surface preparation • Influenced by external or residual magnetic fields	• Reflectivity issues between photons and conductive metals • Influenced by surface preparation • Not influenced by magnetic materials or fields
Environment	• Welds are typically performed under high vacuum (< 10^{-4} torr). • Welds at low vacuum significantly attenuate the electron beam	• Welds are easily performed in atmosphere with or without shielding gases, or under vacuum • High power requires appropriate plume suppression
Safety	• Generation of harmful X-rays requires adequate shielding	• No x-rays generated • Damaging to eyes and/or bodily tissues
Cost	• High initial investment	• Moderate initial investment

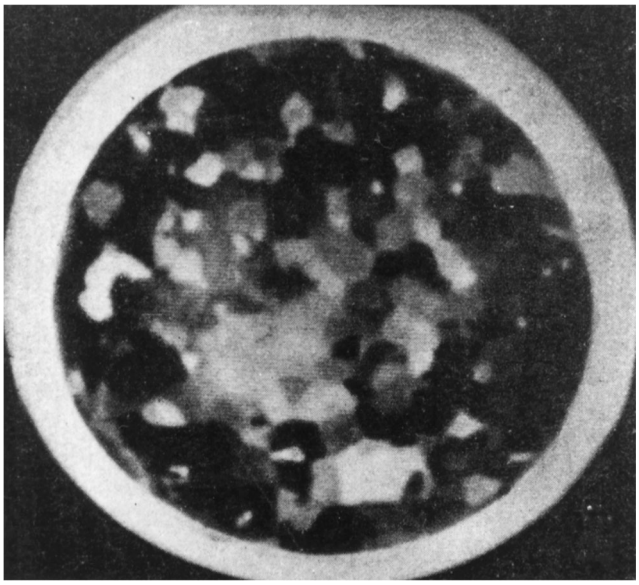

Fig. 1 Early image of silicon iron, Knoll 1935 [4]

lenses to focus the beam down to a very small diameter, resulting in high magnification.

Nearly a decade later in Germany, the "father of electron beam welding," Karl Steigerwald (Fig. 2) was working with electron optics and high-power electron sources. He developed a far-focusing source and, by mistake, made a hole in a platinum aperture. Seeing this, he began "engraving" material. This "engraving" was actually the first reported bead-on-plate electron beam weld [1]. An example is shown in Fig. 3. A photo of an early electron beam welding machine developed by Steigerwald is shown in Fig. 4.

Fig. 2 Dr. Karl Heinz Steigerwald, the father of electron beam welding, c. 1968 [1]

This electron beam engraving/drilling process was patented, and an American broker and metallurgist by the name of Rossi bought the patent and began working with Steigerwald to produce electron beam drilling machines. Shortly after this, in France, Stohr was working with X-ray manipulation when he produced a deep penetration weld [1]. Once he observed this, he decided to join zirconium alloys using an electron beam so that it would avoid oxidation in the vacuum (Fig. 5). In 1956, he produced the first machine designed to weld [12].

From 1956 to 1974, only diode electron gun designs were developed. However, in 1974, Lawrence patented a triode gun design for electron beam welding [13]. The use of a triode became the standard, and most modern welding systems today use a triode design. The beam was not able to be measured until 1977, when a patent was filed by Vaughan [14]. In 1993, Elmer et al. [15] published results for improved electron beam distribution measurements using the modified Faraday cup with a patent following in 1995 [16], which evolved into the enhanced modified Faraday cup in 2001 [17].

Many of the major advances in the development of electron beam welding machines occurred shortly after World War II. The machines progressively gained efficiency, the vacuum levels improved, and were integrated with computer numerical control (CNC) in the 1980s. However, the basic principles in the operation of the EB machine itself remained largely the same as the machines from the 60s and 70s, many of which are still in operation today [1]. A timeline for the development of electron beams and EB welding machines is provided in Table 3. For further reading on the history of the development of EB welding machines, the reader is referred to References [1, 4, 19].

1.1.2 Evolution of the laser

The concept of stimulated emission and absorption of radiation was first presented in a paper by Albert Einstein in 1916 [20]. By the 1950s, numerous researchers were simultaneously working on converting the stimulated emission theory to application. This initially evolved into the creation of microwave amplification by stimulated emission of radiation (MASER) named so for the frequency of electromagnetic waves produced. A Nobel prize was awarded in 1964 to Charles H. Townes and Alexander Prokhorov/Nikolai G. Basov on their independent work developing the MASER. Figure 6 shows Townes on the left standing next to the ammonia maser system he developed [21, 22]. There is debate as to whether the first laser was designed by Charles Townes or Gordon Gould; the latter is believed to have first created the term light amplification by stimulated emission of radiation (LASER) and designed a laser system containing a Fabry-

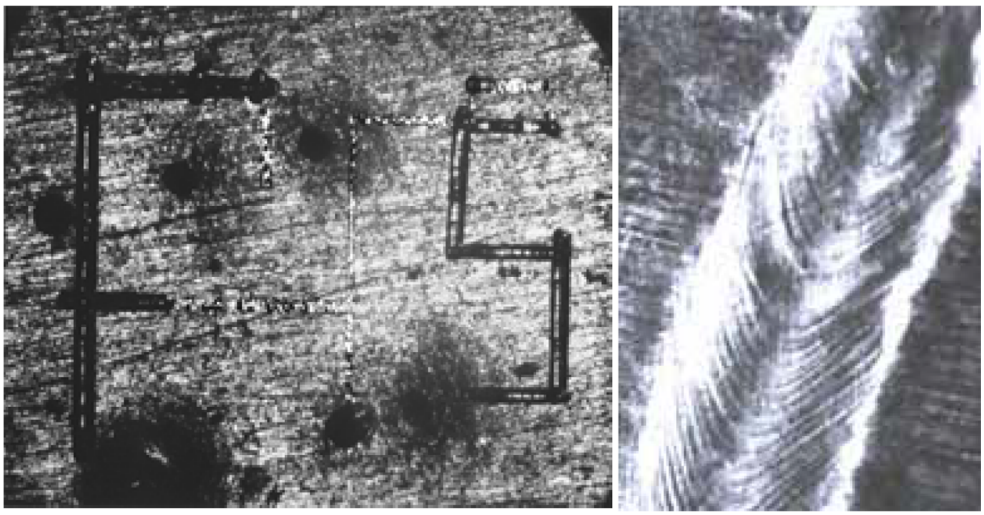

Fig. 3 First electron beam weld, a bead-on-plate engraving produced in 1949 [1]

Pérot resonator cavity. Gould's initial patent application was in 1959 [23]; however, this was after Townes had already applied for a patent in 1958 describing the production of infrared radiation [24, 25]. After legal battles, Gould was finally granted recognition for his work [23, 26]. Although, it was Theodore Maiman who first produced practical amplification of light using a ruby crystal (Al_2O_3 doped with Cr_2O_3) [27]. A photograph of this laser is shown in Fig. 7 [22]. The ruby rod was housed within a coiled flashlamp that was encapsulated in a reflective aluminum cylinder [28]. The late 1950s and 1960s were an important time period for development of fundamental laser technology with gas, diode, and fiber active mediums initially theorized, constructed, and analyzed for feasibility. These early developments in laser production have significantly advanced over the last half century. Table 4 shows the major chronological events in laser development leading to the current material processing technologies and applications.

Fig. 4 Lab prototype of an electron beam welding machine, 1951 [1]

After helium-neon gas lasers failed to make continued improvement in power gains, Kumar Patel at Bell Telephone Laboratories analyzed transitions of molecules to develop the carbon dioxide (CO_2) laser [39, 47]. Patel also discovered significant benefits by adding nitrogen [48] or helium, oxygen, and/or water vapor to the CO_2 gas [47]. By 1965, Patel et al. [49] reported a continuous wave (CW) output power of 105 W with 6% conversion efficiency emitting at a wavelength of 10.6 μm. Figure 8 shows Patel next to a CO_2 laser in 1967. These initial gains and significant advantages spurred a growth in CO_2 lasers for industrial material processing applications, and commercially produced CO_2 lasers eventually reached maximum CW output powers of 50 kW [50]. For decades, CO_2 dominated the laser cutting and welding markets until the creation of the disk laser and further development of the fiber laser. A significant drawback with CO_2 lasers is the generation of the 10.6 μm wavelength that is highly reflected by most metals and does not allow for high power transport through glass optical fibers. For more information on reflectivity, the reader is referred to Section 3.1.3 and Fig. 55.

In the same year as the CO_2 laser discovery, Geusic et al. [40] reported development of the neodymium doped yttrium aluminum garnet (Nd:YAG) lasing medium. The Nd:YAG rod laser eventually made its way into welding applications requiring lower average powers and, particularly, where beam delivery through an optical fiber and/or pulsed welding was possible. However, the original flashlamp pumped Nd:YAG

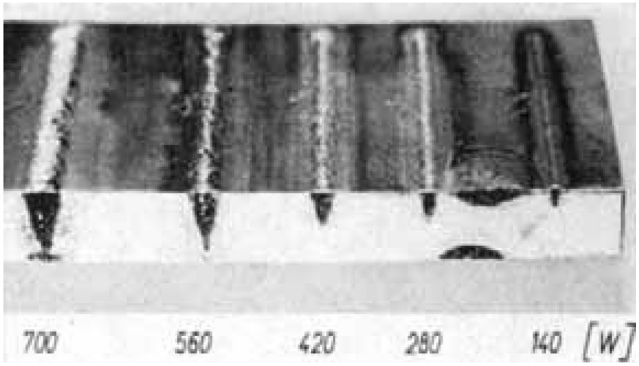

Fig. 5 First deep penetration welds in a Zircalloy plate, 1958 [1]

rod lasers were limited in their potential due to poor flashlamp pumping efficiencies and minimal power output. The power limitation is due to the inability to sufficiently cool the rod-shaped crystal. For more detail on laser operation and a description of pumping, the reader is referred to Section 3.1.

In 1992, Giesen et al. [43, 44] modified the YAG rod geometry to produce a thin disk that enabled efficient, through-thickness heat extraction by applying cooling to a single face on the disk. Along with diode pumping, this substantially improved the efficiency and the ability to generate higher output power. This was the original development of the disk laser that currently competes with fiber lasers for market share in welding applications. By 2012, disk lasers were commercially available that produced 6 kW of power from a single disk design [51, 52].

Poor pumping efficiencies were understood in the early years of laser development, and the potential for GaAs diodes to pump a Nd:$CaWO_4$ laser was originally proposed by Newman in 1962 [38]. A year later, Keyes and Quist [53] reported analyzing diodes to pump a CaF_2:U^{3+} laser and a possibility of 50% electrical conversion to pump radiation. A representation of this transversely pumped laser-diode configuration is shown in Fig. 9 [53].

Diode pumping further progressed as a source for pumping Nd:YAG crystals as shown in Fig. 10 [54], and diode pumped Nd:YAG lasers were commercially available in 1984 [55]. The selective pumping with a narrow band of wavelengths at the absorption bandwidth of Nd^{3+} allowed for reducing heat generation and improving pump light conversion efficiency. However, these initial diodes were limited in application. This limit was caused by low output powers and the need to cool the diodes to cryogenic temperatures. Continued evolution of diode technology led to significant pumping improvements and now diode pumping outperforms flashlamp pumped solid-state lasers. The rise in fiber laser technology is attributed to improvements in diode lasers and diode lifetimes, reported to be as high as 100,000 h of operation [46]. By the early 2000s, diode pumping enabled solid-state lasers to become competitive with high-power CO_2 lasers [55]. Increases in diode output power and efficiency are necessary for reducing costs in diode pumped disk lasers, and as of 2020, single diode bars are reported to produce as high as 300 W of continuous power [56].

Table 3 Timeline of events leading to the development and improvement of the electron beam welding process

Date	Name	Achievement	Reference
1853	Becquerel	First studies of thermionic emission	[2]
1869	Hittorf and Crookes	Utilized electrons in the form of cathode ray tubes	[4]
1879	Hittorf and Crookes	Cathode ray used to melt	[4, 5]
1897	Thomson	Discovery of electrons	[3, 18]
1904	Pirani	Proposed the use of electron beam as a heat source	[1]
1906	Pirani	Patented gas-discharge tube electron beam to join tantalum	[1, 6]
1906	De Forest	First triode design of a cathode ray tube	[1]
1926	Busch	Theorized electron optics by studying magnetic field mathematics	[1, 7]
1931	Ruska	First experiments with electron optics, forming a magnified image	[1, 8]
1934	Brüche and Scherzer	Published *Geometrische Elektronoptik* detailing systematic experiments of lenses	[10]
1935	Knoll	First images of solid samples using a scanning electron beam	[4]
1938	Von Ardenne	First scanning electron microscope to use magnetic lenses and produce a sub-micron probe	[4, 11]
1949	Steigerwald	First electron beam drilling and welding	[1]
1952	Steigerwald and Rossi	First electron beam drilling machine produced	[1]
1954	Stohr	First deep penetration welds	[1]
1956	Stohr	First machine designed for electron beam welding	[1, 12]
1974	Lawrence	Patented a triode gun design for electron beam welding	[13]
1978	Vaughan	Patent of a device for electron beam diameter measurement	[14]
1995	Teruya and Elmer	Patent to tomographically measure electron beam distribution	[16]

Table 4 Major achievements leading to the development of lasers and laser welding

Date	Name	Achievement	Reference
1916	Einstein	Theorized light and stimulated emission	[20, 29]
1927	Ladenburg	Showed that stimulated emission was possible	[30]
1953	Weber	Publication describing function of the MASER	[31]
1954	Townes and Gordon	First demonstration of a MASER	[32]
1957	Gould	Developed the term laser and sketches his idea for a design containing a resonator cavity. Initial patent application followed in 1959.	[21, 22]
1958	Schawlow and Townes	Article describing the extension of MASER techniques to higher frequencies (infrared region)	[25]
1960	Schawlow and Townes	First patent (Patent No. US 2,929,922) describing the MASER	[24]
1960	Maiman	Produced amplification and working laser using a ruby crystal housed within a flashlamp	[27]
1960	Javan et al.	Invented the first continuous wave helium-neon laser	[33]
1961	Snitzer	Development of fiber laser doped with Nd^{3+} ions	[34]
1962	Hall et al.	Demonstration of coherent light emission in a Ga-As p-n junction (diode laser). First demonstrations of direct conversion of electrical energy to coherent radiation	[35]
	Nathan et al.		[36]
	Quist et al.		[37]
1963	Newman	Recognized pumping Nd^{3+} ions via GaAs diodes	[38]
1964	Townes	Received Nobel prize in physics for their independent work on developing the MASER	[32]
	Prokhorov and Basov		[22]
1964	Patel	Invention of the CW CO_2 laser at 9.6 and 10.6 μm wavelengths	[39]
1964	Geusic et al.	Invention of the Nd:YAG laser at a 1.06 μm wavelength	[40]
1964	Snitzer and Koester	Analyzed first fiber laser amplification	[34, 41]
1985	Poole et al.	First reported CW output from a single mode, diode pumped Nd^{3+} fiber laser	[42]
1992	Giesen et al.	Invention of diode pumped Yb:YAG disk laser	[43, 44]
2000	Gapontsev	Invention for coupling multi-mode pump light into a single mode fiber (Patent No. US 5,999,673)	[45]
2004	Gapontsev	Fiber lasers produce total power of 10 kW at wall plug efficiencies of nearly 20%	[46]

Besides pumping, diode technology evolved into high-power diode lasers (HPDLs) that are directly used in material joining applications. Soldering was one of the earliest direct diode joining applications and was reported in 1991 [57]. Higher powers are produced through fabrication of diode "bars" that are an array of diodes arranged on a single chip [58, 59], and to further increase the output power, bars are stacked together forming arrays or diode "stacks" [55]. During the 1990s, another method of increasing overall diode output power was introduced by coupling the diode output from a single emitter or bars into individual fibers that are combined to a single delivery fiber [59, 60]. Arrays and stacks of diodes have inherently poor beam shapes requiring manipulation of the output light. One of the earliest beam shaping approaches was reported by Clarkson and Hanna [61] in 1996, which produced circular spots from high-power diode bars.

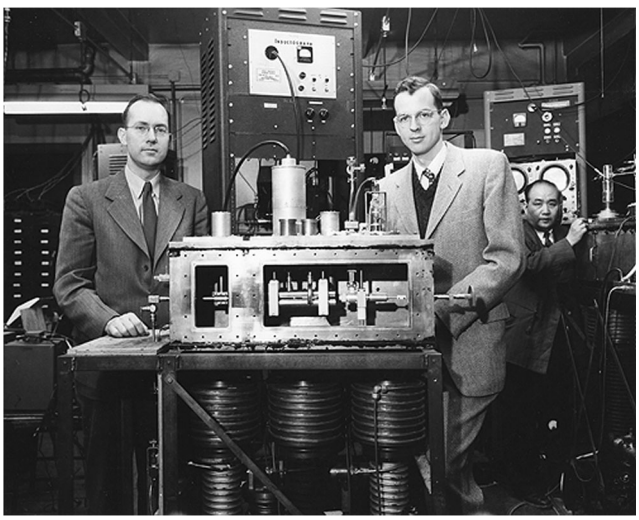

Fig. 6 Charles Townes (left) and James Gordon (right) standing next to the ammonia MASER [21]

The idea behind light transport through a waveguide of low refractive index material preceded maser development, but in 1961, Snitzer [34, 62] published a theory on transmitting a single electromagnetic mode through a thin glass fiber. However, excessive attenuation in the early fiber designs made them not practical for application. Keck and Schultz [63] filed a patent in 1973 for production of optical waveguides with acceptable levels of attenuation. About 20 years later, optical fiber designs evolved rapidly with the expanding telecommunications industry.

Multiple variations of the fiber lasers were developed based on dopants, methods of pumping, and pulsing, but there was minimal improvement in output power for nearly two decades. It was not until 1989 that Wyatt [64] produced over

Fig. 7 First laser containing a ruby crystal developed by Theodore Maiman (left) [28], and Maiman behind a larger variation of the original laser (right) [22, 28]

250 milliwatts of power from a Ti:sapphire pumped Er doped fiber laser. A year earlier, Snitzer et al. [65] reported the development of double-clad fibers containing an offset, single mode core shrouded within a multi-mode pumping fiber. This improved coupling efficiency of pump light enabled low brightness beams to produce a high intensity, single mode beam [66]. In 1994, Gapontsev and Samartsev [45] patented the technology for side pumping a single mode fiber with multi-mode pump light. This enabled significant scaling of power because numerous locations along the fiber could be injected with pump light. Significant power improvement was continued by Gapontsev and the IPG Photonics Corporation. In 2004, Gapontsev [46] reported fiber lasers with a total power of 10 kW by combining individual laser modules to scale single fiber output, and the first commercially available single mode 10 kW laser was available from IPG Photonics® in 2009 [67]. At the time of this writing, fiber lasers are commercially available with power outputs in excess of 100 kW

Fig. 8 Photo of Kumar Patel standing next to a CO_2 laser in 1967 [22]

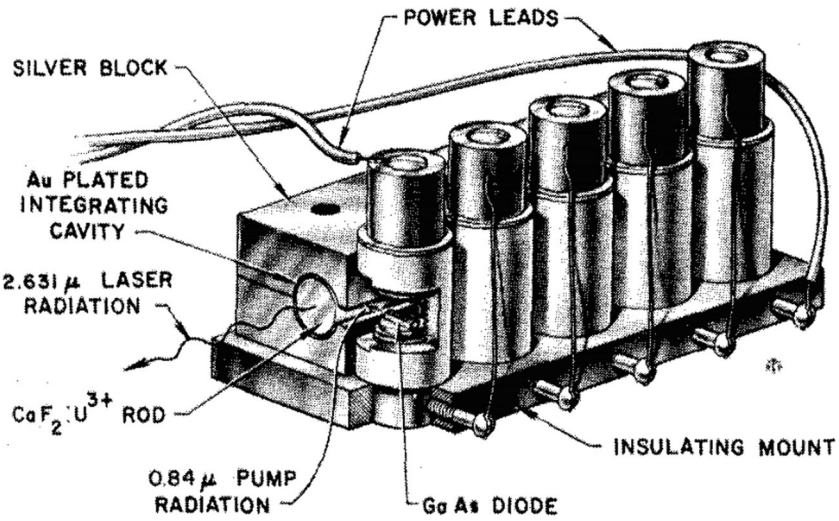

Fig. 9 Drawing of GaAs diode pumped $CaF_2:U^{3+}$ laser published in 1963 [53]

with weld research published in 2018 by Kawahito et al. [68] using a 100-kW fiber laser.

1.1.3 Hybrid laser-arc welding

Hybrid laser-arc welding (HLAW) is a process that brings together laser and arc welding, in order to attain a combined advantage of the two welding methods. In most cases, the gas metal arc welding (GMAW) process is used in conjunction with the laser. According to Ribic et al. [69] synergy is achieved through interaction between the arc and the plume of ionized plasma created by metal vaporization during lasing, creating a path of least resistance to create the laser keyhole. This phenomenon allows for a high-energy density welding process with double the energy density of a standard arc process while maintaining a low heat input per unit length of weld. The low heat input generated by HLAW has many benefits including reduced residual stresses [70] and distortion [71] when compared to a standard arc welding process. HLAW also retains the primary weld pool characteristics of both methods, creating a "wine-glass" shape [72] by the dominance of the arc in the upper portion of the weld and the laser in the lower portion. In addition to lower heat input, the incorporation of the laser allows for greater weld penetration, thereby increasing the range of thicknesses that can be welded in a single pass and reducing the need for multi-pass welds [72,

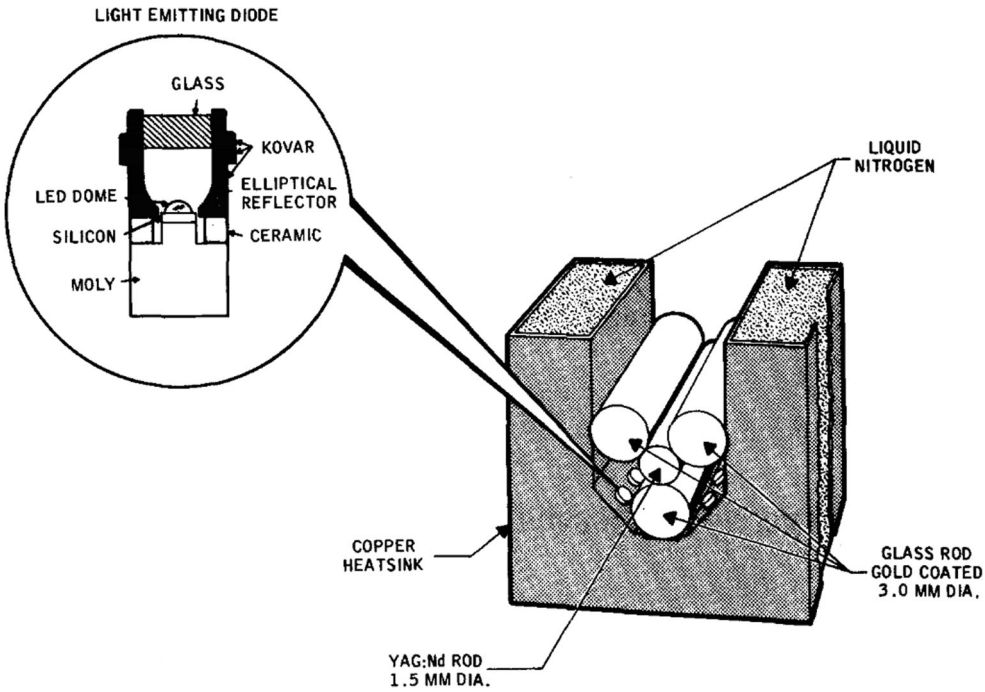

Fig. 10 Configuration of Nd:YAG laser being pumped with an array of $GaAs_XP_{1-X}$ diodes [54]

73]. The arc provides a widened upper portion of the weld pool, increasing the ability to bridge gaps in the weld joint, and relaxing fit-up tolerances when compared to standard HED processes. Unlike most HED processes, inclusion of filler metal is standard with HLAW, allowing for greater range of alloys that can be welded. Inclusion of process monitoring systems for both arc and laser is also feasible for HLAW, allowing for greater process control. HLAW is currently seeing increased adoption as the primary welding method in several industries, including naval construction, where increased penetration and reduced distortion are desirable.

1.1.4 HED additive manufacturing

Additive manufacturing (AM) is a very broad term and consists of seven main processes, namely 1) vat photo-polymerization, 2) material extrusion, 3) material jetting, 4) binder jetting, 5) sheet lamination, 6) powder bed fusion, and 7) directed energy deposition [74]. Lasers and electron beams are used primarily in the last two processes and are discussed. Examples of some metallic AM parts are provided in Fig. 11.

Powder bed fusion Powder bed fusion (PBF) is a process conducted in a chamber in order to deposit the powder material in a layer-by-layer fashion. The electron or laser beam rasters across the powder layer which causes melting and fusion, as shown in the schematic in Fig. 12. This is repeated for each layer until the part is completely built, after which the remaining powder is cleaned off and the part is extracted. This process was introduced in 1986 by Carl Deckard at UT-Austin under the name "selective laser sintering", and was patented in 1990 [77]. Arcam AB developed the electron beam process in 1993 [78].

Using powder bed fusion, complex structures can be made. The beam can focus to 100 microns in diameter or less, and the powder is typically on the order of tens to hundreds of microns in diameter. This allows for high precision and very fine features in the manufacturing of parts. Due to the simplicity of computer aided design (CAD) file conversions, rapid prototyping is also a key advantage. Fully dense parts are achievable with this process, and high strength and stiffness of the parts can be attained [74, 76, 79, 80].

Some disadvantages to PBF include limitations on part size, deposition rates, additional costs relating to powder, startup costs, the presence of defects (cracks, porosity), and potential health hazards resulting from the use of fine powders. The size of the chamber is limited by constraints of the beam being rastered. Laser beam systems (LB-PBF) utilize galvanometers to scan the beam, and electron beam systems (EB-PBF) utilize magnetic deflection coils. In order to maintain beam focus while scanning the beam without altering the power distribution, it must stay in a restricted workspace envelope. Furthermore, as chamber size (part size) increases, more powder is required to fill the powder bed which greatly increases the cost per part. Finally, since the layers being built are generally less than a millimeter in thickness, build times are long. Higher beam powers and deposition rates can result in significant part heating. Therefore, parts made using this process are usually quite small. Health risks include metal powders, which can be highly reactive and easily respirable, and, in the case of EB-PBF, X-ray generation [76]. The advantages and disadvantages of EB-PBF and LB-PBF are listed in Fig. 13.

Powder is made by atomization, commonly done in a gas, water, or plasma medium. Gas atomized powders are typically the preferred feedstock for AM. This is because they are highly spherical, which leads to better feedability properties [81–83]. Water atomized powder is more common since it is less expensive, but it leads to irregular particles which can be detrimental for packing density and feedability and can result in a number of defects [81]. Depending on the method of manufacture, powders can contain entrapped gases that produce porosity in the AM parts. Powder can be recycled, but typically virgin powder is desired to avoid contamination and avoid heat-to-heat differences in composition among manufacturers.

Although LB-PBF and EB-PBF are very similar processes, two major differences result in much different processing conditions: atmosphere and scanning strategy. Since EB-PBF is done in vacuum and LB-PBF is typically done in an inert atmosphere, cooling rates are different by up to an order of magnitude [84]. The scanning strategy for EB is much faster than for LB, reaching up to 8 km/s [83]. This results in the ability to preheat to a much higher temperature by rastering the beam rapidly before the fusion pass. It also allows for pre-sintering of the part, resulting in fewer support structures that may be required for large or complex parts. Also, EB-PBF is only applicable to electrically conductive materials; whereas, LB-PBF can be used for a larger range of materials, including polymers [76]. EB-PBF also produces more surface roughness and reduced feature resolution, as compared to LB-PBF [81].

Directed energy deposition Directed energy deposition (DED) is analogous to multipass welding and is mainly used for functionally graded materials, metal-matrix composites, and coatings or cladding [85]. It involves melting of a deposited wire or blown powder using a beam or an arc. Each pass fuses the deposited feed stock to the previous pass, which continues until the part is completely built. The first report of DED was in 1920 when Baker filed a patent, illustrating a pitcher and a basket made using DED, as shown in Fig. 14 [86]. It was not until 1970 that DED reemerged to build variable composition metal pressure vessels [87]. In the 1980s, advances in lasers and computer control systems allowed for

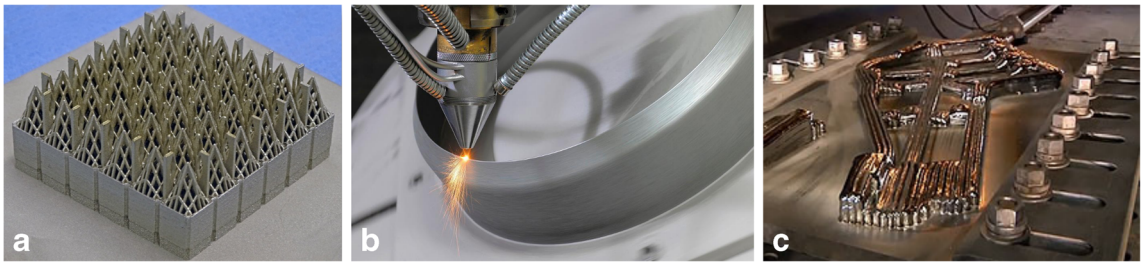

Fig. 11 Examples of metallic AM parts: Westinghouse powder bed fusion (a), LENS™ powder-blown directed energy deposition (b), Sciaky wire-fed directed energy deposition (c) [75]

further progress, and in the mid-1990s, powder-blown DED was developed [78]. It was not until 2009 that Sciaky Inc. patented the current technology for EB-DED [88].

DED allows for much higher deposition rates and larger parts [76] since a powder bed is not required. It should be noted that for EB-DED, a vacuum chamber is generally used, and this chamber is usually relatively large to allow for large builds. Utilizing CNC, the part can be moved under the beam, reducing the restriction on part size. It can also be used to modify or repair existing parts, including cladding [85]. The parts still can be complex in shape relative to traditional manufacturing methods. Much can be inferred about DED because of the extensive research on multipass welding for a wide range of materials. In general, if the material is weldable, it is probably a good candidate for DED. Schematic illustrations of DED using laser and electron beam energy sources are shown in Fig. 15.

Some disadvantages of DED include costs, metallurgical defects, health hazards, reduced precision and complexity of structures, post-processing requirements (e.g., machining), microstructural anomalies, and residual stresses/distortion. DED systems are expensive with the cost increasing significantly as the build envelope increases. Similar health concerns exist in DED as with PBF, especially when working with powder feedstock or when using EB-DED. When using wire feed, post-processing in the form of machining is almost always required. The DED process uses much higher heat inputs than PBF, and when combined with multiple reheats from increasing layers, this results in large grain structures and a higher propensity for distortion. This can be alleviated with heat treatments depending on the build material. The advantages and disadvantages of LB-DED and EB-DED processes are listed in Fig. 16.

Powder-fed DED is only currently available in laser systems, including laser engineered net shaping (LENS™), which was developed at Sandia National Laboratories [90]. The use of a powder feed can achieve much smaller details and better surface quality than wire feedstock. Therefore, it is known as "net shaping" since the part will require little or no post-processing. Wire-feed DED is known as "near-net shaping," which means that the part is close to the final design but will have to be further processed to achieve the desired shape. Powder-blown processes have much lower deposition rates than wire-fed, and normally do not exceed 1 kg/hr [78, 91]. Wire feed can achieve deposition rates of up to 18 kg/h. However, this also increases heat input and therefore has a

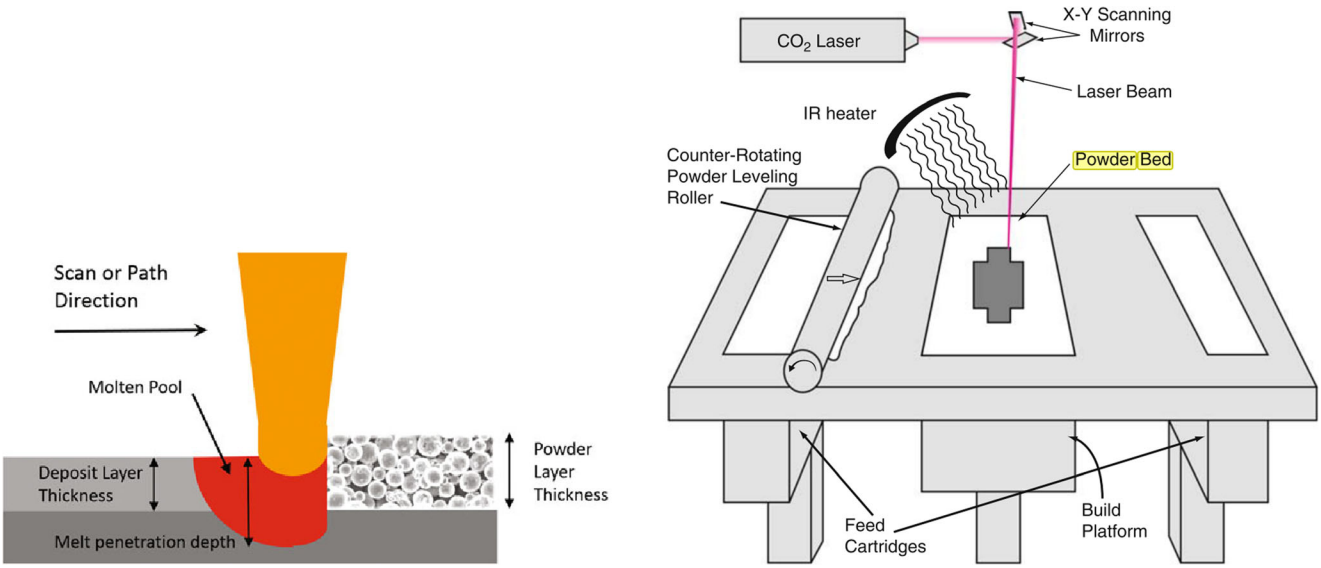

Fig. 12 Laser powder bed fusion schematics [74, 76]

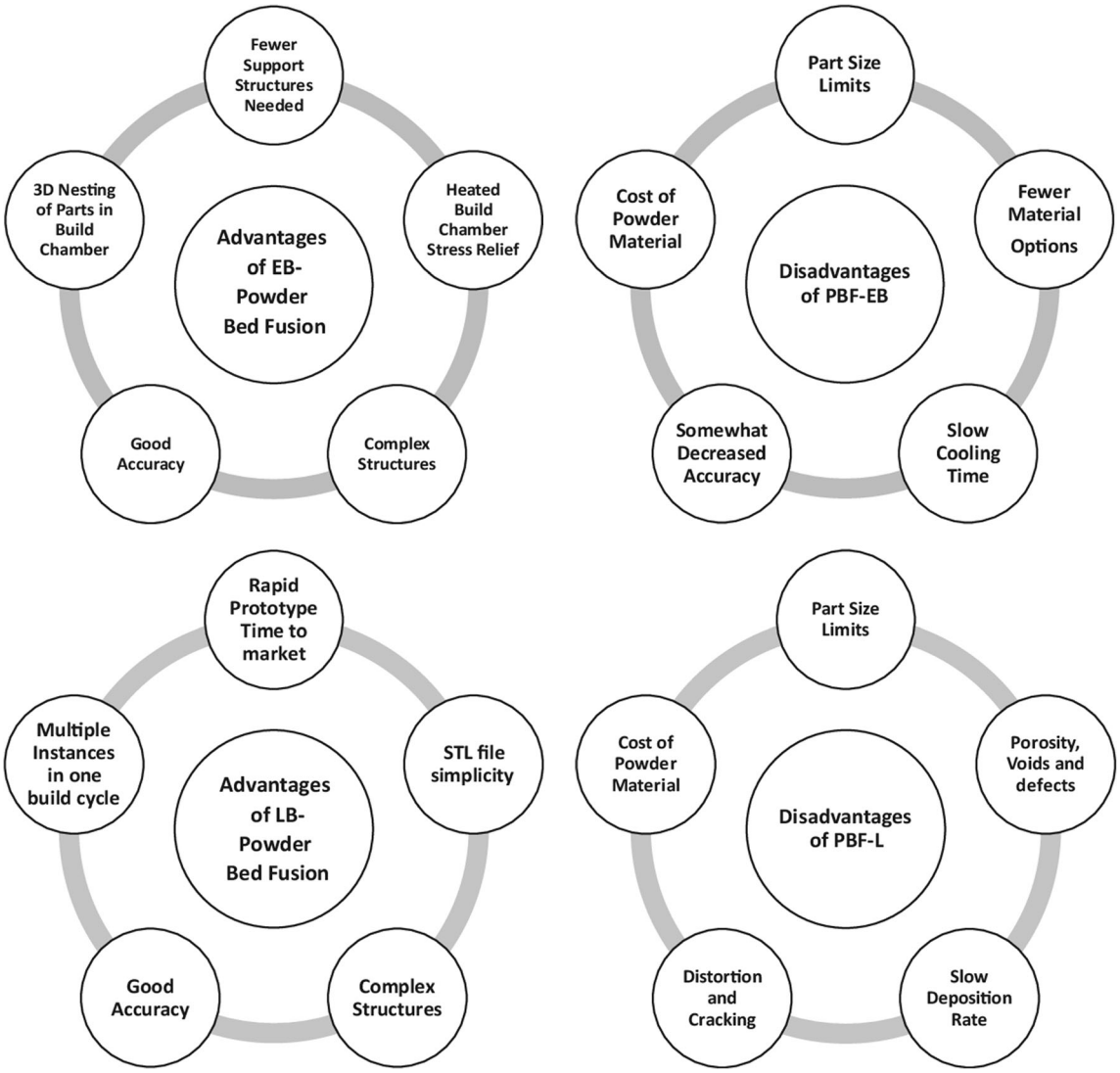

Fig. 13 Advantages and disadvantages of EB-PBF and LB-PBF [76]

detrimental effect on distortion and microstructure; whereas, the powder-blown systems can have much better control over these issues.

EB-DED and LB-DED require different operating environments. Since LB-DED is usually performed in inert atmospheres, cooling rates are faster. However, highly reactive

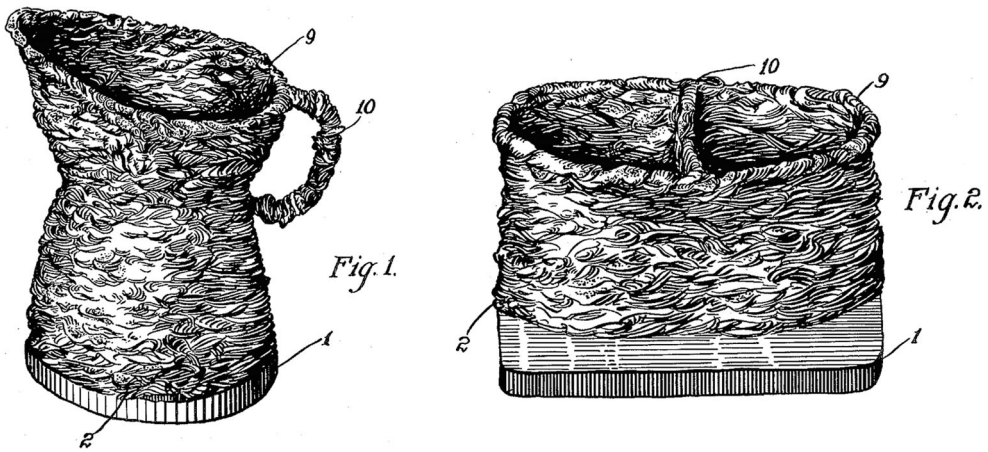

Fig. 14. Baker's illustrations of AM pitcher and basket, 1926 [86]

materials such as titanium alloys are more suitable for EB-DED since the high vacuum reduces reactivity with the atmosphere. Only wire feedstock is used in EB-DED because powder feedstock causes issues in a vacuum environment.

A significant issue with both PBF and DED processes is the presence of defects and microstructural anomalies in the parts that are built. Similar defects can be observed in both PBF and DED, and include lack of fusion, porosity, loss of alloying elements through vaporization, and cracking or delamination [84, 92]. Surface roughness can also be considered a defect; although, this can be remedied by post AM processing. Lack of fusion is a result of powder not being fully melted and/or fused to the underlying layer. This usually results from too low of a power density, a non-optimized scanning strategy, or a combination of both. Porosity can be the result of a keyhole that forms in the build or gas trapped in the molten metal. Typically, additive manufacturing uses the conduction mode to melt each layer [74, 76, 78, 84, 89]. Using too high a power density can result in a keyhole, and the keyhole can become unstable, resulting in porosity. Gas porosity can occur from unclean powder being melted, resulting in the formation of gas bubbles during solidification. This can usually be controlled by controlling powder quality. Porosity concerns are one reason that powder is not reused. Other reasons include alteration of particle shape, size, and flowability as well as composition variations [93].

Loss of alloying elements can occur during each pass and is directly related to power density. This results from preferential vaporization of certain elements in the material. The local change in composition can affect the microstructure, and therefore, its mechanical and corrosion properties. For example, preferential vaporization of chromium in stainless steels may reduce the corrosion resistance of the part. Finally, cracking occurs for the same reasons as in welding. This can be in the form of solidification cracking, liquation cracking, or delamination. Since each layer behaves essentially as a single pass in a multipass weld, the cracking mechanisms are relatively well understood since they are analogous to those during welding. Some examples of defects occurring in additively manufactured components are shown in Fig. 17.

1.1.5 Other applications of HED beams

Electron and laser beams have a significant advantage over other energy sources for providing high incident energy density and allowing rapid processing speeds. These benefits have revolutionized technological advancements in many material processing applications including brazing, cutting, drilling, transformation hardening, and cleaning. The following sections provide brief descriptions and further references for these material processing applications that involve HED beams.

Brazing HED brazing is conducive to joining dissimilar metals because of high efficiency noncontact heating. Laser brazing was used in automotive applications as early as 1997 [95, 96]. The Nd:YAG lasers used in brazing applications were eventually outperformed by more efficient disk, fiber, and diode lasers. Variations of the laser brazing process include tandem laser brazing reported in the early 2000s. This utilizes one laser to heat the substrate and another laser to melt the brazing filler metal. The tandem process was reported to produce superior wetting through laser preheating [97, 98]. The latest advancement in laser brazing uses beam splitting technologies to produce multiple spots such as two lead spots to ablate galvanic coatings and improve quality and processing speeds. A schematic of this beam splitting process is shown in Fig. 18. Reimann et al. [99] showed improvements in braze quality using a trifocal beam to vaporize zinc on galvanized steels. Automotive industry applications are a major opportunity for laser brazing with ongoing interest in brazing zinc coated steels [96, 99, 100] and for dissimilar combinations such as aluminum-to-steel and magnesium-to-steel [101].

Cutting Electron beam cutting was under development as early as the 1960s with an initial patent for an EB cutting control device filed in 1962 [102]. However, electron beam cutting applications are limited in application [89]. This is due to high equipment costs and the need for vacuum environments, components free of magnetic fields, and electrical conductivity.

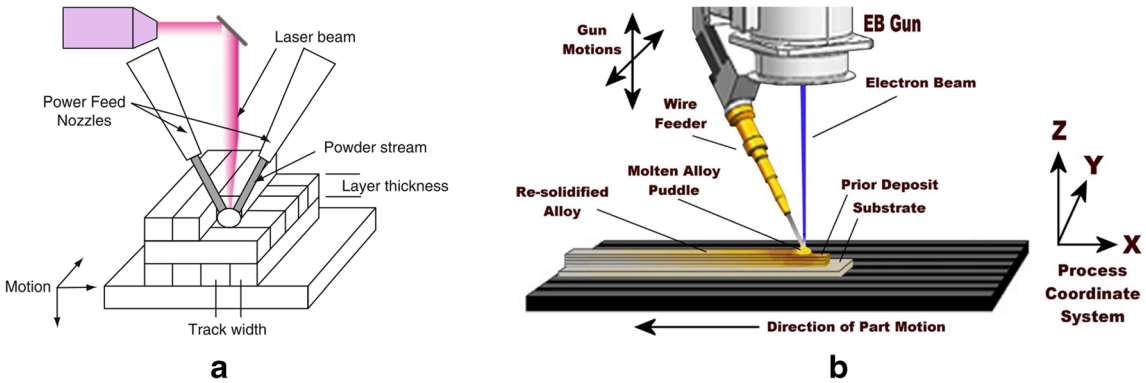

Fig. 15 Schematics of powder-blown DED (a) [74] and Wire-fed EB-DED (b) [89]

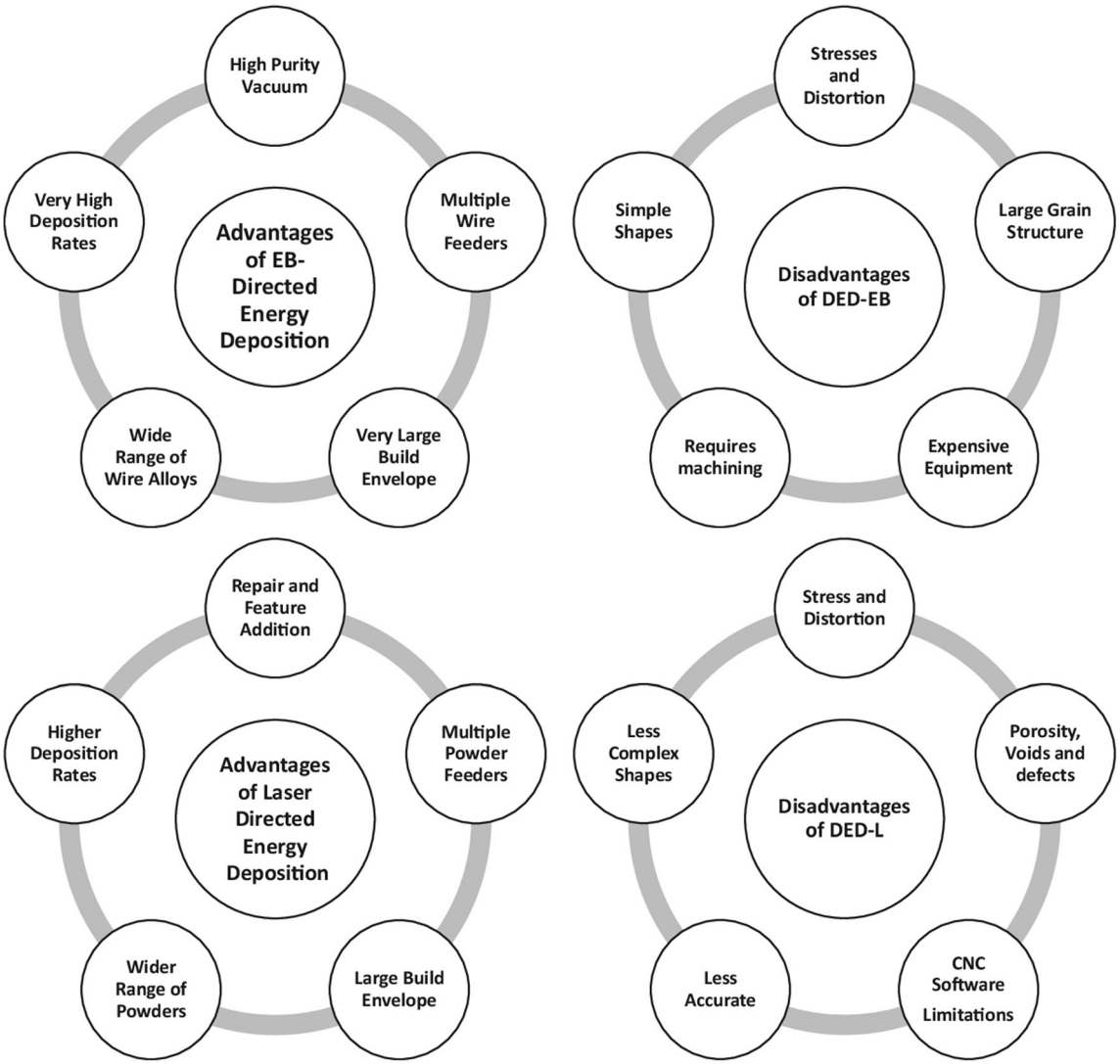

Fig. 16 Advantages and disadvantages of EB-DED and LB-DED [76]

These issues are effectively eliminated with cutting methods involving lasers.

The most common industrial application of lasers is for cutting rather than welding. In 1967, CO_2 laser cutting with oxygen assist gas was demonstrated at The Welding Institute (TWI) by Sullivan and Houldcroft [103]. Photos of the laser cutting setup and operation at TWI are shown in Fig. 19 [104]. The benefits of lasers compared to other processes include high cutting speed, narrow kerf width, easy automation, limited dross, no tool wear, narrow heat affected zone (HAZ), and the ability to cut nearly all materials [105–107]. It is common to utilize a coaxial assist gas (air, oxygen, or inert) to aid in material removal and protect laser optics when cutting metals. Numerous lasers are used for cutting including: CO_2, Nd:YAG, excimer, diode, disk, and fiber. Generally, shorter wavelengths lead to improved cuts unless there is an issue with maintaining comparable beam quality between different laser sources [106].

Laser cutting of metals was initially limited to the thickness range of 15–25 mm [107, 108]. In the late 1990s and early 2000s, dual focal optics [109] and assist gas cutting with oxygen was improved, both of which allowed deeper cuts and enhanced cut quality [108]. The dual focus system was reported to improve cut speed, cut depth, process stability, and reduce/eliminate dross formation [109, 110]. A variant to this design was initially patented in 1991 by producing two focal positions split horizontally from the beam axis for welding butt joints [111]. The advancement of assist gas was performed by O'Neil and Gabzdyl [108] who reported cut depths as high as 50 mm. This process was referred to as laser-assisted oxygen (LASOX) and utilized a larger beam diameter than the oxygen gas jet diameter. The purpose of this is to maximize the oxidation reaction and consume all the available

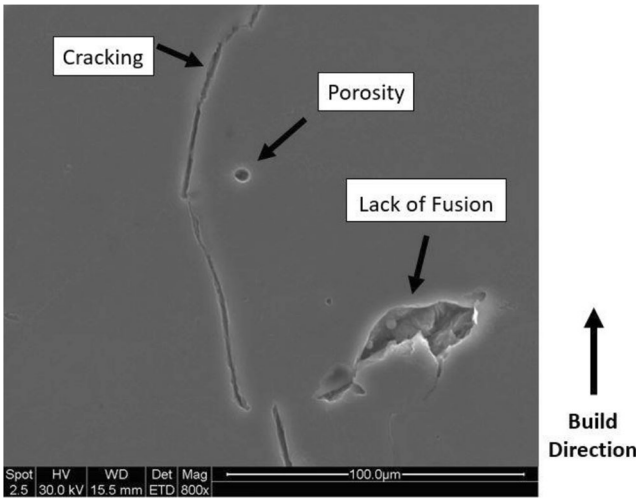

Fig. 17 Examples of the different types of welding related defects found in AM parts [94]

oxygen to aid in higher heat input and increase cutting efficiency.

The latest improvements in laser beam cutting (LBC) involve conversion from CO_2 to disk and fiber lasers that offer better wall plug efficiencies and improved beam quality at comparable powers. In 2011, TRUMPF® announced the development of a single delivery fiber containing two concentric fibers for transporting different beam intensities to the optics [112]. This enables a multi-purpose machine to rapidly switch from high intensity laser cutting to a larger, uniformly distributed low intensity beam for welding.

Drilling A patent for an electron beam drilling device was initially applied for in 1951 by Steigerwald [113] claiming the ability to produce holes with diameters down to 100 µm. The significant advantage to EB drilling is the ability to pulse and deflect electrons at rapid rates. The combination of high speed beam deflection and programmed work piece motion allows for hole drilling rates upwards of 3000 holes per second [89].

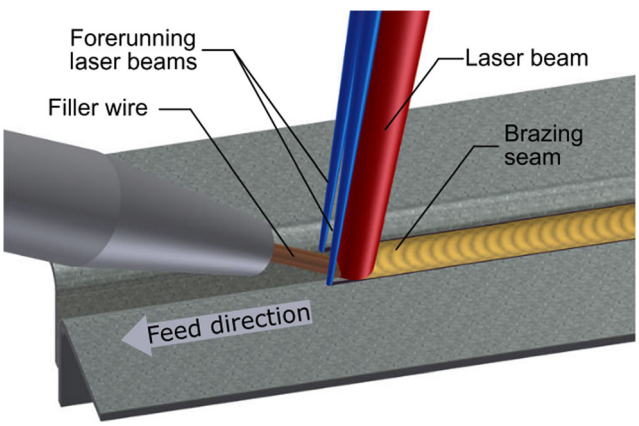

Fig. 18 Trifocal laser brazing [99]

Laser beam drilling was introduced as early as 1965 by repurposing a laser cutting machine to drill diamonds [114]. Laser drilling relies on high power densities (>10^5 W/mm^2) and short interaction times (micro to milliseconds) to vaporize and eject molten material during single or repetitive pulses [105]. Metals are largely drilled using lasers near 1 µm in wavelength and beams with divergence as low as possible to improve drilling performance. Larger holes are produced via laser trepanning to vaporize an increasingly larger region up to the desired hole size. For metals, pulse energies may range from 0.1 to 100 J/pulse with pulse durations ranging from 0.1-2 ms [107, 115].

Generally, high pulse energies produce faster drilling rates but decreased hole quality [115], and higher repetition rates of femtosecond pulses are advantageous compared to picosecond pulses [116]. By shortening pulse widths, material removal is more efficient and heat accumulation is reduced unless the subsequent pulse interacts with the particle plume [117]. Also, it is shown that changing the pulse shape [118] or modifying a progression of pulses composed of individual, repetitive pulses at different energies may improve hole quality [119].

Transformation hardening Transformation hardening was demonstrated as early as 1973 by Locke and Hella [120]. The HED heat treatment process allows for precise control of transformation depth (or "case" depth) with low heat input and minimal distortion. It is generally applied to iron-base or titanium alloys where rapid cooling promotes a martensitic reaction where hardening constituents form through allotropic transformations. The depth of case hardening is controlled by varying the power, beam size, and travel speed and is dependent on the alloy transformation properties. Hardening can also be accomplished by "glazing"; whereby, a surface layer is melted and rapidly solidifies as an amorphous layer [89], or progressive melting and remelting at decreasing depths to attain increased hardening depth [121].

Originally, CO_2 lasers were utilized (compared to other lasers) due to their high efficiency and output power. An issue with the 10.6 µm wavelength for transformation hardening is the high reflectivity (as high as 90%) on metallic surfaces [122]. To counteract the high reflection, absorptive coatings were applied to improve the process efficiency and remain competitive with other transformation hardening techniques. Using this approach, electron beam hardening is beneficial with energy transfer efficiencies nearing 80% [123].

Cleaning Laser cleaning has been expanded to a variety of applications from art restoration [106] to paint stripping [124, 125]. In comparison to conventional methods of

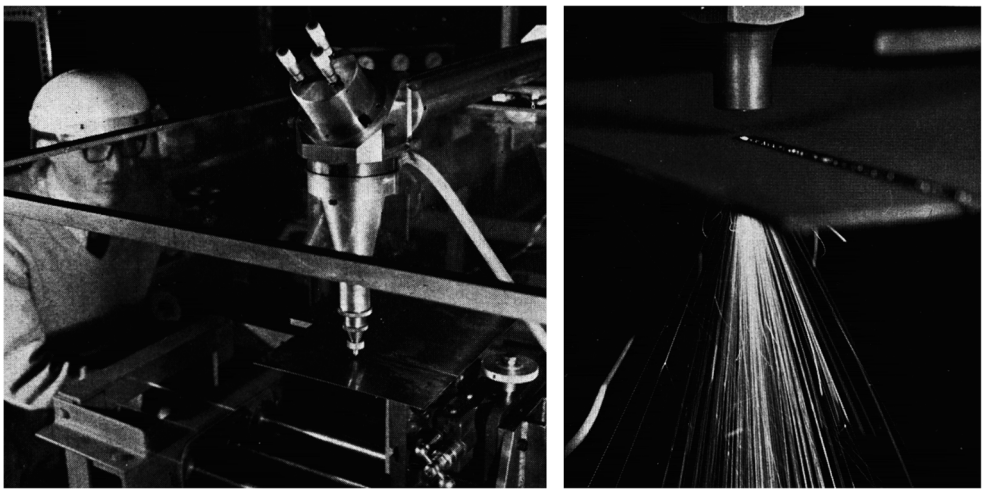

Fig. 19 Photos of CO_2 laser cutting at The Welding Institute in 1969 [104]

material preparation and surface cleaning such as pickling solutions and organic solvents, lasers are more environmentally friendly. Lasers are also favorable over mechanical methods such as blasting, abrasive sanding, or wire brushing through efficiency improvements and no consumable expenses. There are different mechanisms of material removal that depend on the laser power density and interaction time. This includes solely ablation or vaporization, impact of rapidly expanding gases to fracture bonds, and rapid heating of the surface to produce atomic vibrations that fracture bonds [106]. The first patent, "Method and Apparatus for Erasing", pertaining to laser cleaning was produced by Arthur Schawlow in 1971 [126], who helped develop the maser with Townes.

The practical material processing applications for laser cleaning are removing rust and oxide layers, grease, paint, dirt, and other unwanted substances adhered to surfaces. Removing scale from a steel surface was reported in 1974 using industrial CO_2 lasers at powers up to 10 kW [127]. The appropriate laser wavelength and source characteristics are dependent on the type of contaminant removal, especially when considering high frequency pulses, such as femtosecond lasers. Chen et al. [125] reported that CO_2 lasers are beneficial for paint removal on steel; while, the shorter wavelength Nd:YAG laser is conducive to rust removal applications because it is more susceptible to creating surface damage through heating [125]. Research from Lu et al. [128] showed that a KrF excimer laser (0.248 μm wavelength) was better suited at removing organic material on Cu, Al, and stainless steel than a CO_2 laser. Generally, laser output is pulsed for greater effectiveness and minimal thermal damage, and the use of picosecond and femtosecond pulsed sources are increasingly beneficial [129]. Seo et al. [130] showed improvements in copper oxide removal and minimal heating that causes reformation of oxides when using a femtosecond pulsed laser as compared to nanosecond pulsed Nd:YAG and excimer lasers.

1.2 Weld formation

High-energy density processes use two distinct "modes" to achieve penetration of the molten pool into the workpiece, namely, conduction and keyhole. These modes of welding affect the physical geometry of the fusion zone based on differences in interaction of the beam with the workpiece. A schematic comparison of conduction and keyhole mode weld profiles is provided in Fig. 20.

Conduction mode welding occurs at low power densities and results in a fusion zone with a low depth-to-width aspect ratio. In conduction mode, depth-to-width aspect ratios are generally less than one. High power densities produce deep penetration, high depth-to-width ratio welds that are attributed to the formation of a vapor capillary that produces a weld cross-section resembling a "keyhole." A transition or mixed mode region also exists between complete conduction and keyhole mode welding. This is a combination of conduction mode welding and the onset of keyhole formation. Figure 21 shows an approximation of the power densities needed for material processing applications from transformation hardening, through welding, and up to drilling based on beam diameter and power.

Although power densities and aspect ratios are reported to distinguish between keyhole and conduction, these numbers are approximations, and the actual weld regime is highly dependent on power, travel speed, beam diameter, and the material under investigation [132]. Figure 22 shows a distinction between these modes of welding as defined by Assunção and Williams [133]. They report a large transition regime with keyhole mode occurring just above 0.3 MW/cm^2 (3 kW/mm^2). The comparison between stainless steel (Fig. 22a) and aluminum (Fig. 22b) shows the difference associated with materials with aluminum having a higher reflectivity and thermal conductivity, thus showing a higher power density required for transitioning into keyhole mode welding. EBW exhibits a rapid

transition from conduction to keyhole mode due to the efficient energy transfer into the workpiece. One issue with LBW is the ability for the workpiece to absorb light energy. It is generally believed that absorptivity is proportional to the square root of electrical resistivity [134]. Webber et al. [134] report that absorptivity based on calculations of the material emissivity at 300°C for 304 stainless steel is less than 15% and Ti-6Al-4V is approximately 15%. The poor absorption of energy in LBW requires a much higher threshold power density, as large as two orders of magnitude [131], to generate a keyhole as compared to EBW.

To understand the difference between EBW and LBW, it is necessary to consider the underlying physics between photons and electrons. Based on the de Broglie equation, electrons can be treated as waves with a wavelength dependent upon Planck's constant and the momentum (mass x velocity) of the electron as shown in Eq. 1 [131]. Using the rest mass of an electron (9.110×10^{-31} kg) and a velocity 50% the speed of light (1.499×10^{8} m/s), Eq. 1 shows a six order of magnitude difference between the wavelength of an electron at 0.005 nm and the wavelength of a laser at 1070 nm.

$$\lambda = \frac{h}{p} = \frac{h}{mv} = \frac{6.626x10^{-34}\ m^2\ kg/s}{\left(9.109x10^{-31}\ kg\right)\left(1.499x10^{8} m/s\right)} \cong 0.005\ nm \qquad (1)$$

where: λ = wavelength, h = Planck's constant, p = momentum, m = mass, v = velocity

It is believed that the emitted photons from LBW interact with free electrons near the metal surface at approximately 10-100 nm of depth [131, 134]. The relatively large photon wavelength allows for easy reflection off the closely packed material surface; whereas, electrons have a wavelength orders of magnitude less than atomic radii and interatomic spacing. This allows for greater electron penetration and transmission of incident energy into the workpiece surface. Electron beams are reported to interact approximately 10-100 μm below the metal surface or 1000 times deeper than photons [131]. Fundamentally, this represents the difference between photon (LBW) and electron (EBW) interaction and is provided as background for LB and EB process comparison.

1.2.1 Conduction mode

Conduction mode welding causes intense heating of the material surface and conductive heat transfer (thermal diffusion) into the underlying material. The conductive heat losses and surface tension driven fluid flows determine the size and shape of the weld pool, and a steady-state condition is reached when the heat input from the beam is balanced by heat conduction into the base metal [135]. An advantage of conduction mode welding is the higher probability of producing welds free of defects by eliminating the instabilities associated with keyhole formation. During laser welding, the conduction mode limits weld penetration due to low laser coupling efficiencies caused by surface reflectivity and reduced melting efficiency. Pulsed laser welding is normally done in the conduction mode to better control penetration and limit heat input and is widely used for components such as medical devices [136] or electronics and hermetically sealed closure welds [105, 106]. Another important application of conduction mode welding is in laser powder bed fusion (LPBF). In additive manufacturing using powders, it is necessary to minimize vaporization and reduce potential defects that easily arise in deep penetration welding.

1.2.2 Keyhole mode

Keyhole mode, also known as deep penetration welding, requires concomitant melting and vaporization. Benefits include deep penetration, low heat input, and narrow heat affected zones. Formation of the keyhole requires rapid vaporization that imparts a recoil force that then depresses the molten weld pool to form a vapor capillary [137, 138]. The beam energy intensity is such that conduction, convection, and radiation are not adequate at removing heat beneath the incident beam. The keyhole is governed by complex physical interactions and remains an active area of research. An issue with fully understanding keyhole welding is caused by the extremely transient behavior [139, 140] and keyhole instabilities. Keyhole formation substantially increases the absorption of laser light by the vapor cavity "trapping" the incident beam and absorption by the generated vapor phase, which will also conduct heat back into the liquid [141]. When pulsed LBW is performed in the keyhole mode, the formation and stability of the keyhole is critical. Jouvard et al. [142] and Fujinaga et al. [143] reported that pulsed LBW involves a time delay between irradiation and keyhole formation, and increasing the peak power results in faster keyhole formation [106]. Instability of the keyhole can lead to keyhole collapse that in turn

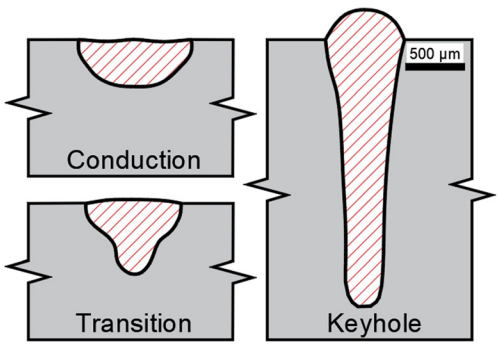

Fig. 20 Comparison of conduction, transition, and keyhole mode laser weld profiles in 304 stainless steel

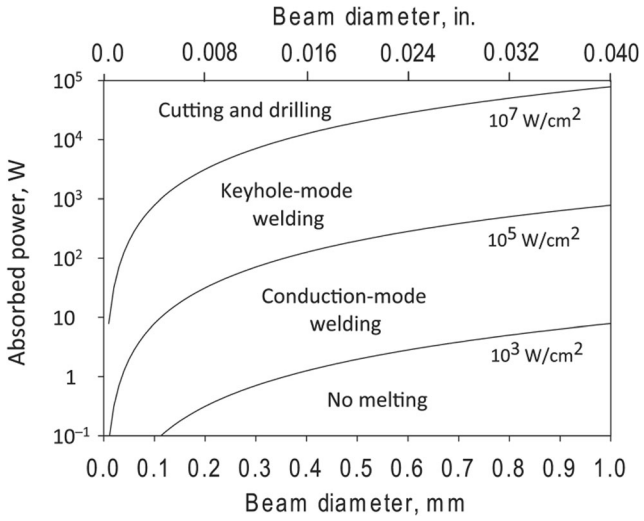

Fig. 21 Comparison of power and beam diameter for conduction versus keyhole mode welding [131]

promotes pore formation and root spiking defects. Examples of these discontinuities/defects are shown in Figs. 23 and 24 respectively. Other issues are entrainment of atmospheric air or shielding gas leading to significant gas porosity formation.

1.2.3 Physics of weld formation

The HED beam-material interaction is an extremely complex process with subtle process changes resulting in significant changes to resultant weld profiles. Figure 25 shows the numerous interactions that can occur during keyhole LBW. It is difficult to experimentally measure all the physical phenomena associated with the process, and therefore, mathematical modeling is often used to better understand the influences on process/material interaction relationships. Prior to the energy incident into the weld, there are physical interactions of the beam with the workpiece, plasma, and particles within the plume. After the energy is absorbed by the material, convective weld pool currents, heat conduction, vapor pressures, phase transformations, and metallurgical changes all influence the resultant weld.

Laser energy is absorbed by the vapor through inverse Bremsstrahlung effects when ionization produces a high density of free electrons but has a greater influence on a 10.6 μm wavelength as compared to 1 μm. The plasma absorption is commonly described by the Beer-Lambert Law [145], and the inverse Bremsstrahlung absorption is proportional to the square of the wavelength [146]. Because ionization potentials are believed to be minimal at a 1 μm wavelength [147, 148], Mie or Rayleigh scattering are the two mechanisms with a greater effect on beam attenuation. The scattering and attenuation occur because of the formation of metallic particles. The amount of Mie or Rayleigh scattering is dependent on the beam wavelength and plume particle size [149, 150]. Fresnel absorption [141, 145] is caused by variations in refractive indices from vapor-to-liquid and is believed to be the mechanism for energy absorption. The formation of the keyhole substantially improves the coupling of beam energy by allowing for numerous reflections off the keyhole wall to eventually become absorbed via Fresnel absorption.

In reference to Fig. 25, similar mechanisms are in effect with EBW when neglecting the differences between incident electrons versus photons and only considering the energy absorbed into the material. Under high vacuum conditions, there is minimal interaction of the generated plume with the incident electrons. Once the energy is absorbed into the workpiece, the weld formation for both processes is dependent upon fluid flow and vaporization.

Vaporization Vaporization is dependent on fluid flow, surface temperature, and diffusivities of vaporized elements. A thin layer exists at interfaces between liquids (or solids) with gases. This layer is known as the Knudsen layer and is caused by the evaporating particles having a reduced velocity a few (approximately three) mean free paths away from the interface [151]. This velocity is inconsistent with the bulk vapor velocities

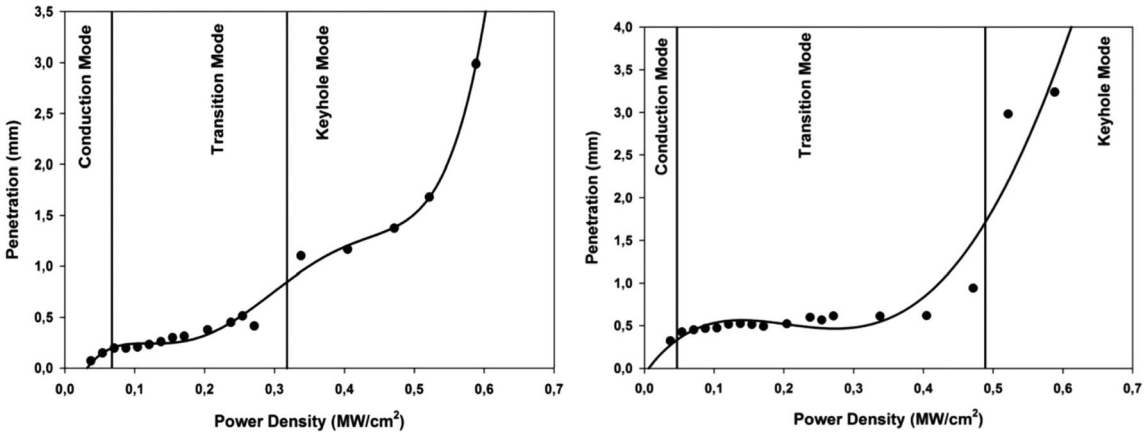

Fig. 22 Laser beam conduction to keyhole mode transition for: 304L stainless steel (a) and aluminum (b) as defined by Assunção and Williams [133]

[141, 152] and reported by Knight [151] to consist of supersonic flow. The recoil pressure [153] imparted by the vapor plume on the liquid surface maintains a compressive force against the keyhole wall, and the vapor motion creates shear stress on the liquid. This vapor interaction and induced shear stress causes additional fluid flow. The recoil pressure is necessary for keyhole formation and stabilization, and the back pressure from the vapor plume must continue to exceed the surface tension and hydrostatic forces attempting to close the keyhole [153].

Fluid flow and vaporization A significant contribution to weld formation is based upon fluid flows induced through chemical composition and thermal gradients. These forces include Marangoni (temperature-dependent surface tension), buoyancy, and vapor pressure. However, the combination of these forces and the relative magnitudes of each force dictates the resultant weld shape. This is important in both conduction and keyhole mode.

Fluid flow is largely dependent on the surface tension gradient in conduction mode welding as shown by Heiple et al. [154] and Kou et al. [155]. Cross-sections of laser spot welds on stainless steels with two different sulfur contents are shown in Fig. 26. Increasing sulfur to 140 ppm (0.014 %) shows a significant increase in weld penetration caused by the downward fluid flow along the weld centerline [156]. This mechanism is believed to be dependent on surface active elements causing an increase in surface tension at higher temperatures as proposed by Heiple and Roper [157]. However, Heiple et al. [154] showed no influence of Se, the surface active element, when welding within keyhole mode via laser and electron beam. Their assumption is that the surface active element only influences keyhole formation based on the overall magnitude of surface tension and is not influenced by a temperature dependency [154].

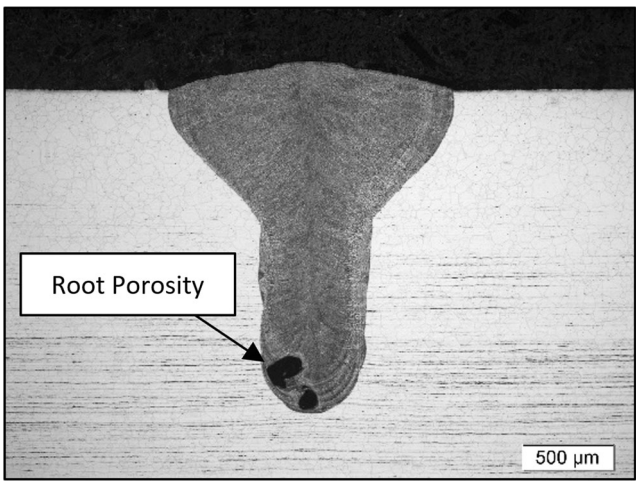

Fig. 23 Keyhole laser weld showing pores trapped near the root caused by keyhole instability [144]

Melt flows during keyhole mode welding are increasingly complicated as a result of the additional interaction of the vapor capillary with the molten metal. Figure 27 shows a schematic of the different flows as reported by Kaplan [158]. These flows become increasingly complex when analyzing pulsed laser welding [140] or manipulation/deflection of the laser or electron beam. For the liquid to divert around or below the keyhole, significant acceleration of the fluid is required and believed to be caused by the evaporative recoil forces [153].

Katayama et al. [159] and Matsunawa et al. [140] analyzed the formation of the keyhole and molten pool through in-situ x-ray imaging in pulsed and continuous laser welding. These results confirmed that the keyhole is extremely dynamic, and evaporation is not uniform along the wall. By introducing tungsten particles to the weld with real-time x-ray observation, fluid flow patterns were reproduced as shown in Fig. 28 [140]. The particle speeds were reported to reach as high as 0.4 mm/s along the front keyhole wall [140]. Analysis was also performed by Fujinaga et al. [143] for pulsed Nd:YAG laser beam welding showing the time delay from the laser pulse and maximum keyhole penetration. Some of the latest x-ray imaging analysis performed by Miyagi and Wang [160] revealed inclination of the keyhole front wall from nearly 90° at a 17 mm/s travel speed to 77° at a 167 mm/s travel speed.

In order to study fluid flow, Tenner et al. [161] and Eriksson et al. [162] utilized high-speed cameras to video the dynamics of the keyhole in real time. Analysis of the fluid flow velocity of the front keyhole wall is shown in Fig. 29 [161]. It is reported that the increase in fluid flow velocity with increased travel speed is based on changes to the recoil pressure caused by the evaporation at the front of the keyhole wall [161, 162] and the temperature-dependent changes in surface tension [161].

The exact mechanism driving fluid flow is difficult to quantify due to the transient nature of the process, but numerous models attempt to account for fluid motion for reproducing weld geometries. These models typically incorporate the Prandtl number or Prandtl mixing length hypothesis [153, 163–166] based on effective viscosity and effective thermal conductivity [167] within the molten pool. It is reported by Dowden [141] that the liquid is very turbulent as confirmed by instability issues and x-ray imaging [140, 143, 159, 168]; while, the vapor capillary or gas maintains a laminar like flow [141].

1.2.4 Weld modeling

The ultimate goal of modeling is to use representative relationships or mathematically compute physical phenomena to predict weld geometries (or penetration) with reasonable accuracy. Current limitations include accuracy of the predictive model, computational times, availability of appropriate

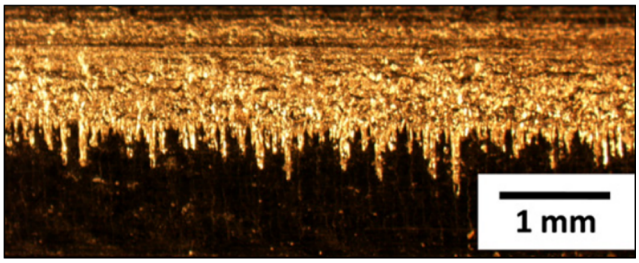

Fig. 24 Longitudinal weld section from keyhole mode LBW showing root spiking [137]

physical material properties, and an inability to solve complex mathematical solutions directly. There are numerous methods reported in the literature to predict weld penetration or geometry from input parameters and material properties. The wide range of modeling approaches includes analytical, numerical, and dimensionless predictions. These substantially vary in complexity, computation time, output information, and accuracy. This review does not attempt to summarize or comment on the many models that have been developed for HED processes. For more detailed reviews of laser weld modeling, the reader is referred Mackwood and Crafer [169], and Svenungsson et al. [170]. Table 5 provides a limited, chronological synopsis of literature pertaining to EBW and LBW modeling.

1.3 Overview of metallurgical considerations

Metallurgically, HED processes can produce small fusion zones with rapid solidification rates, and narrow heat affected zones with high thermal gradients. These conditions result in significant differences in weld microstructural evolution compared to high-energy input arc welds. The following sections will summarize the metallurgical issues specific to EBW and LBW.

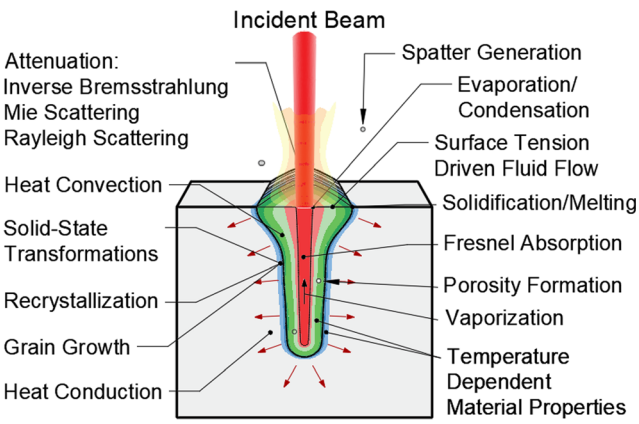

Fig. 25 Schematic showing physical and metallurgical process considerations during keyhole LBW

1.3.1 Solidification behavior

Grain orientation and grain growth The fusion zone (FZ) grain structure is initially determined by the heterogeneous nucleation and epitaxial growth that occurs at the fusion boundary. Subsequent growth within the fusion zone depends on crystallographic effects and preferential dendrite tip temperatures [184]. Conduction mode welds with elliptical pools behave similar to arc welds at relatively low travel speeds. Assuming a cubic crystal (such as body-centered cubic and face-centered cubic), the preferential growth direction is along the (100) cube edge direction, and competitive growth between the epitaxially nucleated dendrites will favor the dendrite aligned with the heat flow direction and oriented normal to the fusion boundary at the trailing edge of the fusion zone. As depicted by Rappaz et al. [185, 186] in Fig. 30a, dendrites growing normal to the interface ($\vec{n}$) can grow at the slowest velocity and require the lowest degree of undercooling. This results in a gradual change in growth direction from the weld toe towards the weld centerline with the grains slowly conforming to the shape of the weld pool as growth progresses. However, in keyhole mode high aspect ratio welds, these orientations are accentuated and can cause distinct microstructural changes with abrupt regions of growth directions stifled by competitive growth from another orientation. A schematic of these distinct orientations is shown in Fig. 30b.

Figure 31 shows the experimentally observed growth directions for an EB, keyhole mode weld on an Fe-15Ni -15Cr alloy [186]. This change in growth direction is based on the geometry of the weld pool and the angle of the solid-liquid interface and continues until competitive growth favors a growth direction within the <100> family oriented closer to the solid-liquid interface. Likewise, David et al. [187] showed that EB and LB weld pool geometries have a significant influence on growth directions in single crystal nickel-base alloys.

In high aspect ratio welds, titanium alloys show prior beta grain (PBG) solidification structures nearly parallel to the plate surface based on transverse cross-sections, and Liu et al. [188] reported that higher travel speeds showed increasingly columnar grains in commercially pure Ti. Lu et. al [189] revealed that the beta grain size slightly decreased (length and width) from the top of the weld to the root. Results from Akman et al. [190] showed an increase in prior beta grain size (PBGS) with increasing average power (constant peak power) for pulsed laser beam welding (P-LBW). The average grain size was reported to increase by approximately 250 μm for each 100 W of increasing average power [190]. Wei et al. modeled three-dimensional crystal growth of keyhole mode laser welds on aluminum [191] and copper [192]. The results of these simulations are shown in Fig. 32 [192] and illustrate the difference in crystallographic growth between two different travel speeds. At the slower travel speed (Fig. 32a), it appears that columnar grain growth parallel to

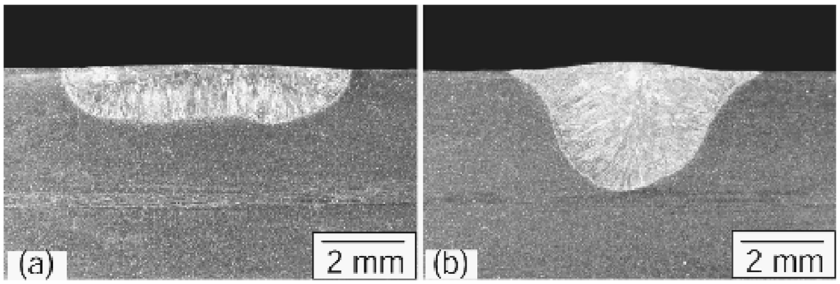

Fig. 26 Change in laser spot weld pool shape on 304 L stainless steel at (a) 40 ppm sulfur and (b) 140 ppm sulfur [156]

the top surface is more dominant and decreases at higher travel speeds (Fig. 32b).

Solid-state grain growth in the HAZ can be an issue for controlling the grain size in the fusion zone, especially when welding isotropic alloys or alloys solidifying as body centered cubic with rapid solid-state growth such as in titanium alloys [193]. However, systems such as austenitic stainless steel are not susceptible to extensive HAZ grain growth especially when welding on annealed or hot-rolled alloys as compared to alloys that are heavily cold worked [107, 194]. Cam et al. [195] showed minimal change in mechanical properties across laser welded joints in austenitic stainless steel. Evidence of the minimal grain growth in magnesium was shown by Coelho et al. [196] who reported LB HAZ weld widths as low as 10 μm and nearly comparable to the base material grain size. Minimizing HAZ grain growth is performed by increasing travel speed and/or reducing power. Riofrio et al. [197] and Benyounis et al. [198] reported that travel speed (at constant power) is the largest influence on the width of the HAZ.

Solidification rate, thermal gradient, and growth modes The combination of the solidification rate (R) and the thermal gradient (G) dictate the resultant solidification modes (planar, cellular, dendritic), and the HED processes are capable of substantially increasing these values as compared to arc-based processes. The product of the thermal gradient and the solidification rate (GxR) determines the scale of the solidification structure as measured by primary or secondary dendrite arm spacing. The ratio of the thermal gradient to the solidification rate (G/R) determines the mode of solidification [156, 164, 199]. The higher cooling rate achieved through EBW substantially decreased the cell size as shown in Fig. 33 [200]. Similar results are shown in Fig. 34 for EB welds at travel speeds of 6.5 mm/s (Fig. 34a) and 100 mm/s (Fig. 34b) on the same stainless steel alloy [201]. These results show how the increased solidification rate dramatically alters the size of the solidification substructure from a coarse, cellular dendritic to a fine, cellular morphology.

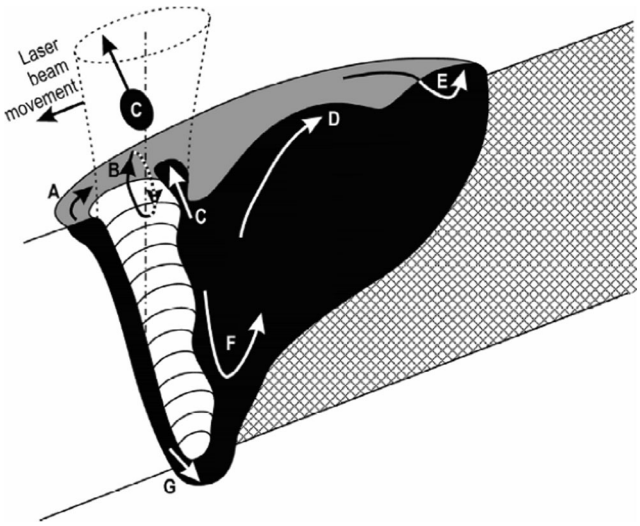

Fig. 27 Schematic of keyhole mode melt flow phenomena: melt flow around vapor cavity (A), Marangoni flow (B), spatter generation (C), humping (D), rear flow (E), eddies (F), and root drop-out (G) [158]

In addition to the thermal gradient and solidification rate, the solidification temperature range (STR) will influence the solidification behavior by promoting constitutional supercooling as reported by David and Vitek [199]. This was demonstrated with an EB weld where the solidification mode shifted from columnar dendritic to equiaxed dendritic at the centerline when the solidification temperature range was intentionally expanded by alloying. The welds were on an Fe-15Cr-15Ni single crystal doped with sulfur, which promoted solute partitioning during solidification, reduced the solidus temperature, and increased the solidification temperature range. These results are shown in Fig. 35 [199]. Similarly, this equiaxed structure was also shown for nickel-base alloys along the weld centerline with solute partitioning and eutectic formation [187].

Vitek et al. [202] analyzed the results of rapid solidification on a Type 308 austenitic stainless steel and showed that CW CO_2 LBW produced microstructures consisting of a fully austenitic structure at a travel speed at or above 25 mm/s; while, at a 13 mm/s travel speed, the weld exhibited a range of microstructures from fully austenitic to an austenite plus ferrite (AF) structure. It was reported that the cooling rates necessary to promote the transition from primary ferrite to primary austenite is in the range of 10^5-10^6 K/s [202].

Much of the research for HED welding of stainless steels stems from solidification cracking issues in alloys solidifying as primary austenite. Primary ferrite formation during solidification is advantageous in welding of stainless steels by reducing the susceptibility to solidification cracking [194]. The predictive

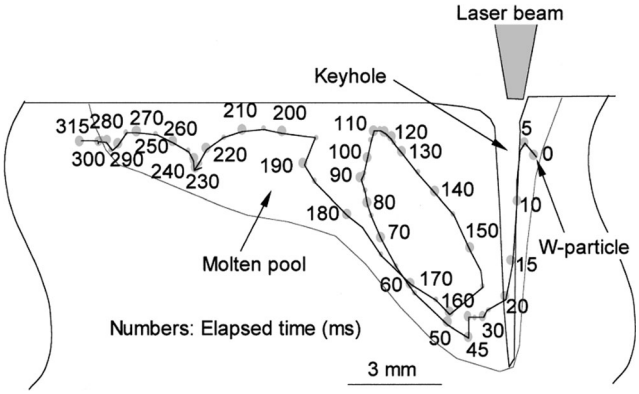

Fig. 28 Position of tungsten particle in weld pool showing the elapsed time in milliseconds from Matsunawa et al. [140]

stainless diagrams experimentally developed for arc welding processes, such as the Schaeffler [203], DeLong [204], or WRC-1992 [205] are not applicable when considering rapid solidification. The high solidification rates in HED processes can favor a transition from primary ferrite to primary austenite [206], and this is believed to be based on the dendrite tip undercooling which influences the stability of ferrite versus austenite [207, 208]. The change in solidification mode along with restraint, grain orientation, and impurity levels can lead to increased cracking susceptibility during HED welding. Lippold [209] reported crack formation in a deep penetration EB weld in Type 304L as shown in Fig. 36. This transition from primary ferrite to primary austenite solidification resulted from the increased solidification rate at the weld centerline.

Impurity elements, such as S, P, and B, further increase solidification cracking susceptibility. The original Suutala diagram developed by Kujanpää et al. [210] showed the relationship between S and P content and chromium-nickel equivalency (Cr/Ni Eq.) with regards to cracking susceptibility. A dramatic increase in cracking susceptibility occurred when the primary phase of solidification shifted from ferrite to austenite. For HED welding, the transition in cracking susceptibility is shifted to higher Cr/Ni Eq. values due to the effect of higher undercooling on solidification behavior. The modified Suutala

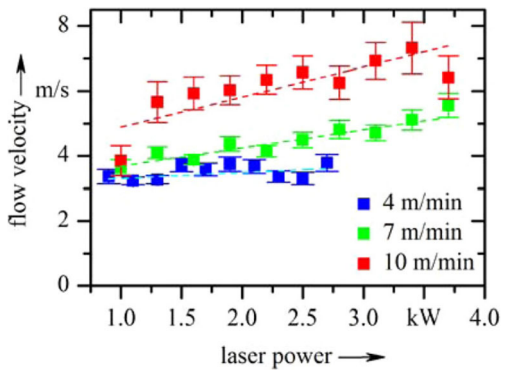

Fig. 29 Flow velocity at the keyhole front for increasing laser powers measured at three different travel speeds [161]

diagram shifted the critical Cr/Ni Eq. ratio for HED welds up to approximately 1.65 [208] versus 1.48 [210] for arc welds. Additional analysis of LBW on austenitic stainless steels was performed by Lienert and Lippold [211] using the Hammar and Svenson [212] equivalencies. Their results showed Type A solidification occurring below 1.59 and mixed mode austenite and ferrite microstructures up to 1.69. Above Cr_{eq}/Ni_{eq} = 1.69, the microstructures exhibited primary ferrite solidification, and no cracks were observed [211]. Hochanadel et al. [213] showed the influence of solidification modes for pulsed LB welds on a joint between 304 and 304L stainless steel. Two different solidification modes were stabilized, and dilution resulted in primary austenite and solidification cracking.

Elmer et al. [201] analyzed the influence of solidification modes for EBW of stainless steel alloys and produced a plot of composition versus travel speed for the corresponding mode. At travel speeds of approximately 75 mm/s, a "massive" transformation to austenite occurs following primary ferrite solidification. Because the F/MA microstructure first solidifies as ferrite, it is believed to be resistant to solidification cracking [194, 208]. Lippold [208] extended the analysis of solidification modes and microstructural formations based on the solidification rates in P-LBW. Along with prior data, a microstructural map was developed for 300-series SS alloys as shown in Fig. 37 [208].

Phase transformations (cooling rate effects) The high cooling rates associated with HED processes can produce room temperature FZ and HAZ structures that contain nonequilibrium phases. Materials sensitive to cooling rate effects on phase fractions can have issues that include higher susceptibility to cracking and reduced mechanical properties and/or corrosion resistance.

Carbon and low-alloy steels are especially susceptible to martensite and/or bainite formation that can produce a steep hardness gradient between the base material and weld zone. These steep gradients can lead to stress concentrations and crack formation [107] and are exacerbated with higher carbon contents. Cam et al. [195] reported increases in hardness of 150 $HV_{0.1}$ towards the weld centerline in a low carbon steel, and Riofrío et al. [197] reported the ability to promote bainite formation by increasing heat input to 80 J/mm relative to 20 J/mm in LB welded high-strength low-alloy steel. The latter heat input produced a mixture of bainite and martensite within the FZ and maintained a comparable hardness as the base material. Although, a wider range of softening was present in the HAZ.

Cooling rates can significantly influence titanium alloys by altering solid-state phase transformations from the elevated temperature beta (β) phase to alpha (α), and alpha prime (α') phases during cooling. The alpha prime (α') or martensite transformation can occur at cooling rates from 100 and 10,000 °C/s [193] in alloys that form significant beta phase at elevated

Table 5 Review of LB weld modeling

Researcher	Description	Year	Process
Rosenthal [171, 172]	Moving point and moving line heat sources	1935 1946	Arc processes
Swift-Hook and Gick [173]	Analytical model based on a line heat source and dimensionless analysis	1973	EBW, LBW
Klemens [174]	Cylindrical cavity of variable radius, radial heat flow, horizontal fluid flow	1976	EBW, LBW
Mazumder and Steen [175]	Gaussian heat source, 3D heat flow using FDM, reports dimensionless groups, no fluid flow	1980	LBW
Miyazaki and Giedt [176]	Elliptical shaped cylinder in infinite plate	1982	EBW
Goldak [177]	FEM analysis of double ellipsoid heat source	1984	EBW, LBW
Dowden [166]	Assumes cylindrical keyhole with varied radius, axial fluid flow perpendicular to keyhole	1985	LBW
Kaplan [145]	Predicts keyhole wall geometry based on point-by-point energy balance, applicable to high welding speeds, neglects fluid flow	1994	LBW
Sudnik et al. [178]	Analyzed radiation absorption, vapor, and weld pool; used vertical and horizontal laminar flows	1996	LBW
Matsunawa and Semak [179]	Simulated the front keyhole wall based on one dimensional melt motion	1997	LBW
Ki et al. [180]	Level set (LS) method for vapor-liquid interface tracking	2002	LBW
Rai et al. [164, 165, 181]	Uses energy balance at keyhole wall and 3D heat transfer fluid flow	2006 2007 2009	EBW, LBW
Amara et al. [182]	Analysis of melt pool dynamics using the volume of fluid (VOF) method for interface tracking	2008	LBW
Hann et al. [183]	Used normalized enthalpy relationships for predicting weld penetration	2011	LBW
Jiang et al. [146]	3D heat transfer and fluid flow model [178] with analysis at reduced ambient pressure based on boiling point variations	2020	LBW

temperature. As in steels, the issue with the α' transformation is a reduction in toughness and ductility. Liu et al. [188] analyzed commercially pure titanium and reported the ability to produce a massive transformation to alpha at high cooling rates with retained prior beta grain boundaries showing remnants of the solidification structure. Whereas, lower cooling rates allowed for long range diffusion and nucleated more alpha [188]. For Ti-6Al-4V, Kumar and Sinha [214] also reported a massive alpha transformation with retained beta phase only observable with transmission electron microscopy. High cooling rates during HED welding of alpha-beta titanium alloys promotes a transformation to α' martensite [215, 216]. Lu et. al [189] analyzed EB weld microstructures on low impurity Ti-6Al-4V and reported a fusion zone microstructure consisting of large prior beta grains entirely transformed to α'. Likewise, Casalino et al. [217] analyzed the laser welding of Ti-6Al-4V and reported a complete transformation to α' with coarse prior beta grains. These welds were performed at 1200 W and travel speeds ranging from 1000 to 2500 mm/min (16.7–41.7 mm/s).

The ability to maintain optimum ferrite/austenite ratios is a concern when HED welding of duplex stainless steels (DSS) with Cr/Ni equivalency ratios greater than 2.25. The extreme cooling rates promote higher than desirable fractions of ferrite

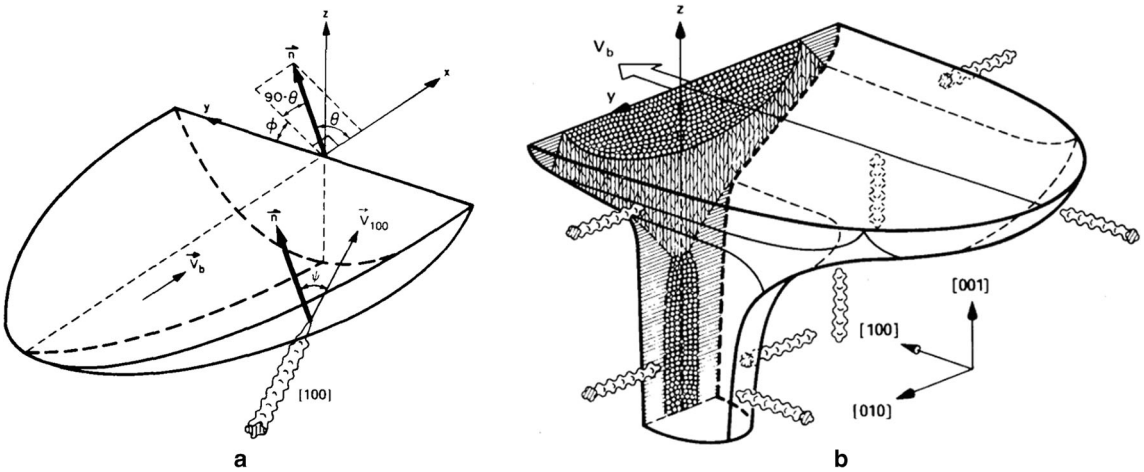

Fig. 30 Illustration of crystal growth in an elliptical weld pool geometry (a) [186]. Illustration of keyhole weld pool showing potential preferential growth directions (b) [185]

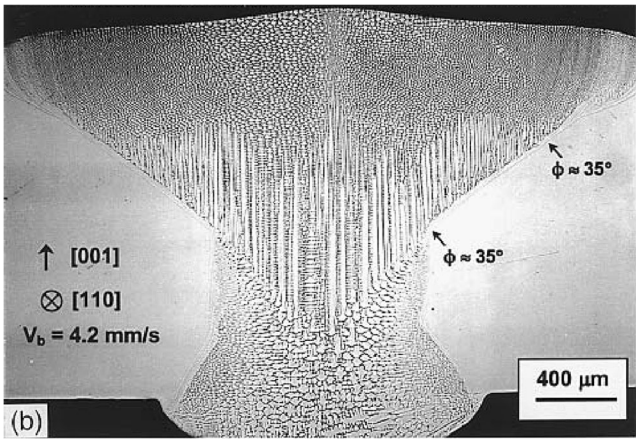

Fig. 31 EB weld at 4.2 mm/s on an Fe-15Cr-15Ni single crystal alloy showing columnar dendritic growth in different orientations from Rappaz et al. [156, 185]

due to insufficient time for diffusion-controlled austenite transformation [218–221]. LBW studies of DSS reported that faster travel speeds (lower heat input and higher cooling rates) led to higher fractions of ferrite [222] with ideal austenite/ferrite ratios occurring at cooling rates well below 100 K/s, as shown in Fig. 38 [221].

The rapid cooling occurring when welding duplex stainless steels can also lead to a saturation of nitrogen [220] in both the FZ and HAZ. This nitrogen readily forms Cr_2N precipitates and can significantly influence corrosion properties [194, 218, 223]. It is generally not recommended to weld DSS with an HED process [218]; however, research has attempted to utilize alternative methods such as preheating [224] or postweld heat treating using a defocused laser immediately following laser welding [223]. For successful HED welds in duplex stainless steels, it is necessary to reduce the cooling rate to promote austenite formation and reduce nitride precipitation.

Vaporization effects The nature of a high intensity beam and keyhole formation results in vaporization during HED welding, and welding under high vacuum with volatile elements significantly increases vaporization rates. Preferential vaporization can result in a loss of alloying elements from the weld pool and is reported to be a significant problem in alloys containing elements with low partial vapor pressures [225]. Pastor et al. [226] showed a reduction in weld metal Mg as high as 1.3 wt% for conduction mode laser welds on Al-Mg alloys. However, when welding in the keyhole mode, the Mg reduction was significantly reduced [226]. Khan et al. [227] showed a reduction in Mn content in high manganese austenitic stainless steels with the amount of loss reported to be dominated by the weld pool size. Similarly, Berger [228] showed the reduction in Mn content in 304L stainless steel under numerous weld passes. The loss of alloying elements can affect the weld microstructure which may influence weldability, mechanical properties, and corrosion resistance. For example, EBW of duplex stainless steels in high vacuum environments accelerates weld metal nitrogen loss and reduces the ability to stabilize austenite, resulting in highly ferritic weld deposits.

2 Electron beam welding

2.1 Fundamental principles of electron beam welding

This section describes the essential elements of an electron beam welding (EBW) machine. This includes how the beam is generated and controlled, and the peripheral equipment required to perform welds in a reduced pressure (vacuum) environment.

2.1.1 Essential parts of the machine

All EBW systems can be divided into three main parts: the cathode, the anode, and the lenses, as shown in Fig. 39 [230–236].

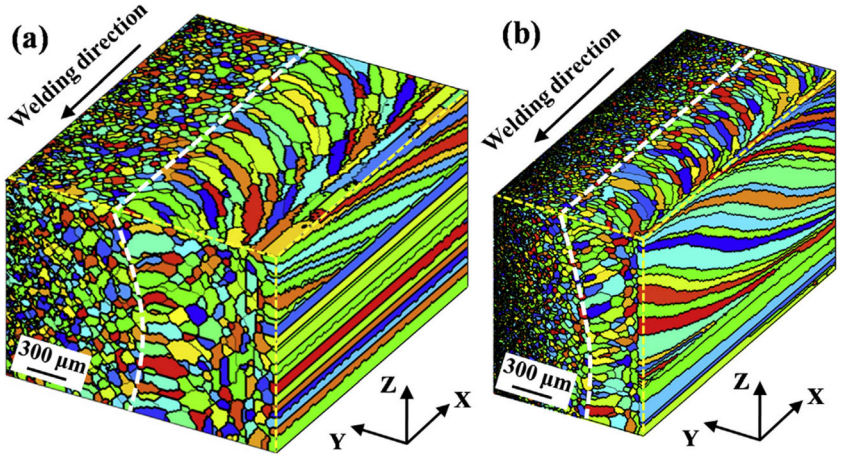

Fig. 32 3D model of crystallographic growth for laser welds on a Cu alloy at 16.7 mm/s (a) and 133 mm/s [192]

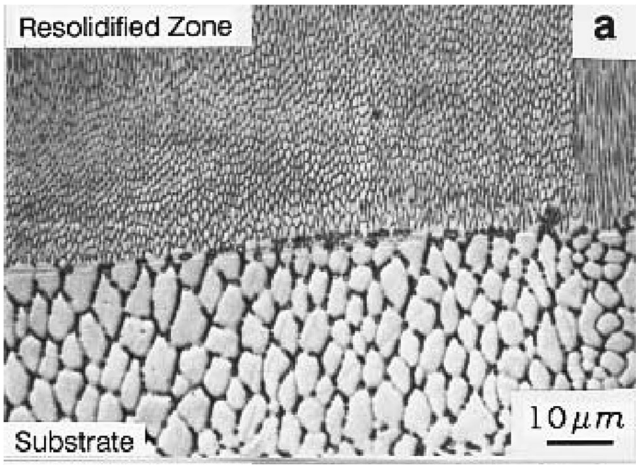

Fig. 33 Reduced cell size within an EB weld (top) cooled at 1.5×10^6 °C/s and a substrate cooled at 2×10^3 °C/s (bottom) [200]

Beam production The electron beam is produced by an emitter or filament. Generally, the filament is tungsten since this element has a high atomic number which supplies the needed electrons. Filaments are supplied in different shapes and sizes. Two types of emitters that are commonly used are "hairpin" and "ribbon" filaments, as shown in Fig. 40 [238–240]. Since hairpin filaments possess a smaller cross section and can be shaped to a point, they will produce a smaller, more precise, beam that can be used for micro-machining and micro-joining [241]. Ribbon filaments are much more durable and provide longer filament life, so they are more commonly used if beam size is not an issue. The filament is electrically heated (Joule heating) until a stream of electrons are produced by thermionic emission. The beam produced will be an "image" of the filament. In other words, if a square filament is used, the beam cross section will approximate a square shape, with electron "hot spots" in the corners where heat cannot be conducted away. Additional discussion is provided in Section 2.2.2 and depicted in Fig. 43.

There are two basic designs for EBW machines as differentiated by having either a diode gun or a triode gun. In the diode design, there is simply a cathode (filament) to produce the beam and an anode to accelerate it. The beam current is a function of the high voltage differential applied, where the voltage differential effectively draws the electrons off the filament tip. With this arrangement the current cannot be changed independently of the voltage. In the triode design, there is a "bias cup." The bias cup applies a separate potential difference, known as a bias. Variation in the bias will result in different currents, regardless of the voltage differential between the emitter and the anode [89, 230–234]. Most modern EBW machines use triode guns in order to independently adjust the beam current and beam voltage.

Acceleration As described previously, the beam is accelerated using an anode with a high voltage differential. The anode is hollow (annular), allowing the electrons to pass completely through at rates from 50% [230] to 70% [89] of the speed of light. These extreme speeds allow for a high momentum of the beam of electrons into the workpiece, which in turn results in extreme heating and, in most cases, vaporization of the metal at the surface. Temperatures are reported to reach up to 25,000°C [230]. Upon exiting the hollow anode, space charge effects will result in the dispersion of the beam. This occurs because the negatively charged electrons repel each other, producing a larger beam diameter that results in a beam with lower power density than needed for welding. In order to correct this, the beam must be focused.

Focusing and deflection lenses The beam passes through magnetic lenses, and the two main types are focusing and deflection lenses. The focusing lens will constrict the diverging beam so that it will pass through "sharp focus," where the beam reaches a minimum size. Welding conditions can call for a sharp focused beam, or one that is not as constricted, known as "defocused." The change in beam diameter, or "spot size," will change the power density.

The deflection lens controls the spatial location of the beam. Manipulations in the deflection current will allow for movement of the beam, including deflecting it into complex patterns. The deflection of the beam can be controlled at very high frequencies, so much so that the workpiece will "see" the pattern as one continuous beam. For example, the beam can be deflected in a circular motion, and at high frequencies the beam will act not as a deflected point but as a larger circular beam. This can be manipulated to produce the effect of

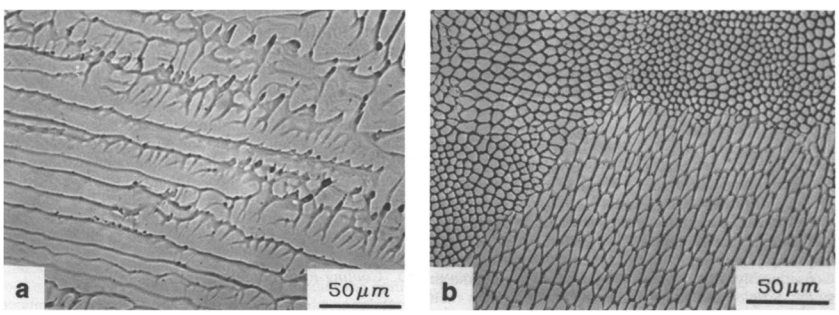

Fig. 34 Primary austenite solidification showing dendritic solidification at 6.5 mm/s travel speed (a) and cellular solidification at a 100 mm/s travel speed (b) [201]

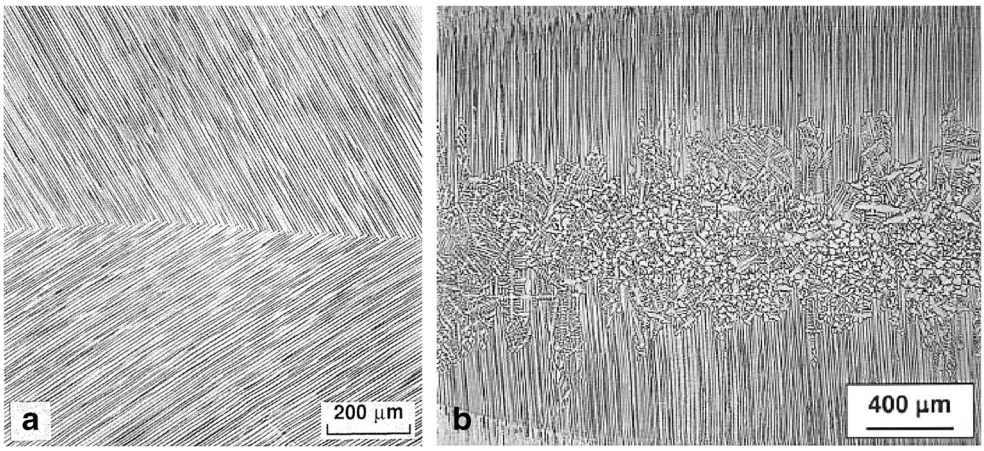

Fig. 35 EB weld (plan view) on a single crystal Fe-15Cr-15Ni alloy: a) pure, b) sulfur bearing [199]

multiple beams on the workpiece and to control the microstructure and geometry of the weld [242].

2.1.2 Other parts of the machine

Chamber Every electron beam welding machine must have a workspace of some dimensions where the beam interacts with the workpiece. Non-vacuum EBW machines do not require an enclosure for the beam, but an X-ray shield is still required. Vacuum chambers are required for medium and high-vacuum EBW machines. These chambers are usually large cylinders or rectangles that can support the pressure loads created by the internal vacuum required for operation. Many of these chambers incorporate a CNC controller so that the electron beam can remain stationary while the workpiece moves in order to be welded. However, some mobile electron gun systems have been developed. Chamber size dictates the size of components that can be welded. Chambers can be quite large, 20 m^3 (~700 ft^3) or more, but larger chambers are more expensive, require more vacuum pumps and/or longer pump down times. Therefore, it is most cost-effective to have chamber size matched to the size of parts to be welded. [89]

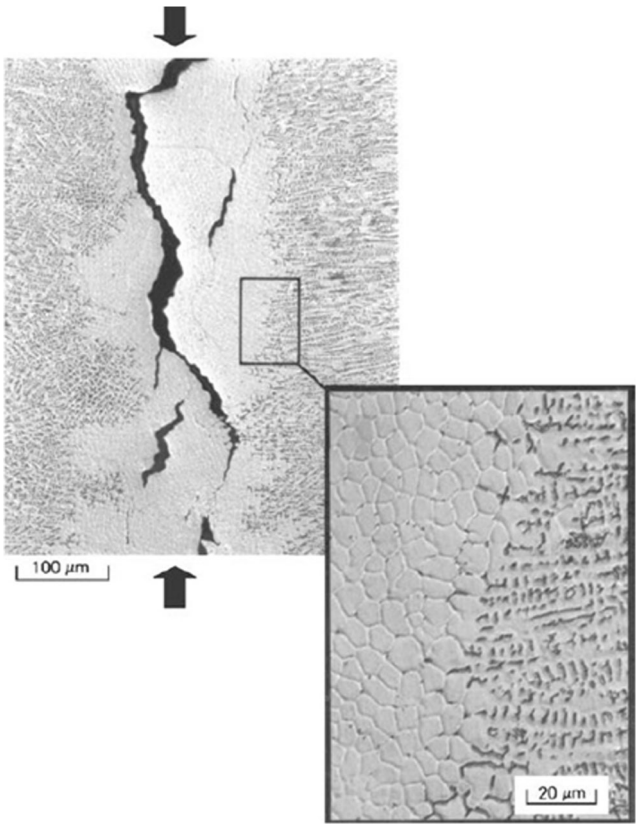

Fig. 36 Weld solidification crack along EB weld centerline in Type 304L SS [209]

Vacuum pumps Depending on the level of vacuum required and the size of the chamber, the number and type of pumps required for the system will vary. Most EBW machines have at least two pumping systems that consist of two pumps each [89]. There are two vacuum systems since it is most efficient to have one system for the gun column and another for the chamber. If a high vacuum is not maintained in the gun column, the machine can "arc out," resulting in no beam and potential damage to the filament or other equipment [243].

Vacuum pumps are either capture pumps or transfer pumps. Capture pumps "capture" the gas molecules. This can be permanent or temporary. Sorption and sublimation pumps fall in this category. Transfer pumps move the gas molecule via compression from the low-pressure area to a higher-pressure area. Rotary, mechanical booster, turbo-molecular, and diffusion pumps fall in this category. Rotary pumps function using rotating vanes or pistons which draw air in, compress it, and exhaust it out of the chamber. Mechanical boosters use "figure 8" rotors which perform the same function. Sorption pumps make use of a porous material which can absorb gas molecules at very low temperatures. Turbo-molecular pumps utilize several alternating sets of rotors and stators that have inclined blades which act in the same manner as a jet engine. These pumps are very expensive. Diffusion pumps use oil vapor to push the air molecules from

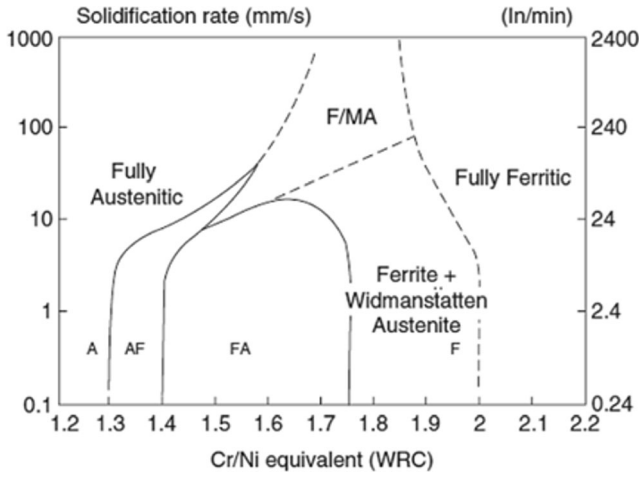

Fig. 37 Microstructural map for pulsed laser welded austenitic stainless steels [208]

the chamber port to an outlet, which takes some time, power, and maintenance due to heating of the oil. Sublimation pumps use an active cathode generally made of titanium which reacts with gas molecules once bombarded with high velocity ions. A chart showing the level of vacuum generated by each pump type is provided in Fig. 41 [235]. It should be noted that cryo-pumps were historically used to reduce pump-down times. Cryo-pumps utilize low temperatures so that when the gas molecules or residual air moisture interacts with a cold surface, the molecules are removed from the residual air [244, 245]. However, these pumps are becoming obsolete as newer machines utilize the previous pumps listed.

More pumps can be added to decrease pumping times or increase vacuum quality. Slow venting is preferred to prevent a rapid pressure differential which can cause equipment wear. Non-reactive or inert gas backfill is also an option to reduce chances of oxidation [89].

Leaks can be real or virtual. A real leak is due to a malfunction in the vacuum equipment or the chamber and must be fixed by maintenance. Virtual leaks are the result of gas trapped in a piece of equipment that is in the chamber. As the chamber pumps down, the gas escapes the part in the chamber. This appears as though a leak is present since the target vacuum level cannot be attained [246].

For a given chamber size, the type of vacuum system will dictate how quickly the chamber can be pumped down and what vacuum level can be achieved. The vacuum level achieved will affect both the weld quality and penetration characteristics. In general, extremely high vacuums provide the best quality and penetration, but there is an economic penalty since the pump down time may be quite long. Also, as the pumping efficiency increases (faster pump down times), the cost of the vacuum system generally increases.

Voltage supply An EBW machine is typically classified by its maximum voltage output. A voltage supply that is capable of 60 kV or less is classified as a low-voltage electron beam welder (LV-EBW), and one that is capable of greater than 60 kV is known as a high-voltage electron beam Welder (HV-EBW) [89]. A typical range of voltages for HV-EBW is 80–150kV, but voltages of 200 kV have been reported. If operating in non-vacuum conditions, a HV-EBW machine is required. For either machine, powers up to 30 kW are attainable. Differences can be seen in Table 6.

HV-EBW is more practical for producing high aspect ratio, deep penetration welds since it can generate a smaller spot size and higher energy electrons capable of deeper workpiece penetration. This is due to the higher acceleration velocity of the electrons, resulting in higher kinetic energy. However, smaller, cheaper machines are typically low voltage. Since the supply does not need to produce as much voltage, the X-ray shielding can be reduced since there is less radiation, and the electron beam gun generator can be smaller and more maneuverable.

2.1.3 Beam characteristics

Electron beam welding is dependent on the size and shape of the beam. The beam is generally circular with continuous power, although efforts have been made to perform pulsed-power electron beam welds [244, 247–249].

Beam diameter The electrons in the beam interact with each other to produce beams of different shapes and sizes. Since electrons are negatively charged particles, they will repel each other in all directions. The force by which they repel is dependent on current, or the rate of electron flow, and voltage, or the energy per electron. As the number of electrons at a given point increases, there will be a "space charge effect" resulting in an increase in repellent forces, resulting in a larger beam. Conversely, if the energy per electron is high, generally due to an increase in voltage, the time-of-flight from filament to workpiece will be low, and there will be a slight reduction in beam diameter [250–252]. The beam current has a greater effect than the voltage on beam diameter at sharp focus, and this effect is linear [89], as can be seen in Fig. 42.

The beam must be constricted by the focusing lenses to produce a sharp focus, and current to these lenses must be controlled to constrict the beam. This has a strong dependence on voltage since it requires more focusing current to constrict a higher energy beam. It has been observed that there is a linear relationship between focusing current and voltage at a given distance. Beam current has negligible effects on focusing current. In general, longer working distances result in larger beam diameters since there is more time for electron repulsion. [250, 254, 255]

Beam distribution Electron beams are ideally a Gaussian distribution [176, 250, 254, 256]. As the beam is constricted through sharp focus and begins to broaden again, the

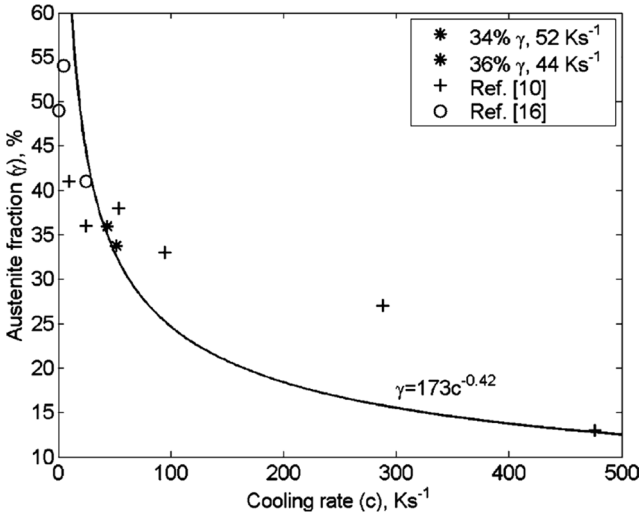

Fig. 38 Austenite phase fraction versus cooling rate for a duplex stainless steel [221]

repulsion forces are uniform in all directions and the power distribution will appear Gaussian. However, before it passes through sharp focus, the beam will not be completely Gaussian. As previously stated, the beam will appear as an image of the filament. Therefore, some "hot spots" will be present where more thermionic emission occurred from the filament due to imperfections and heat conduction differences in the geometry. In this under focused condition, the beam distribution is less predictable than in a sharp or overfocused condition. A representation of this is shown in Fig. 43.

The distribution can be changed to something non-Gaussian by either using a custom filament or by precise control of magnetic fields [257]. Often, these methods are not practical, so deflection can be used. Although this will not change the distribution of the beam, a high frequency can be used, resulting in what appears to be a different beam distribution, which has been confirmed using diagnostic devices [258].

2.2 EBW penetration characteristics

EBW is often selected because of its ability to achieve deep penetration in a single pass. Welds that require multiple passes and addition of filler metal using arc welding processes can be made in a single pass with EBW. In order to achieve such deep penetration, welding must be done in the "keyhole mode" where vaporization of the workpiece and acceleration of the electron beam produces a cylindrical "hole" around which melting occurs. If no keyhole is produced, melting occurs in the conduction mode with resultant welds being much shallower. Electron beam welds made in the conduction mode may resemble those made using gas tungsten arc welding (GTAW). Weld penetration and the depth-to-width ratio of the weld is related to process parameters [174], composition of the material to be welded [201, 259, 260], and the number of passes [255]. The following sections review the effect of process parameters on penetration characteristics of single pass keyhole mode welds.

2.2.1 Keyhole formation and effects

Considerable research has been performed to understand the formation of a keyhole in electron beam welding [255, 261–266]. At high accelerating voltages, the electrons collide with the workpiece with high momentum. This creates extreme localized heating in the form of kinetic energy transfer. The metal heats rapidly until vaporization occurs. This is when the keyhole forms. The keyhole will either reach a steady-state depth (partial penetration) or melt and/or vaporize completely through the workpiece (full penetration). This is dependent on the thickness of the material, the beam diameter, the power, and the travel speed. A schematic of the process of a full penetration weld is shown in Fig. 44.

In partial penetration welds, the keyhole is very transient. It can oscillate and result in defects such as spiking, humping, and root porosity [265, 267–269]. Figure 45 illustrates the fluctuations of the keyhole in the partial penetration mode.

The keyhole is kept open by several forces. These forces are quite complex and are affected by the following phenomena: evaporated metal atoms, vapor pressure, friction, surface tension, electromagnetic force, thermocapillary force, electron pressure, and hydrostatic pressure [232]. The interaction of these forces is displayed in Fig. 46. For more information on

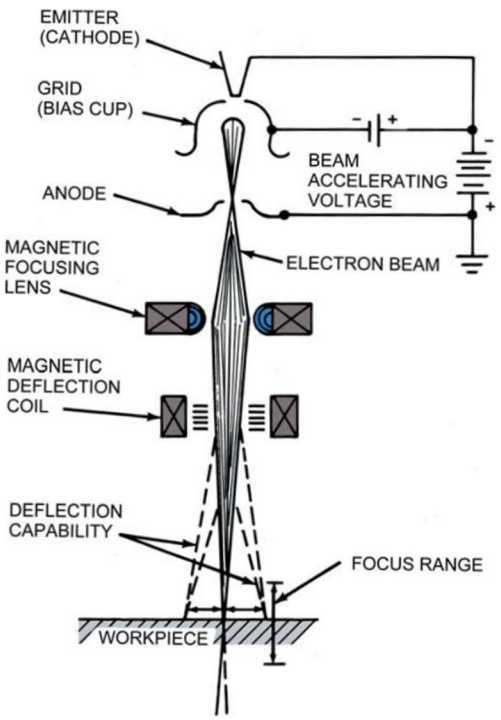

Fig. 39 Basic components of an EBW system [229]

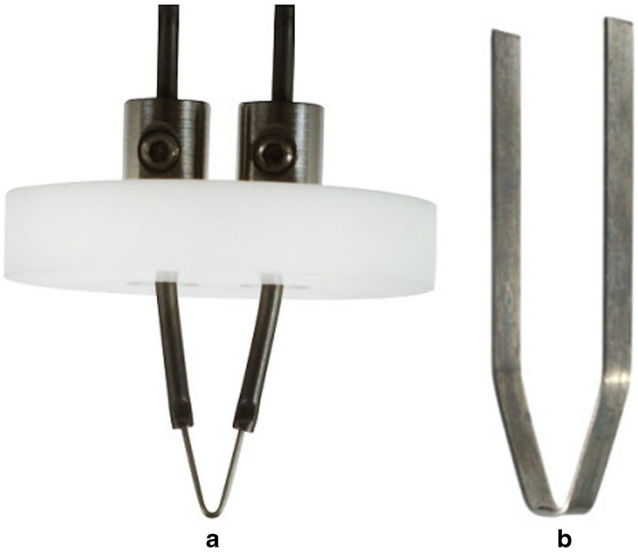

Fig. 40 Hairpin filament (a) and ribbon filament (b) [237]

keyhole formation, the reader is referred to Sections 1.2.2 and 1.2.3.

2.2.2 Effect of EBW parameters

Power Power is the product of voltage and current (P = V x I). Since voltage and current can be changed independently, similar powers can result in different weld characteristics. Low voltages and high currents result in low penetrating properties of the beam as well as a larger beam. This causes the weld geometry to be wide and shallow. Conversely, high voltages with lower currents produce finer, high-energy beams, resulting in weld pools that are much deeper and narrower [239].

The depth of penetration in electron beam welds increases linearly with increasing power [164, 270–276]. It can be seen in Fig. 47 that multiple experiments [144, 164, 271, 272] yielded similar results for electron beam welds of varying power in 304 stainless steel. It should be noted that all of these welds are at similar travel speeds, but beam diameter varies. The results from the authors of this review utilized a beam diameter of approximately 500 μm. Rai's [164] work varied the working distance, and therefore, the beam diameter from approximately 250–500 microns. Burgardt [271] and Giedt [272] do not provide beam diameters. It is interesting to note, however, that despite the difference in beam diameter the results in Fig. 47 fall within a distinct "band."

Beam diameter The diameter of the electron beam is important since it contributes to the power density and therefore the heat input. Smaller beams allow the workpiece to experience a higher local power density, which results in a deeper and narrower weld. This can be seen in Fig. 47 for Rai's [-164] work. With larger beam diameters, the welds did not penetrate as deeply. The lower penetrations in Fig. 47 are from slightly faster welds with larger beam diameters. It can be inferred from the figure that the beams used by Giedt [272] and Burgardt [271] likely had diameters of approximately 300 μm. Investigations into heat input also illustrated a linear relationship to penetration depth [277, 278].

Travel speed The electron beam interacts with a given point of the workpiece for a given time. This is dependent on the travel speed. Slower speeds result in more interaction and therefore deeper welds. This also widens the weld pool, resulting in a larger weld width on the surface. The relationship of penetration to travel speed at a fixed accelerating voltage is a reciprocal function as shown in Fig. 48 [279, 280, 281].

Focus At sharp focus, the beam is at the smallest diameter and therefore has the highest power density. However, slight underfocus will cause the focal point to be slightly into the workpiece (below the surface). Once vaporization of the metal occurs, the beam will appear to be at sharp focus below the top of the workpiece, and the deepest penetration can occur. Excessive underfocus will result in a lower power density, resulting in a decrease in penetration and an increase in weld width. Likewise, overfocusing the beam (above the surface of the workpiece) will produce a similar trend [250, 282].

Electron beam welds made at sharp focus will mainly produce keyhole mode welds. The exception to this is at very low powers or very high travel speeds. In general, conduction mode welding requires the beam to be defocused in order to reduce the power density [268]. For most commercial applications, a keyhole mode is desirable since this maximizes penetration and produces a stable weld. Conduction mode welding is used where only surface melting is desirable, such as for "cosmetic" passes after the initial, deep penetration weld is made. The purpose of a cosmetic pass is to smooth out the surface on the previous, deep penetration weld. This removes issues with high weld crowns or undercut and provides a weld surface free of sharp, geometric transitions and improves surface aesthetics. The conduction mode is also used when applying electron beam for additive manufacturing applications.

Deflection Beam deflection can be used to control the weld profile, microstructure, power distribution, and to accommodate the joint gap [242]. Different patterns will correspond to different weld properties. Common deflection patterns used are circular/sinusoidal, linear (perpendicular and parallel to the joint), or "figure 8"/"infinity." Deflecting the beam will result in different weld geometries, which can be seen in Fig. 49.

It has been observed that large deflection amplitudes and frequencies will decrease weld penetration [284–286]. However, beam deflection allows for better process control and ability to accommodate some welding concerns, including large joint gaps or to control (reduce) weld cooling rate.

2.2.3 Defects

Common electron beam welding defects include solidification cracking, porosity, undercut, spiking, and missed joints [269]. Electron beam welds are susceptible to solidification cracking due to the high stresses experienced from fast cooling rates and high aspect (depth/width) ratios. In particular, materials that solidify as a face centered cubic (fcc) phase (aluminum-base and nickel-base alloys, and some stainless steels) tend to be susceptible to solidification cracking. This normally occurs at the weld centerline. Some austenitic stainless steels can experience EBW solidification cracking due to the shift in solidification mode to austenite (fcc) at high solidification rates [201, 287]. To avoid solidification cracking in susceptible materials, if possible, it is advised to reduce travel speed, power, and allow for a preheat or controlled cooling rate, which can be done by beam deflection. The use of filler metal or shims can effectively control the microstructure and reduce solidification cracking through compositional changes.

Porosity can be an issue because of a keyhole instability or gas formation [288]. If a keyhole is unstable, it will collapse, forming a pore (or void) in the solidifying weld pool, ejecting spatter [287, 289], and leaving a concavity, as shown in Fig. 50.

Parameter optimization is necessary to avoid keyhole instability. Since the instability leading to porosity is often periodic, changing travel speed and power can mitigate the periodicity and alter (or eliminate) the frequency of pore formation [291]. Porosity can also be due to nucleation and growth of dissolved gases. These include hydrogen, oxygen and nitrogen. If a joint is not properly cleaned, it can leave contaminants (such as oxides) that, when welded, will form a gas pore in the fusion zone. To avoid this, the joint must be cleaned, and it is suggested to use a cleaning agent that does not leave a residue. Also, beam oscillation is a potential solution since it disrupts the nucleation and growth of the pores. It has been shown that porosity can be reduced or eliminated with a deflection pattern, but it is dependent on the frequency and amplitude of the deflection [284, 292–296].

Undercut can occur on the surface of electron beam welds, resulting in large stress concentrations. Kubo et al. [268] have investigated the effect of process parameters on weld appearance. It appears that as the power increases and focus is closer to sharp, both the underbead width and overbead height increases.

A missed joint is common for EBW since the pieces to be welded typically have little to no gap and the beam must be precisely located on the joint. Since the beam is quite narrow, the beam must be essentially parallel to the joint to avoid creating an incomplete fusion defect. This can be a serious issue since the weld surface may appear normal but the joint below the surface is not fully fused. Another problem can occur when the material being welded or the fixturing that holds it is magnetic, resulting in the beam being deflected or repelled away from the joint. To correct this, all equipment in the electron beam chamber should be demagnetized, and the joint must be carefully aligned. Another method for avoiding missed joints is to broaden the beam by means of defocus or deflection so that it is able to fuse the whole joint. This may not be possible in cases where penetration depth is a concern.

2.3 Vacuum effects

Most EBW is conducted under high vacuum since penetration and performance of the electron beam is optimized under “hard vacuum” conditions. Partial vacuum or non-vacuum EBW has been reported [244, 297, 298]. The advantage of partial vacuum EBW is usually related to economics where the amount of time required to pump down a large chamber is reduced. There are also situations where EBW is desirable for very large components where the use of a vacuum chamber is impractical. This section will discuss the role a vacuum plays relative to the beam and penetration characteristics.

2.3.1 Dispersion of beam

A high vacuum environment is generally used in EBW in order to minimize the interaction of the electron beam with the molecules that make up the atmosphere. This results in a smaller, more intense electron beam where the electrons are not scattered by particles in the atmosphere. High-vacuum practices are most common, with vacuum levels in the range from 10^{-6} to 10^{-3} torr (1.3×10^{-3} to 1.3×10^{-1} Pa). Medium-vacuum is classified as pressures in the range from 10^{-3} to 25 torr (1.3×10^{-1} to 3.3×10^{2} Pa), and non-vacuum as atmospheric pressure [299]. When using lower vacuum levels, the beam will begin to interact with atmospheric particles, causing the beam to spread and appear to be defocused. This can be seen in Fig. 51 which shows that when a better vacuum is maintained, the beam diameter can be reduced. The further the beam must travel in partial vacuum, the more particles it will interact with resulting in beam broadening. It should be noted that although the beam appears to become more diffuse from 500 to 250 torr, the number of electrons that can be seen is still higher, which is represented by a lighter color. The conditions shown in Fig. 51 represent the condition of medium-vacuum (5 torr) to non-vacuum (760 torr).

2.3.2 Effect on penetration characteristics

As stated earlier, the beam will appear as defocused as the quality of the vacuum decreases. This can be seen in Fig. 52, where the normalized penetration decreases at higher pressures (lower vacuum). Welds made under these conditions were characterized by percent penetration, where 100% is equivalent to a full penetration weld. It can be seen that the lower vacuum level decreases penetration, which is due to a lack of power density as the beam increases in diameter. A steep drop is noted around 1 torr (133 Pa) since there is a large

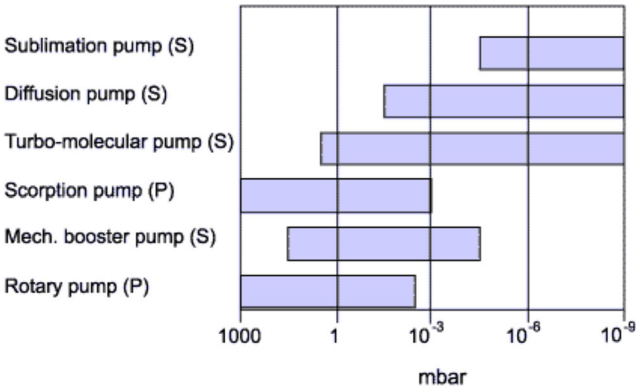

Fig. 41 Range of vacuum in which each type of pump is operable. Primary (P) can operate at atmospheric pressure. Secondary (S), requires some pumping before operation [235]

increase in atmospheric molecule interaction. Figure 52 also shows a larger variation in penetration with higher pressures. This is due to the variation of particle interaction as more molecules are present. Fewer interactions result in a more predictable beam diameter and power density.

Furthermore, as the vacuum level increases, the vaporized material escapes more readily, reducing the beam interaction with particles from the workpiece. As pressure increases, it is more likely that the metal vapor will form a particulate "cloud" above the weld, inhibiting the beam from reaching the material. The material agglomeration effects require more research; although, EBW non-vacuum could show plasma properties similar to a plume in laser welding [238].

Burgardt [300] has investigated the narrow field in the high vacuum section of Fig. 52. It appears that beam spot size and focal distance change with pressure in the range from 10^{-6} and 10^{-3} torr. With a better vacuum, the spot size actually increases. The change of spot size due to vacuum effects is also dependent on voltage. At lower voltages, the change in spot size is more dramatic. This is not thought to be a scattering effect, but instead a space charge effect. It is postulated that towards the higher end of the range analyzed, there are more particles to interact with the beam, and these particles will interfere with the repulsion of the electrons from each other [301]. Some other potential effects could be aberrations in electron optics and filament effects due to thermal spreading, but these are not thought to be significant in relation to changes in pressure.

Table 6 Comparison of advantages between LV-EBW and HV-EBW [89]. A "plus" indicates better properties relative to the other process, and a "minus" indicates reduced properties

	Low voltage EBW	High voltage EBW
Spot Size	-	+
Aspect Ratio	-	+
X-rays, Shielding	+	-
Electron beam gun	+	-

3 Laser beam welding

3.1 Fundamental principles of laser beam welding

Light amplification by stimulated emission of radiation (LASER) is the process of creating light with photons of the same phase and wavelength. Lasers are an energy conversion device that transform energy from electrical, optical, thermal, or chemical sources into a specific frequency of light within the electromagnetic spectrum [105]. Laser light is generated by exciting atoms or molecules that produce a very narrow band of electromagnetic frequencies (ideally monochromatic) with an in-phase electric field (coherent). Fundamentally, there are three components for laser generation:

1) Active/gain/lasing medium
2) Pumping source
3) Optical cavity/resonator

The active medium is where stimulated emission occurs, and the amplification of laser light is possible. When the atoms in the active medium are energized, the energy states of the outer electrons increase. A natural reduction in the electron energies causes an emission of a photon uncharacteristic of other photons produced in the medium. This is known as spontaneous emission. However, stimulated emission is when atoms or molecules have excess energy (i.e., electrons are in an elevated energy state), and an incoming photon causes emission of a photon that matches the phase, frequency, direction, and polarization of the incident photon [105, 106, 302].

By energizing or "pumping" the lasing medium via a light source or electrical potential, a condition arises where the atoms or molecules of the lasing medium are maintained at the higher energy state. This is known as the pumping source and can consist of light, electrical, chemical, or nuclear energy. For welding, most lasers are pumped via electrical or light energy. Light energy is generally produced with flash lamps or laser diodes. There are advantages of different pumping sources, such as diodes, to improve the useable lifetime and optimize absorption of pump light frequencies to improve pumping efficiency [106].

To further increase the laser output, the optical cavity reflects (resonates) laser light through the active medium to continue the stimulated emission process. The optical cavity allows for amplifying the laser light based on a positive feedback mechanism. There are many variations of optical cavities, but the premise behind the operation is to continually reflect photons using configurations of parallelly aligned mirrors or Bragg gratings in fiber optics [303, 304]. Continued reflection of the laser within the optical cavity will lead to a threshold where the gains in light amplification surpass the losses that simultaneously occur. This maintains a greater

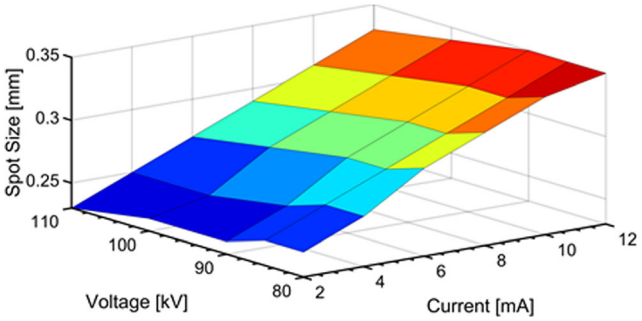

Fig. 42 Influence of accelerating voltage and beam current on electron beam spot size [253]

percentage of atoms in the excited state and is the "gain" of the laser. The greater percentage of atoms in the excited state (net gain >1) leads to what is known as population inversion [302]. Population inversion is created by the nearly instantaneous process of spontaneous emission, stimulated emission, and amplification [302].

High levels of laser energy can be focused to very small diameters (< 20 μm) by eliminating chromatic aberration, which is the inability to focus light composed of multiple wavelengths. With a single wavelength, low beam divergence is achieved, and therefore, power densities greater than 10^6 W/cm^2 can be produced for welding and cutting applications [106].

The following sections will compare laser and optic configurations currently used in welding applications. In addition, this section will review the physical phenomenon of laser/material interactions and how process variables and beam interactions influence weld geometry and penetration characteristics.

3.1.1 Types of lasers

Lasers are commonly referred to by the phase of the active medium. For the purposes of welding, this includes only high-power gas and "solid-state" lasers. Common gas lasers are carbon dioxide (CO_2) and excimer lasers composed of dimers (molecular complex consisting of two identical molecules linked together) of inert gases. Solid-state lasers generally refer to lasers that host the active ions within a crystal or glass and are optically pumped [326]. This includes rod lasers with a host material of glass or crystal doped with rare earth elements, such as a neodymium doped glass (Nd:glass) or a neodymium doped yttrium aluminum garnet (Nd:YAG). However, fiber and disk lasers also consist of a solid phase active medium doped with ions capable of stimulated emission, and diode lasers utilize doped semi-conductor electron-hole pairs to produce photons and stimulated emission.

Common lasers used in welding applications and their characteristics are summarized in Table 7 which compares the wavelengths, average power ranges, beam qualities, and "wall-plug" efficiencies. In Table 7, beam quality is defined by the M^2 value, and the reader is referred to Section 4.1 for an explanation on beam quality. The wall-plug efficiency is defined by the energy conversion ratio between the electrical input and the energy output by the laser beam.

The most common lasers used for welding include: CO_2, Nd:YAG (rod), fiber, disk, and diode. This is not meant to be an exhaustive list of lasers and excludes lasers not normally used in welding applications such as other dopants, host materials, and laser mediums. The various forms of laser operation such as continuous, quasi-continuous, or pulsed mode operation are lumped within the ranges of Table 7.

Lasers can be operated with an average or constant output power known as continuous wave (CW) operation or with pulses of output defined by a peak power, pulse width, and pulse repetition rate or frequency. The latter is known as pulsed mode or pulse welding operation. A technique to produce pulsed outputs is referred to as Q-switching, where "Q" stands for quality and is a ratio of the energy stored in the cavity to the energy lost per cycle [326]. This is the ability to pulse the laser output via an optical shutter [326] in frequencies between 0-50 kHz [106]. Many methods are used to employ Q-switching which can be mechanical, acousto-optical, or electro-optical such as Kerr cells or Pockels cells that change refractive index under an applied voltage [326]. However, Q-switching can significantly reduce beam quality as compared to CW output [307].

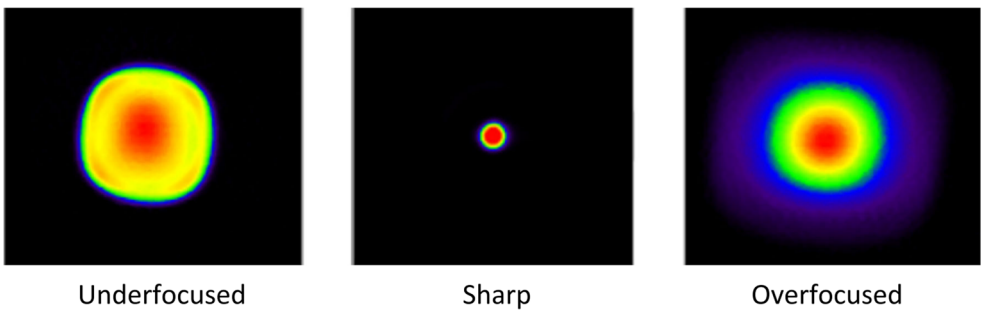

Fig. 43 Power distribution for different focus conditions of an electron beam with red indicating higher intensity [253]

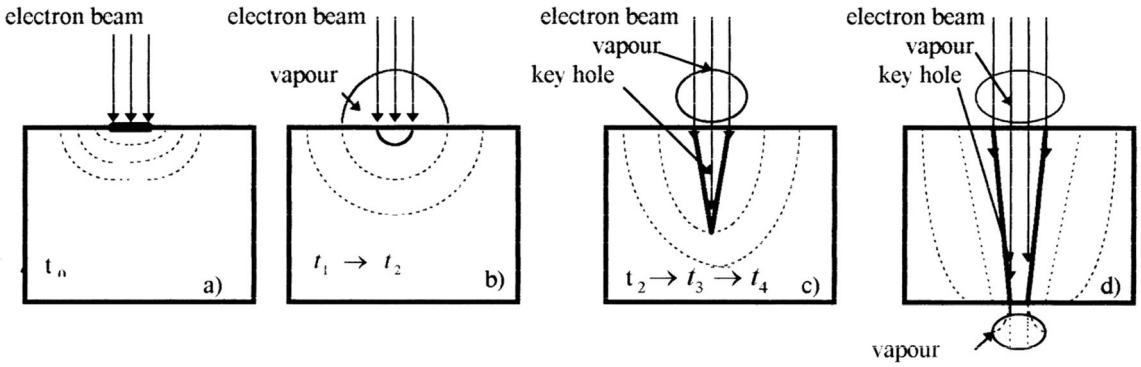

Fig. 44 Full penetration keyhole mode weld formation [263]

Beneficial features of pulsing the output include the ability to utilize low average laser powers to output high energies over very short durations (microseconds). A method to produce extremely short pulsed durations of femtoseconds (fs) or nanoseconds (ns) is called "mode locking." The premise behind mode locking is to produce a single mode or phase within the resonant cavity through constructive interference. Pulse durations are dependent on the speed of light and the length of the resonator [326]. Pulsing can have substantial benefits in welding applications, particularly in highly reflective, thin, and/or heat sensitive components or to improve mechanical properties through reduced grain growth [316]. However, there are also deleterious influences from pulsing such as extreme solidification rates and a greater propensity for solidification cracking [302].

CO_2 At the time of this writing, CO_2 lasers are much less popular in welding applications than in the early days after their introduction, but they are still commercially produced and used in some welding-related applications. The largest current application of CO_2 lasers is in cutting processes [318]. CO_2 lasers operate at a wavelength of 10.6 μm with a CW or average output power range of 0.5-45 kW [50, 106, 318]. CO_2 lasers also utilize additions of other gasses, such as N_2, He, and Xe, to improve efficiency, output power, and cooling [318, 319]. Most CO_2 lasers use a mixture of CO_2, N_2 and He. There are also multiple designs of CO_2 lasers such as slow axial flow, fast axial flow, and transverse flow designs and are distinguished by the operation/gas recirculation [105, 319]. Issues with beam quality, wall plug efficiency, and the inability to transport the beam through optical fibers are some reasons why CO_2 lasers were phased out with the development of newer laser technologies. The long wavelength leads to reduced energy absorption when welding reflective materials such as metals (see section 3.1.3), but 10.6 μm wavelengths can be advantageous for processing materials that are transparent to shorter wavelengths. Also, modes of electrical propagation produced via CO_2 sources, such as a ring-shaped intensity

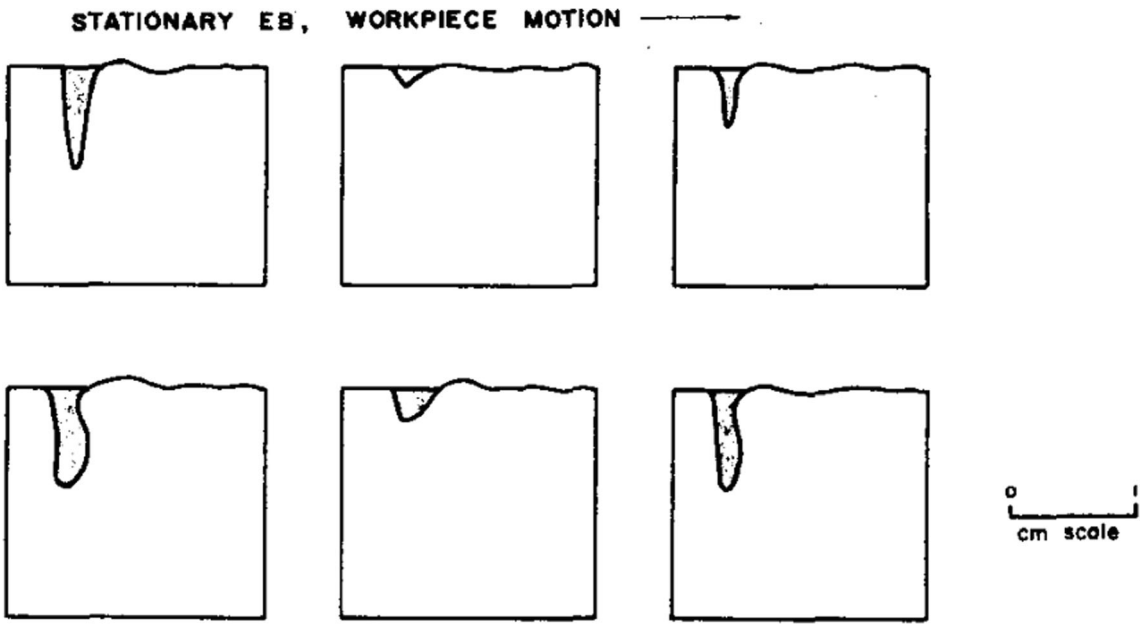

Fig. 45 Fluctuations of the keyhole in 1100 aluminum [265]

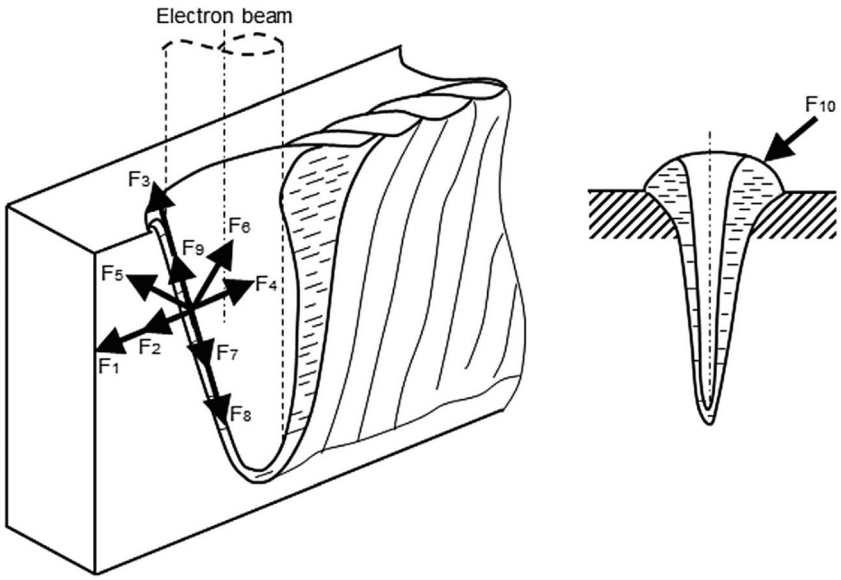

Fig. 46 Forces which maintain the keyhole. F1-force due to evaporated metal atoms. F2-force due to vapor pressure in keyhole. F3-friction between vapor and liquid films. F4-surface tension. F5-electromagnetic force. F6-thermocapillary force (temperature difference between front and back walls). F7-force due to electron pressure. F8-hydrostatic pressure. F9-thermocapillary force (front wall temperature gradient). F10-surface tension [232]

distribution [320], has enabled improved weld quality by reducing porosity and spatter generation [321]. This has helped continue the use of CO_2 laser sources within industry.

Nd:YAG Generally, the use of the term "Nd:YAG laser" refers to the lasing medium in the shape of a rod. The rod consists of an yttrium aluminum garnet (YAG or $Y_3Al_5O_{12}$) doped with the Nd^{3+} ion. The Nd^{3+} ion produces a characteristic wavelength at 1.06 μm. Excitation sources are krypton or xenon flash lamps or diodes. Flash lamps generate chromatic light and only a small fraction of input energy pumps the Nd:YAG rod. This leads to excessive heat generation and poor efficiency. Pumping via diodes can improve the wall-plug efficiency from 12% [106] to 30% [105]. The most efficient pump wavelength or absorption from Nd^{3+} ions is around 808 nm [106, 322], and this is a wavelength achievable via a GaAs or AlGaAs diodes.

Nd:YAG lasers have pulse capabilities [322], which allow for reducing heat input to reduce HAZ widths and better energy conversion in reflective alloys. A main issue with Nd:YAG lasers is the rod geometry causing low efficiency, thermal lensing, and susceptibility to thermally induced stress and distortion. These deficiencies led to the development of improved YAG crystal geometries such as slab designs [43] and disk lasers [58].

Neodymium glass Neodymium glass lasers are similar to Nd:YAG lasers and use the Nd^{3+} ion. However, the host material is glass and is advantageous as compared to YAG due to improved energy conversion and an ability to fabricate glass in a large range of shapes with high optical quality. The disadvantages to glass are broader Nd^{3+} emission lines and reduced thermal conductivity leading to overheating. [105, 106]

Diode Laser generation from semiconductors or diodes occurs from photon generation between an electrically charged p-n junction with a lateral waveguide. This fundamental principle of light production is the same as in light emitting diodes (LEDs), except

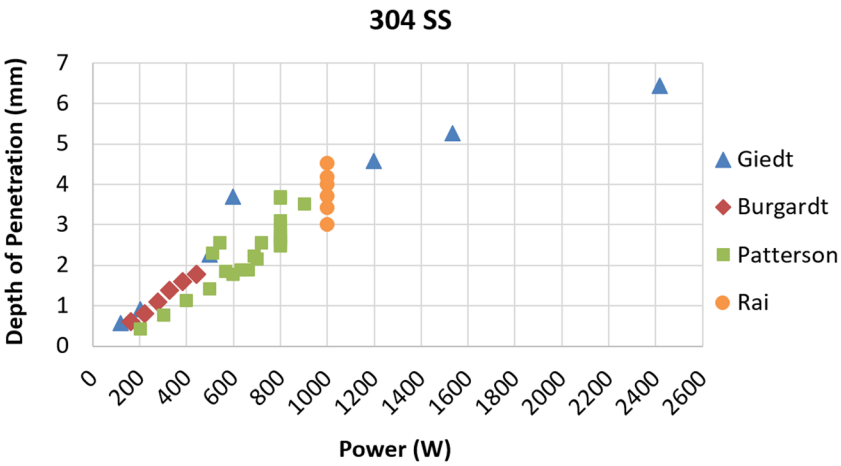

Fig. 47 Power versus depth of penetration for various 304 stainless steel experiments [144, 164, 271, 272]

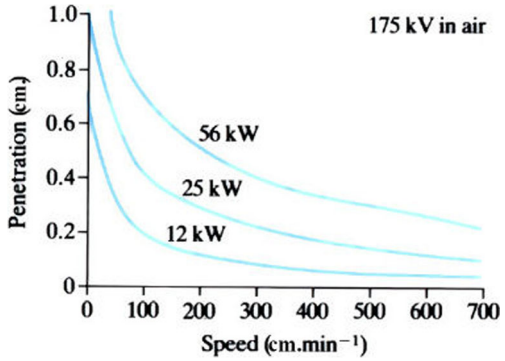

Fig. 48 Depth of penetration versus travel speed at different powers [279]

a single wavelength is produced and guided [105]. A substantial improvement with diode lasers is the energy conversion or wall-plug efficiency [58, 105]. Currently, the highest wall-plug efficiency occurs with output wavelengths between 880 and 980 nm [59]. Diode lasers are largely used as pumping sources for disk and fiber lasers because the wavelengths can be specifically selected to optimize absorption by the active medium and improve quantum efficiencies as compared to broad emission spectrum arc and flash lamps. Diodes are optimal for pumping solid-state gain mediums with 800-1100 nm spectral absorption bands due to the matching output wavelength and narrow emission band [58, 323]. Another major benefit to diodes is improving the pumping source lifetime to as high as 30,000 h [59] with some manufacturers advertising as high as 100,000 h [308]. This is a substantial improvement as compared to approximately 1000 h for flash lamps. In addition to a pumping source, diodes can be stacked with multiple, individual diodes to form arrays for increasing the total laser power. This allows for directly using diode lasers in welding applications. However, stacking diodes to form an array leads to poor beam quality, low brightness, and asymmetrically focused spots [105, 323].

The need to increase the size of the diode stack is a current limitation for direct diode welding applications. However, diode lasers have shown promising results when welding high reflectivity metals that are traditionally difficult to weld. Zediker et al. [317] reported coupling efficiencies of 65% when using blue light and coupling four diode modules together to produce 600 W of beam power and a beam parameter product of 44 mm*mrad. The reader is referred to Section 4.1 for the definition of beam parameter product (BPP). Currently, commercial diode lasers composed of several diode bar stacks coupled into an optical fiber are available with beam qualities as low as 30 mm*mrad at powers as high as 8000 W [324]. A significant advancement with diodes is quasi-continuous wave (QCW) operation. QCW lasers can switch the pump energy on for short durations and reduce the thermal load but maintain a laser output power close to steady-state.

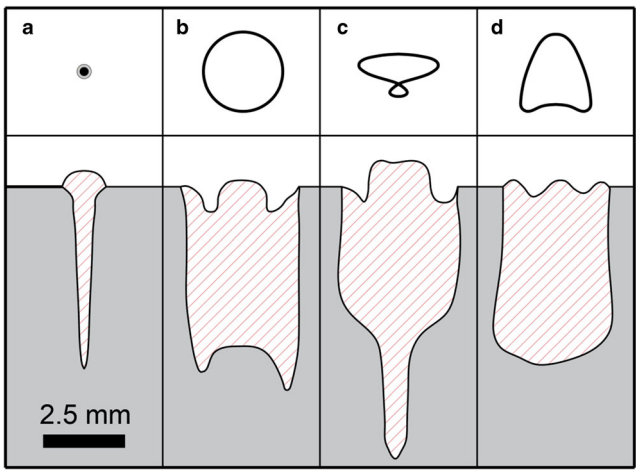

Fig. 49 Deflection patterns and corresponding weld geometries [283]

Disk The disk laser concept which was first developed in 1992 by Giesen et al. [43, 44] utilizes a thin disk geometry to allow cooling on one face of the disk. The cooled face is also an end mirror enclosing the optical cavity. This provides significant benefit to a rod-shaped design for reducing thermal gradients that will affect the laser propagation within the active medium. Heat extraction becomes very efficient by water cooling the end mirror side of the disk, and operation can occur at high volume power densities (1 MW/cm^3 [44]).

A popular active medium is the ytterbium (Yb^{3+}) ion housed within the YAG host crystal. The Yb^{3+} ion, as opposed to Nd^{3+}, has a three level pumping state with a long radiative lifetime and high thermal conductivity [44, 310]. Pumping is performed using laser diodes typically around 940 nm for Yb:YAG. The use of diodes for laser pumping substantially reduces the thermal load applied to the crystal allowing for significantly improved efficiency and beam quality as compared to Nd:YAG lasers [326]. Welding and cutting applications typically have beam parameter products ranging from 1 to 10 mm*mrad with powers from 1 to 16 kW respectively [52].

The disk laser is also capable of pulsed mode operation at pulse durations as short as picoseconds (ps) and femtoseconds (fs) with Yb^{3+} doped in other host materials [322, 325]. These short pulse widths are also achieved through mode-locking [326].

Overall, disk lasers have high efficiency, and compared to fiber lasers, they have a reduced cost and a decreased susceptibility to back reflections into the laser cavity [52].

Fiber Fiber laser generation occurs in a flexible, glass fiber that is doped with rare earth elements. Yb^{3+} is a common doping element which provides efficient energy conversion and a wavelength of 1070 nm [302]. The pumping source of a fiber laser can be other fibers or diodes and is performed by launching into the core or cladding of the fiber through end pumping or side pumping [314]. Coupling of light into the core can largely be affected by the location and geometry of the core, and therefore, other core geometries and multiple

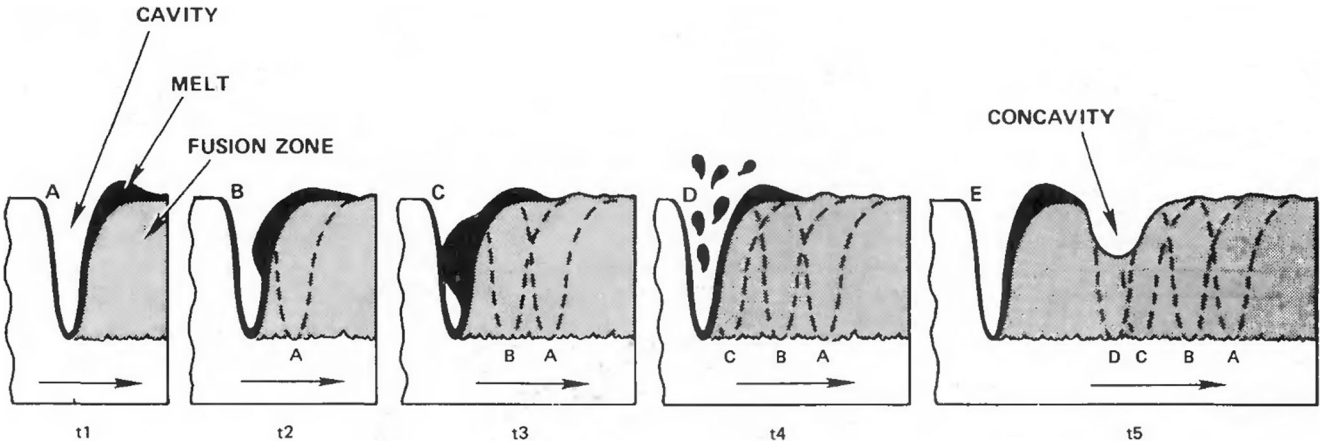

Fig. 50 Defect formation due to keyhole instability [290]

clad layers may be used to enhance coupling of the pump light [314, 327]. The resonator is contained within the fiber laser through fiber Bragg gratings (FBG) that are etched into the fiber to act as full or partial reflectors [302]. The FBGs work by altering the refractive index for passing and reflecting certain wavelengths. The rare earth elements Yb, Er, and Th have minimal attenuation within silica and are suitable dopants in fibers [327]. A schematic showing pumping sources (diodes) combined and launched into the Yb doped fiber lasing medium contained between two Bragg gratings is shown in Fig. 53. [304]. This single module can be coupled together with multiple modules (Fig. 53) to continually increase power to produce output powers in excess of 100 kW. Pumping of the fiber core by diodes can lead to wall-plug efficiencies of approximately 40% [315] to 50% [302].

An advantage of fiber lasers as opposed to other solid-state or gas lasers is the ability to generate a beam of exceptionally high quality (low beam parameter product) [105]. This allows for high power densities that are conducive for welding processes. Fiber lasers can also be Q-switched and mode locked for ultrashort laser pulse applications [327].

3.1.2 Optic configurations and beam delivery

CO_2 lasers are directed through the air to the final focusing optics and are severely limited by transport through fibers due to their wavelength. For example, commonly used silica (SiO_2) fiber optics are incapable of transmitting 10.6 μm wavelengths, and CO_2 lasers can only be transported through other materials, such as a thallium-based fibers [106], making welding impractical due to severe power restrictions.

Beam delivery for most solid-state lasers is through a silica fiber optic cable that can range in core diameter sizes from approximately 10–1000 μm [59]. The fiber optic cable provides a flexible means of transporting the beam and is easily applied in CNC and robotic welding applications. To facilitate single mode laser operation, which is the fundamental transverse electromagnetic mode (TEM_{00}) or Gaussian intensity distribution, small fiber diameters are used. These fibers are generally less than 50 μm to restrict the wave propagation to a theoretically single mode. However, it can be desirable to weld using different TEM modes or multi-mode for better energy distribution characteristics. Commonly, higher order

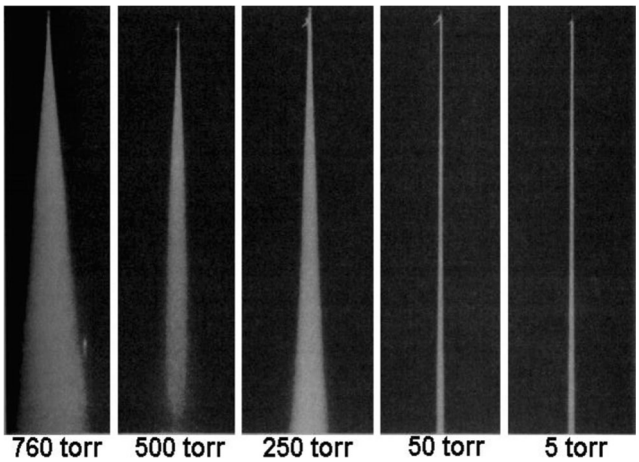

Fig. 51 Effect of vacuum level on size of beam [234]

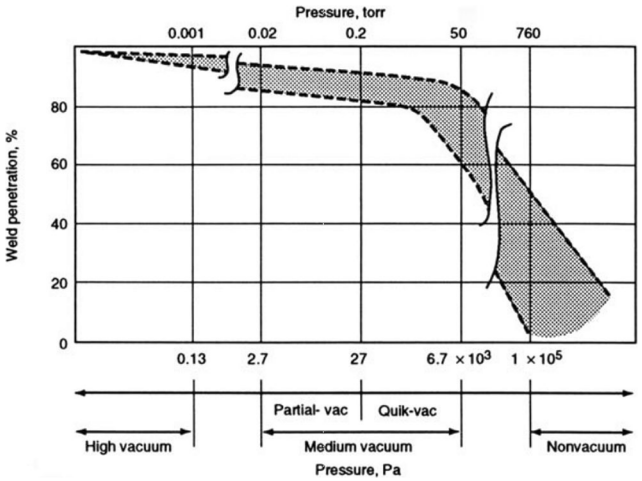

Fig. 52 Vacuum level versus percent penetration [234]

Table 7 Characteristics of lasers utilized in welding applications

Laser Type	Lasing Medium	Wavelength (μm)	Typical Average Power Range (W)	Beam Quality (M^2)	Wall-Plug Efficiency (%)
CO_2	CO_2-N_2-He gas	10.6	1k-20k [50, 106, 306, 337]	1-10 [50, 318]	5-15 [50, 106]
Lamp Pumped YAG	Nd^{3+}:$Y_3Al_5O_{12}$ rod	1.06	0.04-7k [106, 306]	8-100 [106, 307]	0.1-4 [106, 306]
Diode	GaAs, GaAlAs, InGaAs, etc. semiconductors	0.75-1.10	0.1-10k [59, 306, 308, 309]	1.2-800 [59]	30-73 [59, 106, 309]
Diode Pumped YAG	Nd^{3+}:$Y_3Al_5O_{12}$ rod	1.06	50-6k [306]	1.1-100 [106, 307]	8-12 [106]
Disk	Yb^{3+}:$Y_3Al_5O_{12}$ YVO_4 disk	1.03	100-16k [44, 310, 311]	1.3-30 [312, 313]	15-60 [306, 311]
Fiber	Yb^{3+}:SiO_2 fiber	1.07	100-30k [68]	1.3-8 [311, 314]	20-60 [302, 306, 315]

TEM modes are used and referred to as a "top-hat" distribution because of the uniform intensity that sharply drops to zero outside of the beam diameter. Differences in the intensity distributions for nearly the same power and 86% beam diameter are shown in Fig. 54. In this example, the difference in peak intensity is nearly five times greater for the Gaussian distribution. The latest advancements utilize manipulated beam profiles, such as a high intensity peak surrounded by a lower intensity ring [321], to change penetration characteristics and reduce defect formation. The reader is referred to Section 4.3 for beam analysis techniques, procedures, and measurement.

Reflective and transmissive optics Transporting, guiding, and focusing the produced laser requires optics that consist of many configurations but can be loosely categorized as transmissive or reflective. Transmissive optics utilize a lens or lenses produced from fused silica or CaF_2 and contain antireflective coatings to mitigate back reflections; while, reflective optics are composed of mirrors of copper, molybdenum, or gold for high reflectivity and decreased beam attenuation [105]. Except for CO_2 lasers, the optics consist of an initial lens that produces a column of light after the light exits the processing fiber (fiber transporting the beam from the point of laser generation). This collimating lens is usually defined by a number relating the distance between the center of the lens and the face of the optical fiber [328]. Following the collimating lens is the focusing lens to produce the desired spot size, which is directly proportional to the lens focal length [105].

The longer wavelength associated with CO_2 lasers does not allow transport through fiber optics or glass lenses and requires the use of reflective optics or zinc selenide (ZnSe) lenses. There is a benefit to reflective optics for all lasers, and this is to mitigate what is commonly referred to as thermal lensing. Thermal lensing [105, 106, 328, 329] describes the distortion of laser beams and shifts in focal positions or spot sizes resulting from the inability to cool the lenses at high laser powers and/or long laser illumination times. This causes thermal expansion and distortion of the lenses from the temperature gradients produced at high power [328–330]. It should be noted that "thermal lensing" is also used to describe thermal distortion in the lasing medium as in Section 3.1.1. These optics-related thermal distortions have been reported to increase beam diameters by over 100 μm within 50 s at 7 kW of power [329]. Miyamoto et al. [331] showed that thermal lensing could influence the focus and power density in CO_2 lasers using ZnSe lenses, and Blecher et al. [328] reported substantial changes to the focal length and beam diameter when producing welds with transmissive optics at 12 kW of beam power. By utilizing mirrors, heat extraction is easier to attain by applying water cooling directly to the back of a thin metallic mirror. This allows for steady-state temperature distributions to help mitigate thermal lensing effects. However, the use of water-cooled lenses further complicates and adds to the expense of the entire laser system.

3.1.3 Beam coupling and other "physics" considerations associated with the process

A major issue with using lasers to weld metals is coupling the laser energy into the workpiece to produce a satisfactory weld. The primary issues with energy transfer are based on the reflectivity of the metal being welded, the wavelength of light used for welding, and the interaction of the incident beam with the vapor plume that results from melting. The ability to apply the incident power into the workpiece is represented by the energy transfer efficiency [134, 173, 332]. This is calculated by the total heat input into the material divided by the laser energy incident to the material surface as shown in Eq. 2.

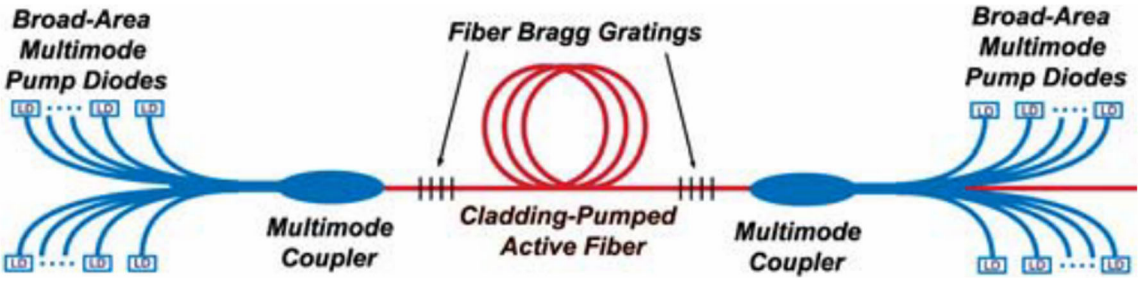

Fig. 53 Schematic of doped silica fiber laser pumped via diode sources [304]

LBW energy transfer efficiencies are relatively low in conduction mode (approximately 30%), but once a keyhole is established, the efficiency becomes 75–90% [332]. EBW, however, maintains a nearly consistent energy transfer efficiency (85–95%) [156, 173] and readily transitions into a keyhole welding regime. This high efficiency is because reflectivity and plume interaction issues are not inherent to a high vacuum, EBW process.

$$\eta = \frac{P_i}{P_0} \quad [unitless] \tag{2}$$

where: P_0 = power absorbed and P_i = total power

The energy transfer efficiency is not to be confused with the melting efficiency or melting ratio [173], which accounts for the power to melt a volume of material relative to the input power. A method to compute "melting efficiency" is defined by Ream [333] based on the weld cross-sectional area, travel speed, and power, as shown in Eq. 3. The weld process can also significantly influence efficiencies. Webber [334] showed that a pulsed (Q-switched) Nd:YAG laser could significantly improve melting efficiency as compared to a CW Nd:YAG laser at the same average power.

$$E = \frac{A_w v}{P_o} \quad \left[\frac{mm^3}{J}\right] \tag{3}$$

where: A_w = weld cross – sectional area, v = travel speed, and P_0 = total power input

Reflectivity Shiny metal surfaces at room temperature are highly reflective and lead to low absorption of laser light. Webber et al. [134] report that absorptivity based on calculations of the material emissivity at 300°C for 304 stainless steel is less than 15% and Ti-6Al-4V is approximately 15%. Conductive alloys such as aluminum are reported to have absorptivities between 2 and 3% [134]. However, this is dependent on the wavelength and alloy with absorptions reported as low as 1% for CO_2 lasers on aluminum alloys [105]. Reflectivity is higher at the longer wavelengths, and Xie et al. [335] reported three times the absorptivity at 1.06 μm (Nd:YAG) when compared to 10.6 μm (CO_2). A schematic of reflectivity versus wavelength for steel, Al, Cu, and Ni is shown in Fig. 55.

Absorptivity is proportional to the square root of electrical resistivity [134, 337]. As with conductivity, the reflectivity decreases as temperature increases. A further understanding of coupling beam energy into the workpiece can be described by the underlying physics of photons. It is believed that the emitted photons interact with free electrons near the metal surface [337] at approximately 10–100 nm of depth [131, 134]. The relatively large photon wavelength (0.5–10 μm), and lower energy, allows for reflection off the close packed and free electron material surface. Reflectivity is also dependent on the angle of incident light [106], and it is common to weld with a leading or lagging

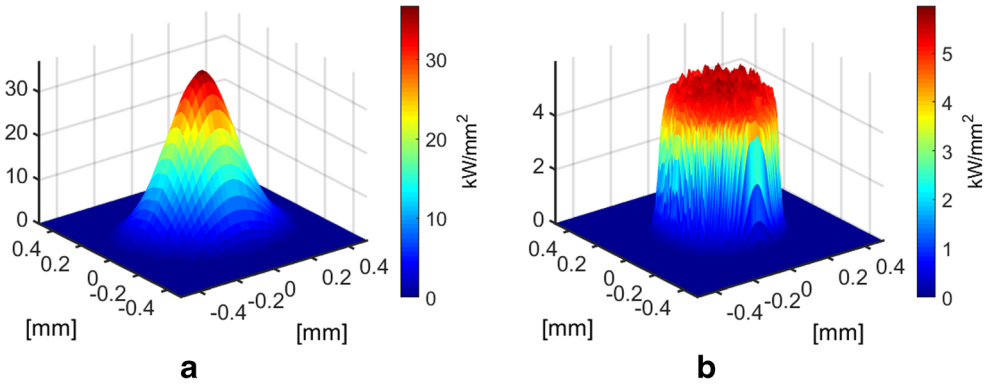

Fig. 54 Beam profile comparison between Gaussian (a) and multimode distributions (b) at 800 W of power at nearly a 500 μm beam diameter (86%) [144]

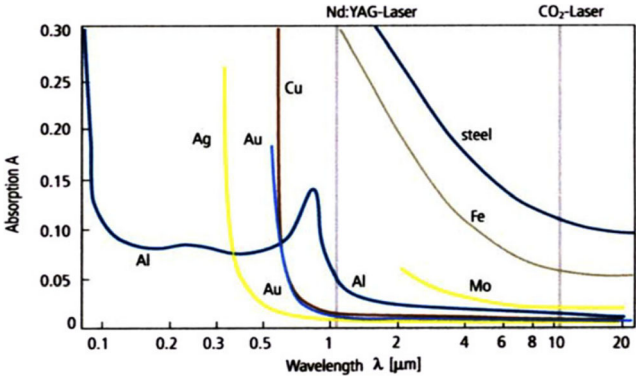

Fig. 55 Absorptivity versus wavelength for various metals [336]

weld angle to avoid excessive back reflections through the optics and into the laser [303, 338].

The poor absorption for LBW requires high threshold power densities [105, 131]. Reflections can be mitigated by selecting appropriate laser wavelengths to aid in absorption, using high power densities to form a deep-penetrating weld that will help to "trap" the incident light through Fresnel absorption [339, 340], or utilizing a surface preparation technique that minimizes reflection [341]. Absorption/reflection is a surface driven process, and coatings, films, or oxides [335] have been used to improve photon absorption. Xie and Karr [335] reported that increased oxide film thickness increased absorption when welding steel with a CO_2 laser. However, this can lead to substantially reduced mechanical properties due to increased oxygen levels in the weld metal. Another technique that was utilized was welding with a shorter wavelength laser followed by an infrared (IR) laser [342, 343]. This setup provided enough preheat via the shorter wavelength to allow for absorption of the IR beam.

At power densities significant enough to vaporize material and depress the molten weld pool, the laser is believed to be reflected and absorbed by the wall of the vapor cavity. This is referred to as Fresnel absorption [106, 141, 340] and is independent of the intensity. However, this does not mean that the intensity distribution of the incident beam does not influence the vapor cavity formation as shown by Volpp and Vollertsen [344]. Fresnel absorption is dependent upon wavelength and angle of incidence [141]. Kaplan [340, 345] reported absorptivity for common laser wavelengths based on the angle of incidence as shown in Fig. 56. It was also shown by Kaplan [345] that the tortuosity (roughness) of the liquid surface influenced absorption differently for 10 μm versus 1 μm wavelengths depending on the travel speed. High travel speeds for a 1 μm wavelength showed minimal influence on surface waviness. The readers are referred to References [141, 340, 345] for additional information.

Plume formation Due to the vaporization of elements during deep penetration welding, a vapor plume is generated above the keyhole. The issue with plume formation results from beam interaction with the vapor plume and the absorption, scattering, or radiation of the incident beam. Therefore, plume formation leads to attenuation (reduction in intensity) of the incident laser beam, which can lead to a loss in the energy transferred to the workpiece and a high degree of variability on the penetration depth. The degree to which the incident beam is absorbed is largely a factor of plume temperature and particle size for a given wavelength. Increasing temperature leads to higher absorption rates. Increasing power was shown to increase the amount of plume and its intensity near the vapor cavity or vapor capillary. Results from Gao et al. [346] for aluminum alloy 6061 are shown in Fig. 57.

The decrease in attenuation (percentage of incident power lost by the incoming laser beam) is commonly described by the Beer-Lambert Law as presented in Eq. 4 [347].

$$\frac{I_t}{I_o} = e^{-NLc_{ext}} \quad [unitless] \tag{4}$$

where: I_t = transmitted intensity, I_0 = incoming intensity, N = particle density, L = laser length interacting with the plume, and C_{ext} = extinction cross − section

Originally, the plume was believed to be a plasma (mixture of ions and free electrons) and was widely referred to as a plasma plume similar to arc welding [348]. This is largely due to the original plume studies using CO_2 lasers [349] and reports of plume temperatures as high as 17,000 K [350]. The formation of a plasma is dependent on the laser wavelength, and at 1.07 μm, researchers reported the plume to mostly be a thermally excited high temperature gas or weakly ionized plasma [351, 352]. This was shown by maximum plume temperature measurements between approximately 4000–6000 K [149, 150, 352, 353] with a plasma existing only with ionization potentials of a few percent. The large

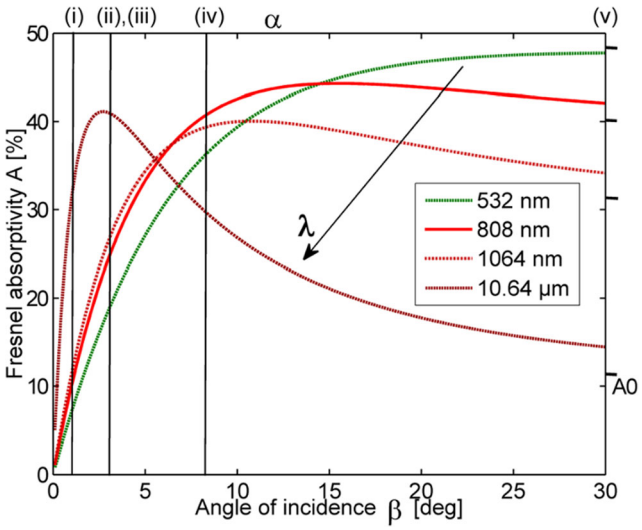

Fig. 56 Calculated absorptivity versus angle of incidence for molten iron at different wavelengths (arrow indicates increasing wavelength) [345]

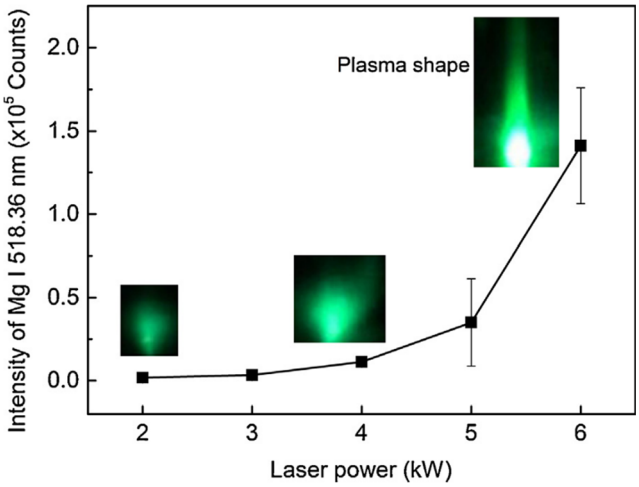

Fig. 57 Plume formation with increasing laser power in aluminum alloy 6061 [346]

difference in plasma formation is due to inverse bremsstrahlung effects associated with a 10.6 μm wavelength as compared to 1.06/1.07 μm wavelengths [141, 354]. This is shown with a wavelength dependency for the computation of the inverse bremsstrahlung absorption coefficient [149, 346, 350] and is reported to be about 100 times greater for CO_2 [147, 355].

Inverse bremsstrahlung occurs when the molecules or atoms within the plume are heated to a plasma. The free electrons within the plasma absorb the incident photons and cause the incident energy to mainly be trapped by the plasma plume above the keyhole. When the absorption exceeds the emission, the plasma is continually heated, and the longer wavelength of CO_2 causes greater absorption within the plasma [356]. The shorter wavelengths of solid-state lasers are less affected by inverse bremsstrahlung and most beam attenuation is believed to be caused by Rayleigh [352, 357] and Mie scattering [149, 357]. For a more in-depth explanation of inverse bremsstrahlung, the reader is referred to Reference [358].

Gao et al. [346] showed that fiber laser powers greater than 5 kW can significantly increase ionization potentials above 20%, and it was reported to be caused by inverse bremsstrahlung. However, this is contradictory to reports of other researchers such as Kawahito et al. [351] at 10 kW of laser power. Fabbro et al. [147] also reported that the inverse bremsstrahlung effect scales with a square of the laser wavelength. The shorter wavelengths associated with solid-state lasers allow for neglecting any inverse bremsstrahlung influences [147, 148]. However, beam scattering and attenuation can be associated with other physical phenomenon such as Rayleigh and/or Mie scattering.

Shcheglov et al. [149] and Zou et al. [150] defined the plume as consisting of two regions that included the weakly ionized vapor near the weld pool and a long plume of vapor particles within the beam path. Schneider et al. [359] made similar observations regarding the plume. A high-speed video image of the plume is shown in Fig. 58 with welding performed on mild steel.

As already mentioned, the influence of the near infrared light is based on Rayleigh and Mie scattering. Both mechanisms are dependent upon the size of particles that form within the plume and the wavelength of the incident light. Mie scattering occurs when the interacting particles are similar in size to the wavelength of incident light; while, Rayleigh scattering occurs when the particles are much smaller than the wavelength of incident light.

Scholz et al. [347] analyzed plume particle formation on 304 stainless steel using a 2kW fiber laser and reported that high vapor pressures aid in creating large particles. As shown in Fig. 59a, increasing power from 0.8 to 1.6 kW increased the average particle sizes from 8 to 15 nm respectively [347]. Also, higher welding speeds showed a slight reduction in particle size as in Fig. 59b. Similarly, Zou et al. [150] reported average particle diameters of 40 nm, and calculated results indicated particle sizes between 50 and 80 nm [149]. Particle size distribution was also shown to be dependent on the shielding gas with smaller particles produced with He or N_2 as compared to Ar [357]. These results indicate that Rayleigh scattering is largely attributed to beam attenuation and can have a significant influence on weld geometry and penetration.

3.2 LBW penetration characteristics

3.2.1 Parameter influences on weld penetration

There are many variables that must be considered when comparing the penetration characteristics of various laser welding

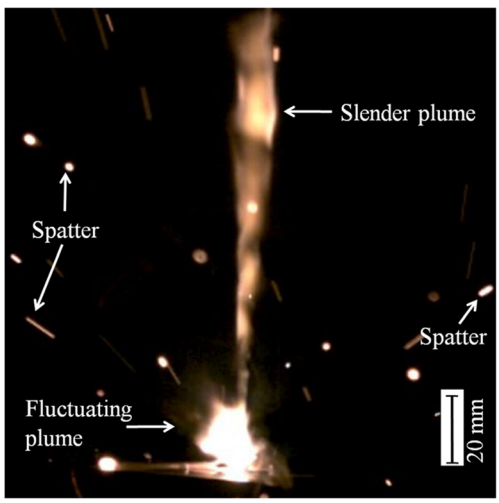

Fig. 58 High-speed video image of the plume on mild steel during laser welding at 5kW and 1.07 μm wavelength, with a 0.3mm spot diameter and weld speed of 2m/min [150]

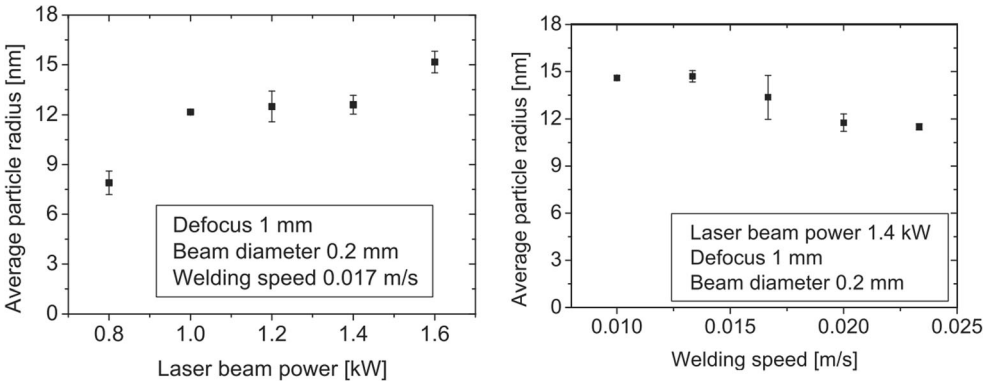

Fig. 59 Average experimentally determined particle radius versus beam power (a) and particle radius versus welding speed (b) [347]

processes. The following sections consolidate the information for CW and P-LBW.

Power and beam diameter (power density) It is difficult to decouple the analysis of beam power and beam diameter which often leads to weld analysis based on power density or power per unit area. At a constant beam diameter, it is reported that the depth of penetration increases nearly linearly with increasing beam power [134, 360]. There is an approximately linear relationship within keyhole welding between power and penetration at a fixed travel speed. This is consistent with results from numerous researchers [137, 164, 336, 360–362]. Figure 60 shows results of fiber laser weld penetration in steel alloys with increasing power [133, 336, 363]. These welding conditions utilized a top-hat beam distribution (see Fig. 54). The linear exception in this data is from the results using a 1.2 mm beam diameter (circles) and transfers from conduction to keyhole mode [133].

For P-LBW, peak power largely influences the penetration [302]. For Ti-6Al-4V, Akman et al. [190] showed a nearly linear increase in penetration depth versus peak power until a threshold power level was reached where there was no further increase in penetration. The departure from linearity was reported to be caused by beam interactions with the plasma plume [190]. Similar P-LBW results can be found from Bransch et al. [135] with increased power density at a constant beam diameter. When welding in conduction mode (lower power density or high travel speed), the penetration relationships are no longer linear [120, 133].

Beam diameter Beam diameter is a complicated variable that can lead to weld variations caused by different energy intensity distributions. Diameters are not always directly comparable because of energy density differences due to varying transverse electromagnetic modes (TEM), beam quality, and the method of measuring the diameter. The reader is referred to Section 4.1 for more information on defining beam diameters. However, reducing the diameter for a given analysis method at a constant power and travel speed will increase the intensity and result in deeper weld penetration [132, 364, 365]. Figure 61 shows that at twice the beam diameter (0.6 mm versus 1.2 mm) and nearly comparable travel speeds (≈50 mm/s), there is a substantial change in penetration indicated by the circles versus the left pointing triangles. It is interesting to note that these penetration results are at nearly the same power density. However, the 1.2 mm beam diameter [133] remains in conduction/transition mode versus the 0.6 mm beam diameter in keyhole mode. This illustrates how solely comparing power density is insufficient.

Travel speed Slower travel speeds increase the overall energy and heat input deposited into the workpiece. This causes the weld pool to widen and reduces the weld aspect ratio [105]. Penetration is reported to exhibit an exponential decrease with increasing travel speed [105, 360]. There is a substantial amount of literature published that plots the LBW relationship between penetration and travel speed [105, 120, 132, 302, 336, 349, 360, 366]. Figure 61 shows the exponential decay with increasing travel speed based on results from CO_2 lasers. Baardsen et al. [360] reported that laser welding penetration depths do not show a corresponding relationship between penetration and travel speed. This was based on the idea that

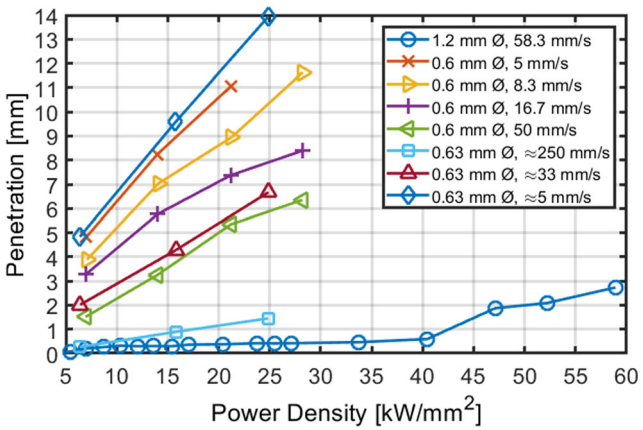

Fig. 60 Fiber laser penetration versus power for steel alloys [133, 336, 363]

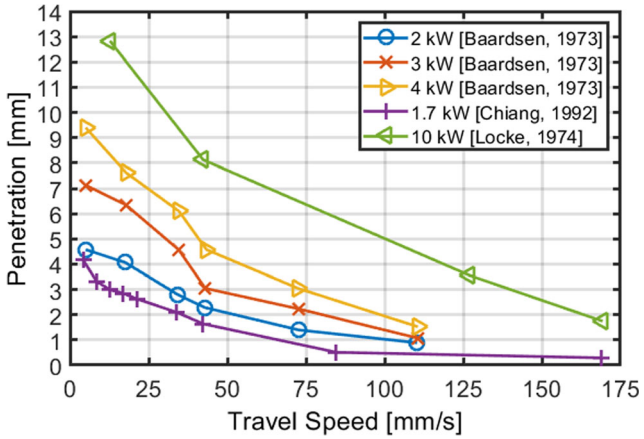

Fig. 61 Penetration versus travel speed for CO_2 lasers operating in keyhole mode [120, 349, 360]

higher travel speeds require some amount of "illumination time" to form a weld pool. Therefore, reflectivity becomes greater with higher speeds and less energy is "captured" within the keyhole [360]. The complexity of the travel speed is exacerbated by laser plume interactions [168, 356, 367–369], which is also dependent on travel speed [349]. Although, CO_2 lasers have much greater plume attenuation than near 1 μm wavelengths, the relative trend is the same for shorter wavelength lasers as shown in Fig. 61.

Travel speed also changes the shape of the weld profile with higher travel speeds resulting in reduced penetration and a narrower weld as viewed on the surface of the workpiece [105]. Figure 62 shows the influence of increasing travel speed on Type 304 stainless steel at 1400 W of beam power. The change in weld penetration is much more pronounced than the change in weld width for these welding conditions, and it is believed that a transition occurs between keyhole to conduction mode between 75 and 100 mm/s.

Pulse parameters Pulsed laser welding introduces additional parameters including peak power, pulse width, and pulse frequency. Pulsed waveforms with increased complexity are also useful for applications attempting to improve coupling efficiencies [370], reduce porosity, or improve the weld surface appearance [302]. For linear welds, the combination of frequency and travel speed determines the percentage of pulse overlap to maintain required strength (cross-sectional area) or hermetic seal requirements. The relationship to describe percent overlap is shown in Eq. 5 [371].

$$\%overlap = \left[1 - \frac{\left({}^{v}/_{f}\right)}{(d + vt)}\right] x100 \tag{5}$$

where: v = travel speed, f = frequency, d = spot diameter, and t- = pulse duration

P-LBW can be advantageous compared to CW by significantly increasing penetration for the same average power. It is also an effective method for reducing the overall heat imparted to the workpiece. Assuncao and Williams [372] showed increased weld depth at consistent interaction times and power densities between P-LBW and CW-LBW as shown in Fig. 63. The difference in the penetration was dependent on the interaction time, and shorter interaction times resulted in larger differences. Figure 63 also shows the linear relationship with power and penetration for P-LBW and essentially no or negligible transition region is apparent between conduction and keyhole mode.

As with CW welding, Kumar and Sinha [214] showed a linear relationship between the calculated heat input and cross-sectional area of the fusion zone area in Ti-6Al-4V. Fuerschbach and Eisler [373] analyzed pulse duration with increased "energy intensity" (pulse energy divided by spot diameter, J/mm). Comparing equivalent energy intensities, a shorter pulse duration produced greater penetration.

Beam manipulation The use of galvanometer-based scanning optics allows for manipulating laser beams in various configurations such as circles, longitudinally with travel direction, transversely with sinusoids, and "figure 8" patterns. This introduces an additional three variables to the laser welding process including: pattern, amplitude, and oscillation frequency. Benefits to beam oscillation or "wobble head" welding may involve changes to weld penetration and width [374, 375]; improved joint fit-up tolerances [375, 376]; reduced porosity [377]; microstructural refinement [378]; and greater process control when welding dissimilar metals. Issues arising from beam oscillation can include widening of the HAZ [378], increased spatter [376], and undercut [374]. Mrna et al. [379]

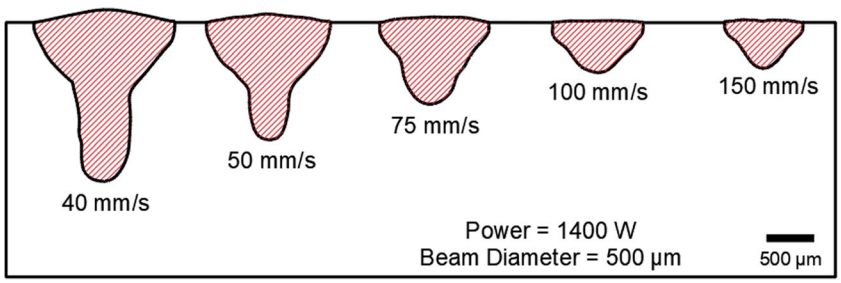

Fig. 62 Change in weld geometry on 304 stainless steel using a multi-mode beam profile at sharp focus [144]. An apparent change from keyhole to conduction mode occurs above 75 mm/s

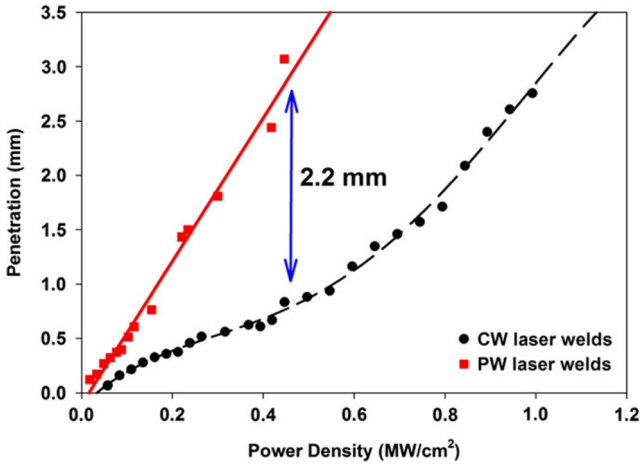

Fig. 63 Comparison of P-LBW and CW-LBW penetration at an interaction time of 20 ms and ≈0.9 mm beam diameter [372]

showed that beam oscillation causes significant variability in the vapor capillary and weld pool flow. This transient nature of the keyhole may introduce defects depending on the welding parameters. Higher frequency (200 Hz) compared to lower frequency (100 Hz) circular oscillation resulted in reduced spatter as shown by Fetzer et al. [377].

Wang et al. [378] reported a decrease in grain size at the weld centerline when beam oscillation is used for an aluminum alloy. The greatest grain refinement occurred with a circular oscillation at a diameter of 1 mm and frequency of 180 Hz. The refinement is believed to be caused by fragmentation of the solidifying dendrite tips at the trailing edge of the weld pool, resulting in heterogenous nucleation sites for new grains as shown in Fig. 64 [378].

Other variables Other variables related to the baseline beam parameters that can influence weld penetration include, 1) interaction time [132, 134, 365, 380, 381]; 2) specific point energy [365, 381]; and 3) energy density [365]. The interaction time includes the travel speed and diameter of the beam across the surface of the work piece assuming the centerline of the beam spot parallel to the travel direction [134, 363, 366, 382]. The interaction time is then calculated by the beam diameter divided by the travel speed as shown in Eq. 6. Fundamentally, the interaction time is only accurate at the weld centerline because moving outward from the circle center (assuming a circular beam) reduces the length of the beam applied to a specific point. However, Suder and Williams [132, 363] assumed that the effects on a beam radius are negligible for small spot sizes, and multiple researchers have incorporated interaction time into weld width and penetration analysis [132, 365, 382].

$$t_i = {}^{d_b}/_{v} \qquad [s] \tag{6}$$

where: t_i = interaction time, v = travel speed, and d_b = beam diameter

The specific point energy (SPE) calculation is shown in Eq. 7, and this is defined by the energy computed from the power and interaction time. At the weld centerline, this represents how much energy is exposed to an infinitesimally small point.

$$SPE = Pt_i \qquad [J] \tag{7}$$

where: P = power and t_i = interaction time

The interaction time is believed to be comparable to a pulse used in P-LBW applications where the interaction time can be thought of as the pulse length or period of radiation in the CW LBW process. Suder and Williams [363] analyzed the influence of a constant interaction time for bead-on-plate welds using a fiber laser. When maintaining a constant interaction time, the depth of keyhole penetration increased linearly with an increasing power density. This data is consistent with prior results (Fig. 60) showing increased penetration at higher power with a fixed beam diameter and travel speed [105, 137, 164, 336, 361, 362]. Suder and Williams [363] reported that some length of interaction time is required to establish a keyhole for a given power density, and it was reported that there is a need for a threshold energy density to elevate the material to its boiling point for transitioning into keyhole welding. Energy density can be calculated by the power multiplied by the interaction time as shown in Eq. 8.

$$Energy\ Density = P_d t_i \qquad \left[J/mm^2\right] \tag{8}$$

where: P_d = power density and t_i = interaction time

Weld defects Porosity and solidification cracking are major issues inherent to HED processes. Porosity defects are associated with substantial vaporization, rapid solidification, and vigorous weld pool stirring; while, solidification cracking is an issue with rapid solidification rates, alloy composition effects, and internal shrinkage stress.

Porosity is considerably more significant in deep penetration welding (higher power densities) and with certain alloy systems such as aluminum [139]. Two basic types of porosity form, which include root porosity (keyhole collapse) and uniform porosity (gas entrapment). Norris et al. [383] and Blecher et al. [384] showed that increased weld volume/area increased the amount of porosity that formed for CW LBW. For P-LBW, porosity formation is largely dependent on the power modulation and the pulse parameters utilized. Matsunawa et al. [385] showed that lengthening the trailing edge of the pulse was able to reduce weld porosity by slowing keyhole collapse and gas entrapment. LB-PBF is an active area of research on porosity analysis and minimization techniques to reduce and avoid defects in AM parts. Results show that higher powers at a given scan speed result in reduced

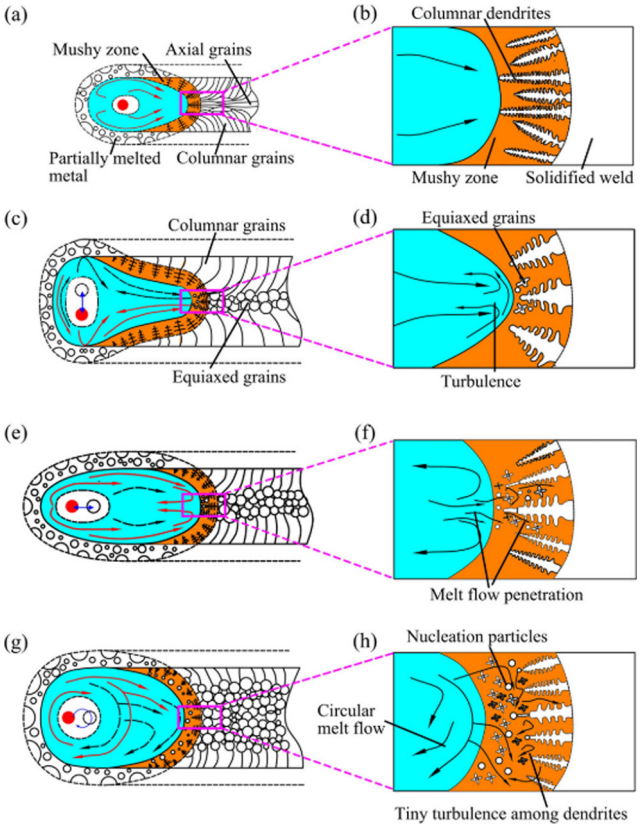

Fig. 64 Schematic illustrating potential melt flows and dendrite solidification for different oscillation patterns when welding aluminum. None (a, b), transverse sinusoid (c, d), longitudinal (e, f), circular (g, h) [378]

porosity during selective laser melting (SLM) of Ti-6Al-4V [386, 387].

As with EBW [209], CW LBW can be susceptible to solidification cracking and is exacerbated with unfavorable solidification conditions and high shrinkage stresses. For example, for austenitic stainless steels such as Types 304 and 316, solidification as austenite tends to promote solidification cracking versus solidification as ferrite. Also, high aspect welds with distinct centerlines tend to increase susceptibility to cracking.

P-LBW is inherently more susceptible to solidification cracking due to higher solidification rates associated with low average power [388, 389]. However, modification of pulsing parameters by increasing frequency or modifying pulse waveforms can reduce solidification cracking tendencies [388, 389]. Reduced crack susceptibility was also reported by Olsen [370] with high repetition rates, larger overlap, and greater weld depth.

"Humping" is an issue when welding at extreme travel speeds [390–393] and is usually preceded by "ropy" beads and undercut [393]. Kawahito et al. [392] showed that humping is exacerbated with smaller beam diameters (130-200 μm) and higher travel speeds (>75 mm/s). Because surface tension and Marangoni flows are believed to significantly influence humping, material composition can largely influence formation of a high and discontinuous weld face.

3.2.2 Vacuum (or reduced pressure) effects

The following section discusses LBW under reduced atmospheric pressure. Although LBW is usually conducted at ambient pressure, welding in high or partial vacuum can significantly influence weld penetration.

Penetration and weld width The influence of laser welding under vacuum was first analyzed for CO_2 lasers. Arata et al. [394] initially showed significant increases in CO_2 laser weld penetration under vacuum conditions. Katayama [368] also increased penetration depth during YAG laser welding at reduced ambient pressure. The trends in penetration characteristics with decreasing vacuum levels are consistent among researchers using various laser types and alloys [146, 147, 356, 369, 390, 395]. Reports have stated that vacuum LBW can improve penetration depth by a factor of two [394, 396] to four [397] times compared to atmospheric conditions. Katayama et al. [390] achieved penetration as deep as 73 mm in Type 304 stainless steel when welding in an under-focused condition at a pressure of 0.1 kPa (0.75 torr) [390].

A schematic representing the trends of penetration and welding speed for a given laser process, power, and beam diameter as a function of atmospheric pressure is shown in Fig. 65. At higher travel speeds, there is less influence on increased penetration with decreasing pressure [390]. At low pressures, penetration no longer improves. This vacuum level, known as a critical threshold, is reported at pressures as high as 10 kPa (75 torr) but can be influenced by the alloy, wavelength, power density, and travel speed. High travel speeds in excess of 3 m/min (66.7 mm/s) may exhibit critical thresholds at or near atmospheric pressures [390, 395].

Lower pressures also influence aspects of the weld other than penetration. The weld widths are reported to decrease [390, 391], and the weld geometries become comparable to EBW [147, 356, 367, 396]. Fig. 66 [356] shows laser beam weld cross-sections at pressures of 100 kPa (750 torr) and 0.01 kPa (0.75 torr). There is a substantial decrease in the weld toe width with increased penetration. For comparison, there is also the cross-section of an EB weld at an equivalent power [356].

A main mechanism for increased LBW penetration in reduced pressure is the reduced interaction of the beam with the plume. A schematic representing how the plume changes with reduced atmospheric pressure is shown in Fig. 67 from Luo et al. [391]. Experiments to analyze plume characteristics in reduced vacuum environments have used 1) x-ray imaging [394]; 2) standard photography [367, 395, 398]; 3) high speed

imaging [150, 369, 391]; and 4) transmission of probe lasers through the plume/process beam [150, 390, 391, 398]. All of these techniques have verified the reduction in beam/plume interactions under reduced pressure conditions.

The open literature contains contradictory information as to what degree the plume influences beam attenuation for fiber lasers at 1070 nm wavelengths. Kawahito et al. [352] reported a maximum attenuation of 4% measured at 3 mm above the plate surface using a 10-kW fiber laser. These results were for welds on austenitic stainless steel at atmospheric pressure. Their conclusions state that the "weakly ionized plasma" was insufficient in reducing weld penetration [352]. Similarly, Zou et al. [150] reported a maximum attenuation of 5% in atmosphere when welding on mild steel. Figure 68 shows the maximum attenuation around 13% for an aluminum alloy [398] and 20% for a high strength low-alloy steel [391] and the probe laser attenuation decreasing further below atmospheric pressure. These results show significantly higher beam attenuation at atmospheric pressures (~100 kPa), and the attenuation can be dramatically decreased through reduced pressure.

Contrary to other published results, Greses et al. [357] reported maximum attenuations up to 40% when analyzing Nd:YAG CW LBW in atmosphere. Some issues in plume attenuation analysis using a horizontal probe laser are attributed to plume fluctuations or temporal instabilities [242, 355, 357]; probe diameters relative to beam analysis; and a reduced length of beam propagation through the plume. By propagating a probe laser transversely through to the incident beam, the attenuation through the appropriate length of beam is not comparable to the incident beam. Nonetheless, there is a clear decrease in attenuation with reduced ambient pressures, and different alloys will have different vaporization pressure/temperature curves that lead to variable plume generation [362]. It was shown by Chiang and Albright [349] and Zou et al. [150] that reducing the height of the plume available to interact with the beam improves penetration.

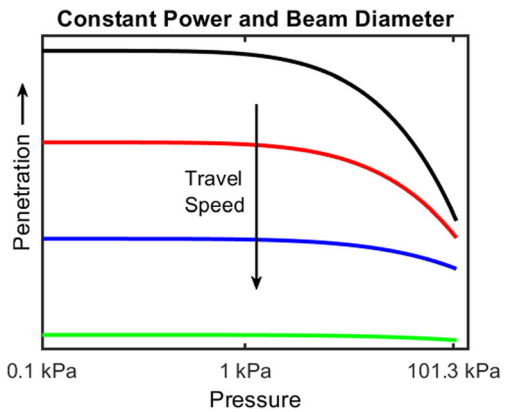

Fig. 65 Schematic showing LBW penetration versus pressure at a constant power density and increasing travel speed. Data interpreted from references [147, 390, 394, 395]

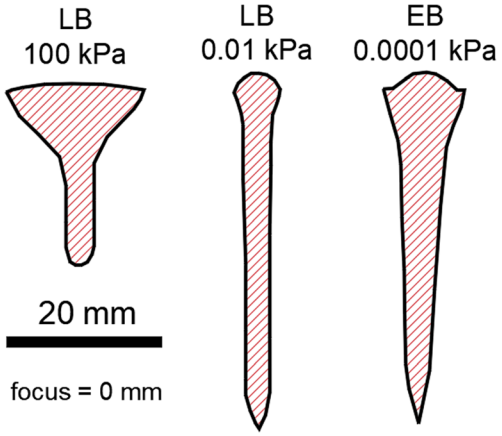

Fig. 66 The effect of pressure on S355 steel welded at 16 kw and 0.3 m/min (5 mm/s). LBW at 100 kPa, LBW at 0.01 kPa, EBW at 0.0001 kPa [356]

At nearly atmospheric pressure, heat distribution is substantially different near the weld surface. This plume interaction and energy absorption at the weld surface distributes the heat and reduces the propagation of the incident energy further into the workpiece. At low pressures, the plume can no longer interact with the beam and distribute heat outwards along the surface. Thus, the incident laser energy is no longer absorbed and scattered by the plume.

The advantage of reduced pressure LBW in comparison with EBW is the ability to substantially increase penetration at moderately low vacuum levels, such as 1 kPa (7.5 torr). In contrast, EBW requires much lower vacuum pressures (<0.1 torr) to minimize electron-molecule interaction that results in extensive beam attenuation [356, 396]. Thus, with LBW, even small reductions in atmospheric pressure can provide significant improvement in penetration.

Because of the nature of the process, such as beam delivery by fiber optics, the ability to use partial vacuum conditions for LBW is apparent. LBW can achieve faster pumping times along with decreased complexity of vacuum systems. An additional benefit for improved weld penetration in partial vacuum environments is the ability to utilize local vacuum or partial vacuum units that move with the welding optics [399, 400]. These "mobile enclosures" open the possibility for low pressure LBW by reducing capital costs and allowing for welding of large components [399].

Porosity In addition to increased penetration, reduced pressure was shown to significantly reduce weld metal porosity [338, 368, 397]. An example of this is shown in Fig. 69 [338]. Cai et al. [338] reported that the change in porosity is influenced by liquid flow along the keyhole wall and due to greater keyhole stability. Elmer et al. [397] reported differences in the morphology of the pores under vacuum conditions. Under atmosphere, the pores were large; while under vacuum, the pores were much smaller but greater in number.

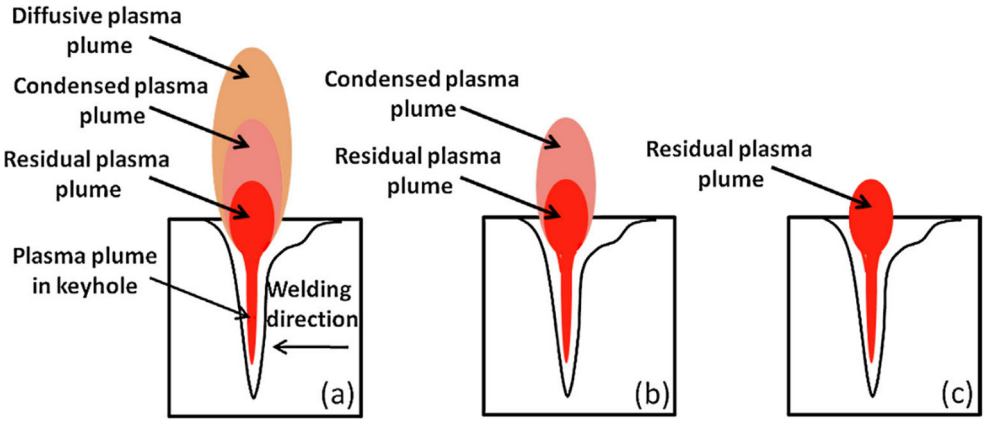

Fig. 67 Schematic representation of laser plume at reducing pressures. 101 kPa-80 kPa (a), 80 kPa – 20 kPa (b), 20 kPa-3 kPa (c) [391]

Humping Vacuum conditions are reported as increasing the tendency for humping. Both, Lou et al. [391] and Katayama et al. [390] reported an increase in humping at lower pressures (≤ 1 kPa). Although, Katayama et al. [390] reduced humping at low pressures by welding in an under-focused condition (i.e., with the beam waist significantly below (>20 mm) the plate surface). The same results were obtained by Börner et al. [395] at vacuum levels below 0.1 kPa and velocities greater than 12.5 mm/s. Elimination of humping occurred when under-focusing by 8 mm.

3.2.3 Plume suppression

Plume suppression techniques are commonly utilized in LBW to remove the vaporized particles from the beam path using a jet of gas. This is generally considered to be a more practical and cost-effective method to improve weld penetration as compared to welding under vacuum. Generally, this consists of compressed air, N_2, or Ar directed orthogonal to weld direction and through the beam. This stream of gas (sometimes referred to as a "cross-jet") aids in removing metallic particles and allowing for less photon-particle interaction, and therefore, reduced beam attenuation.

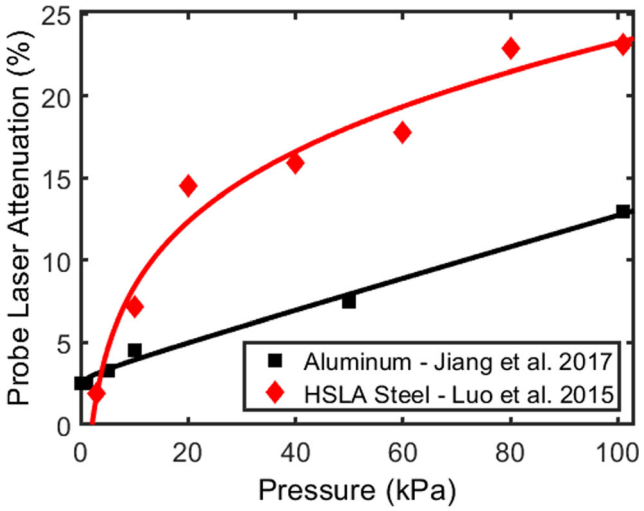

Fig. 68 Variation of laser attenuation versus atmospheric pressure for fiber lasers at a wavelength of 1070 nm. Differences in plume attenuation are shown at a 1 mm height for an aluminum alloy (squares) [398] and at a 3 mm height for a high-strength low-alloy steel (diamonds) [391]

Chiang and Albright [349] (CO_2 laser) and Zou et al. [150] (fiber laser) showed that reducing the height of the cross-jet above the workpiece improved weld penetration. With the cross-jet applied close to the weld surface, most of the plume is ejected out of the path of the laser resulting in less beam attenuation and deeper weld penetration. These results are shown in Fig. 70 and have an exponential decrease relative to cross-jet height [150]. As with the vacuum results, the influence is greater at slower travel speeds [349].

Flow rates Schneider et al. [359] showed variation in plume suppression under two different argon flow rates with lateral gas flow. Increasing the flow rate from 10 to 50 L/min reduced the plume height from approximately 30 mm to 10 mm, respectively [359].

Gas compositions Different gases within the plume may change particle agglomeration and alter ionization potentials which can lead to variations in weld geometries. Chiang and Albright [401] produced varying penetration based on the shielding gas utilized. The deepest penetration was achieved using He (highest ionization potential), followed by CO_2 and Ar. Greses et al. [357] reported that there was minimal difference in particle sizes when comparing Ar, He, and N_2 shielding for a Nd:YAG laser, and the best transfer efficiencies were obtained using an Ar cross-jet versus He and N_2 [357].

4 EB/LB process characterization and monitoring

Producing electron and laser beam welds that perform as intended for a given application starts with understanding and quantifying the total power and beam distribution

(characteristics). HED beams develop non-ideal shapes during generation, propagation, and focusing, and beam distributions and divergence angles directly influence weld geometries, process robustness, and the propensity to form undesirable discontinuities and/or defects. Therefore, understanding the "actual" power and power distribution through beam characterization is crucial to mitigate material processing issues. This becomes increasingly important in manufacturing when components must be duplicated on numerous machines that have variable performance.

4.1 Beam terminology

Beam quality refers to the beam diameter and the divergence angle, with a high quality beam having a small focused diameter and a low divergence angle. The beam quality is influenced by the nature of the generated beam, lenses, and machine parameters. For reference, Fig. 71 shows a schematic of a longitudinal beam section commonly referred to as a beam caustic [131]. The beam quality is commonly represented as the beam parameter product (BPP). The BPP is the beam waist (R_0) or radius in millimeters multiplied by the far-field divergence half-angle (θ) in milliradians (mm*mrad) [131]. The smaller the value, the higher the beam quality. The divergence determines the depth-of-field or the distance away from the focused beam waist where the beam maintains its diameter. This is quantified by the distance from the beam waist where the beam doubles its cross-sectional area and is referred to as the Rayleigh length (Z_{RL}).

Comparison of the actual beam to an ideal beam is based on the M^2 value or BPP of the actual beam divided by the BPP of the ideal beam. As the M^2 value approaches one, the closer the generated beam is to a theoretically ideal, diffraction-limited Gaussian beam. This has the greatest ability to be focused and can achieve the highest power density. The K-number is also

Fig. 69 Weld metal porosity at: atmospheric pressure (a), 10^3 Pa (b), 10^1 Pa (c), 10^{-1} Pa (d), 10^{-3} Pa (e) [338]

used to indicate beam quality and is an inverse of the M^2 value. For more information and equations, the reader is referred to References [105, 106, 131, 134]. Fiber lasers can produce a high beam quality even at powers upwards of 50 kW with a BPP less than 8 mm*mrad [131]. This is attributed to the shorter wavelength as compared to CO_2 lasers and the ability for thin fibers to constrict a single mode of wave propagation as compared to Nd:YAG lasers [106].

As discussed in Section 3.1.2, lasers can produce various transverse electromagnetic (TEM) modes or standing wave patterns. TEM modes common for welding include a Gaussian (EB distribution) or a "top-hat" distribution (multiple propagating TEM modes in solid-state lasers). A Gaussian or TEM_{00} mode is shown in Fig. 72a; a multi-mode beam is shown in Fig. 72b; and a TEM_{01*} beam is shown in Fig. 72d. In welding, it is not necessarily desirable to use the highest quality Gaussian or TEM_{00} beam.

With finely focused high intensity beams, weld issues may arise such as: a missed joint caused by narrow welds and insufficient tolerances [106], excessive spatter generation, root porosity [403], and keyhole spiking defects [137]. Multi-mode distributions produce lower quality beams with higher M^2 values ranging from approximately 10–30 [144, 402]. However, multi-mode distributions can mitigate weld related issues caused by high intensity Gaussian profiles. Multi-mode distributions only contain uniform intensity at the focal position and, thus, the beam diameter and the intensity distribution changes at an increasing distance from the focal point [402].

Because physical equipment cannot achieve ideal distributions, there is always discrepancy in the focal point and output intensity distributions. Understanding the output requires measuring multiple intensity distributions and beam diameters throughout the beam axis. This is necessary at various positions above and below the focal point, and this series of measurements can produce a beam caustic as shown in Fig. 73. The intensity disparity for a multi-mode laser beam is also shown in Fig. 73. From this caustic, the beam diameter, intensity distribution, far-field divergence angle, Rayleigh length, BPP, and M^2 values can be computed. It should be noted that these measurements must be taken normal to the beam axis. Some of the historic and current methods for measuring electron and laser beams will be discussed in the Sections 4.2 and 4.3 respectively.

The complex, non-ideal shapes of propagating beams are not conducive to defining an absolute beam diameter. High voltage electron beams are usually representative of a Gaussian-like distribution [250]. This is also the case for single mode and laser beams. Common computations to quantify the beam diameters include full-width-at-half maximum (FWHM), $1/e^2$, D86, and D2M [250, 404]. FWHM is the width of the beam measured at half the peak intensity, and the $1/e^2$ diameter is the distance measured between two points

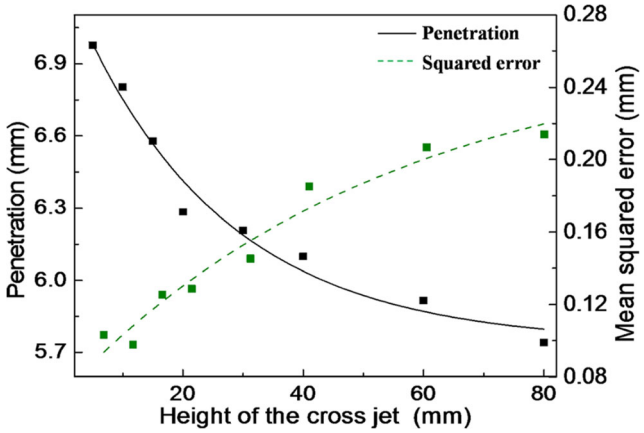

Fig. 70 Penetration versus cross-jet height at 5 kW and a 33 mm/s travel speed [150]

where the intensity reduces by 0.135. D86 is the diameter centered above the centroid where 86% of the total power is contained. D2M is the second-moment beam width and essentially an integral of the intensity weighted according to the square of the distance from the centroid. The D2M diameter is the International Standard Organization (ISO) definition of laser beam diameter [405].

For an ideal Gaussian beam, the $1/e^2$, D86, and D2M methods compute identical results. Beams that take on non-symmetrical shapes may influence the diameter depending on the calculation utilized. Pierce and Burgardt [250] analyzed a low voltage electron beam caustic comprised of a high intensity peak surrounded by an annular ring of electrons for an underfocused welding condition. The analysis shows that this ring surrounding the high intensity peak can lead to variations in D2M calculations as compared to D86 or $1/e^2$. A simulation of this beam profile was recreated by Pierce and Burgardt [250] as shown in Fig. 74. The result of this difference is from the second moment calculation multiplying the intensity by the square of the distance [404, 405]. Therefore, a low percentage of electrons at a large distance from the centroid will significantly increase the computed diameter. This shows the importance of always comparing beam measurements based on consistent definitions when beam profiles result in complex geometries.

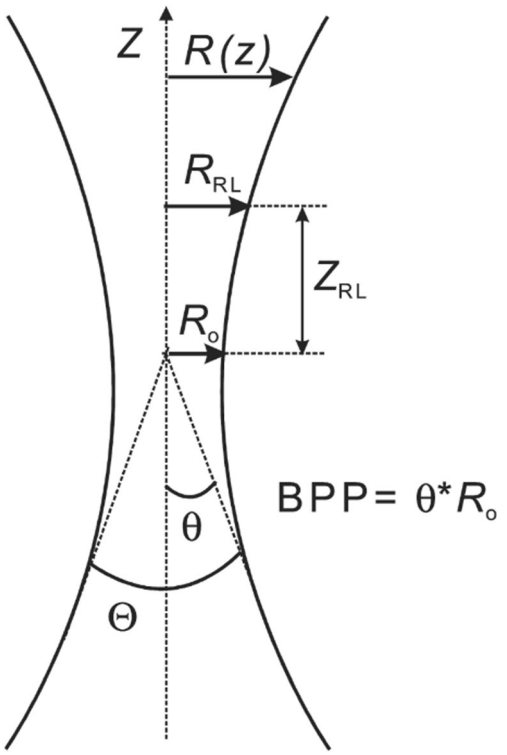

Fig. 71 Representation of a focused beam caustic along the z-axis (longitudinal section) [131]

Welding closest to the focal position provides the greatest process tolerance due to variations in vertical positioning or focal point shifts. As discussed in Section 3.1.2, thermal lensing during laser welding can move the focal position and change the beam diameter, ultimately leading to wide variations in process conditions [328]. An example of varying beam diameter at two different powers and beam-optic transmission times is shown in Fig. 75. Higher laser powers [406], longer times [406], and TEM_{00} distributions with high intensity peaks [105] exacerbate the effects of thermal lensing by changing the refractive index and thermally distorting the lens geometry [106]. This is one example showing why beam diagnostics is imperative to avoid unwanted material processing issues resulting from changes in beam characteristics.

4.2 Electron beam characterization

Electron beam quality control starts with verifying machine settings such as beam current, accelerating voltage, vacuum level, focus current, working distance, and travel speed. The modern EB systems utilize closed-loop feedback controls to maintain consistent parameter outputs. However, settings are not directly comparable between EB machines [407] and can change for a single machine throughout the operational lifetime [407, 408]. Also, the sharp focus beam diameter is determined through operator judgement leading to significant inconsistency [407, 409], and machine maintenance such as filament changes [408] causes filament-to-filament variation in electron emission.

An early method to determine the EB sharp focus position was developed by Arata [410] as shown in Fig. 76a. This test works by the beam passing over thin plates to produce melting and/or cutting at different heights along the beam axis. The physical shift in focal position can be determined, but this procedure does not reveal beam intensity variations. For more in-depth EB diagnostics, methods have been developed to examine the electron beam by reconstructing detected electrical signals relative to beam positions. These methods utilize either a rotating wire traversed through the beam, as shown in Fig. 76b, or some variation of a Faraday cup. Fundamentally,

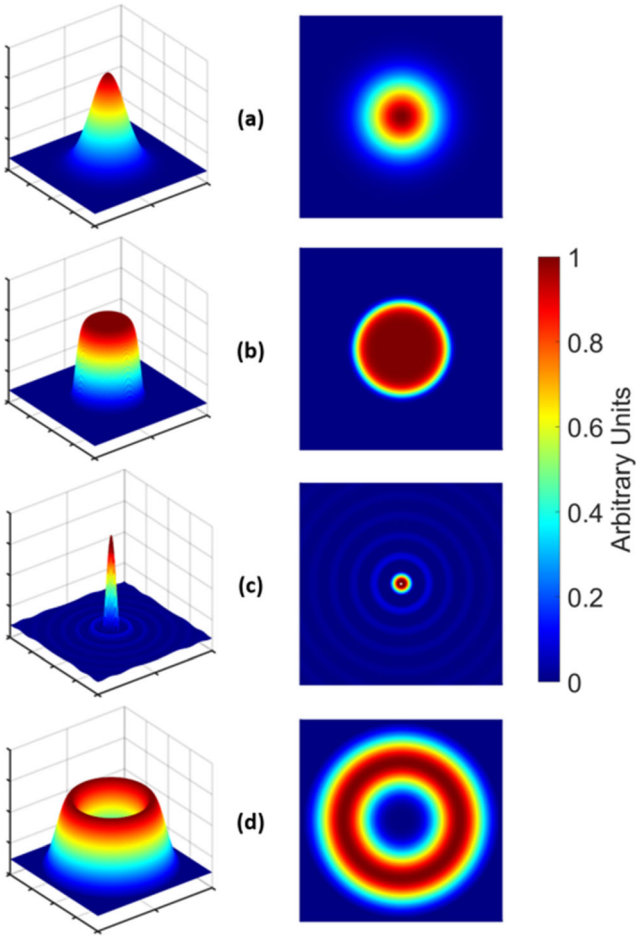

Fig. 72 Laser beam intensity distributions: Gaussian beam (a); multi-mode or "top-hat" (b); Bessel (c); annular, TEM_{01*}, or "donut" (d) [402]

a Faraday cup is a metallic, conductive enclosure that collects electrons through a small orifice. Within the collection cup, a voltage is developed across a resistor that is further processed and analyzed to reproduce the electron intensity. These probes include rotary wire systems [409, 411], single slit systems, multi-slit systems [15, 17, 407, 408], and pinhole systems [250, 404]. Schematics showing the operating principles for the pinhole and slit systems are shown in Fig. 77a and b respectively.

Initial wire-based designs simply utilized a small diameter, stationary wire probe while the beam was moved across the wire [412]. The output current can then be correlated to the fraction of wire within the beam, and it is necessary to maintain a wire size much smaller than the beam diameter [413]. To eliminate influences from beam deflection, rotary wire probes were developed that consist of thin, refractory metals attached to an arm that is rotated at high speed [409, 411, 414, 415]. These designs can provide quantitative information on beam shape, width, and current distribution. In addition, the versatility and simplicity of the rotary probe allows the device to accommodate most EBW systems. Limitations for a wire probe system include the rotation speed, the wire diameter, and the duty cycle with power limited to ≈30kW [409].

Slit-based probes contain high aspect ratio cavities cut into a refractory metal positioned on top of the electron detector. The electron beam is scanned or deflected across slits with widths that are fractions of the beam size as shown in Fig. 78. There are various designs of slit systems from continuous evolution of EB detection development [409, 416]. The enhanced modified Faraday cup (EMFC) [17] is a relatively recent variation of a slit system Faraday cup with slits radially positioned on a tungsten target that allows for recreating the EB distribution [15, 408, 409].

Pinhole based probes are similar to slit based probes except that the geometry of the orifice for sampling the electron beam is a very small hole. The Pro-beam Diagnostic Device (PBD) is an example of a pinhole type system [404]. As with the wire and the slit design, the pinholes must be a fraction of the size of the electron beam diameter. Since these pinholes are very small, debris and melting can be major issues for these systems by preventing or limiting accurate measurements of the electron beam characteristics [409]. Additionally, pinhole systems are limited due to their low signal-to-noise ratio. However, pinhole Faraday cup systems provide comprehensive analysis of the electron beam characteristics for systems with low power limits (≈10kW and below) [409].

Another system, known as the DIABEAM [410, 415], incorporates the rotating wire, slit, and pinhole detection methods to provide a more comprehensive beam diagnostic. The ultimate need for accurately measuring and characterizing the beam with these probing systems is to better understand beam distributions and parameter variations leading to variable weld quality. Using the EMFC, Palmer and Elmer [408] showed the necessity for beam diagnostics to avoid the variations in observed EB parameters at sharp focus. It was reported that the EMFC allowed for maintaining a tolerance of ±2% for FWHM and $1/e^2$ measurements. Caution should be taken when comparing results from different detection methods and diameter measurement definitions; however, Pierce and Burgardt [404] showed similar results for a Pro-Beam pinhole device as compared to the EMFC.

4.3 Laser beam characterization

Laser settings and output powers do not always correspond and can have a significant influence on process performance. This requires knowing and calibrating the difference in set power versus output power for each system. Beam diagnostic tools are required to quantify laser output powers, beam diameters, divergence angles, modes of propagation, and pulse parameters. These analysis tools are lumped into two categories which involve power measurement and beam caustic analysis. The appropriate diagnostics tool must be chosen based on the laser wavelength, continuous versus pulsed

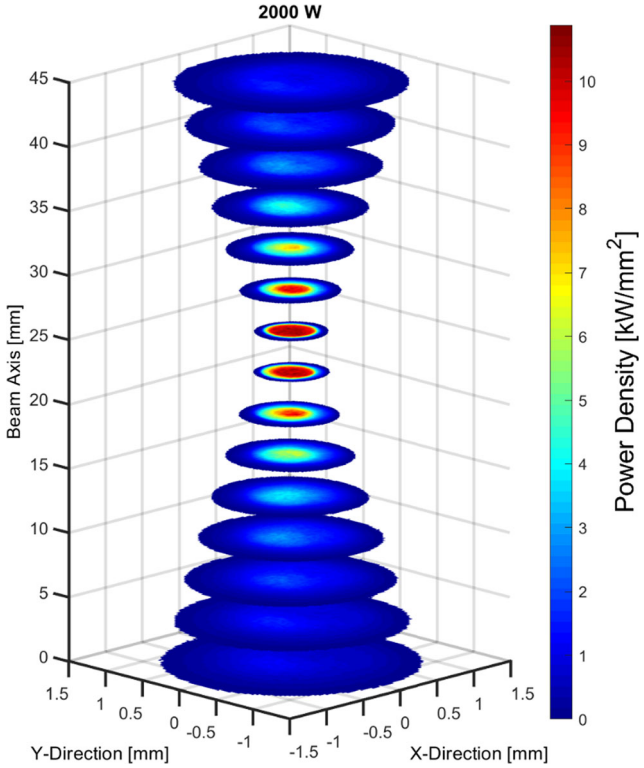

Fig. 73 Multi-mode laser beam caustic at 2000 W of power measured using a commercially available rotating pinhole device [144]

power, overall power, and spot size. There are numerous commercially available laser energy and power sensors available and selecting which sensor to use is largely dependent on the application. This is not intended as an exhaustive overview of these sensors, but provides some information on sensor fundamentals and selection criteria. A list of laser power sensors and characterization systems is provided in Table 8.

4.3.1 Power meters

Thermopiles are composed of many connected thermocouples that produce a voltage proportional to the temperature rise caused by heat absorbed from the incident laser. Because these sensors can take several seconds to stabilize, they are only suitable for average power measurements and not sensitive to individual pulses (Table 8).

Photodiode sensors are semiconductor devices that convert light directly into an electrical signal. Photodiodes are highly sensitive and saturate easily, making these sensors mostly useful for low power lasers (pW to mW) in the visible to near-infrared wavelengths [417, 418]. However, these sensors can measure the variation of the pulse power throughout the temporal profile.

Pyroelectric sensors detect infrared radiation and are highly sensitive, and are widely used for pulsed lasers. They measure the pulse energy of the laser by generating a current when subjected to variations in temperature. The current delivered by each pulse is then proportional to the pulse energy delivered by the laser [418]. These sensors can measure the energy of an individual pulse but cannot differentiate how the pulse power varies throughout the pulse waveform or temporal profile.

The radiation pressure power meter (RPPM) is a recent development that measures the force generated by the laser light and can provide a highly accurate measurement of the laser power [419–422]. A schematic showing the measurement and/or implementation of an RPPM in applications is shown in Fig. 79. The RPPM has been used with CW lasers with powers ranging from 25 W to 50 kW at a 1070 nm wavelength. These sensors are currently being adapted to be mounted within the weld head and have potential for real-time laser power monitoring [421, 423].

4.3.2 Beam profilers

To diagnose the actual laser output distribution as shown in Figs. 72 and 73, it is necessary to direct the laser at a material, such as Kapton® film, or across a sensor. Techniques to sample portions of the beam mainly include cameras for direct laser measurement or rotary devices to direct and detect small fractions of the beam at a given position [106, 428, 429].

Physical beam diameter measurements have and continue to be analyzed by vaporizing materials such as Kapton® film or anodized aluminum. The laser is fired at the material using a single laser pulse, and the diameter of the hole or "charred" region is measured under a microscope. The diameter of the charred region provides an approximation of the laser beam diameter, and the beam caustics are produced by moving the film or material through a range of focal positions. Fuerschbach et al. [424] reported that Kapton® film provides a measurement encompassing approximately 99% of the beam diameter, although the spatial or intensity distribution of the laser cannot be determined. The change in intensity distribution and power showed a divergence (increase) in Kapton® measured diameters as compared to a rotating pinhole device using a D86 beam measurement [424]. Similarly, Wang et al. [425, 430] showed that this technique produces variations in the "charred" region and hole diameter depending on the pulse energies used.

Digital cameras use complementary metal oxide semiconductors (CMOS), charge-coupled device (CCD), or pyroelectric sensors assembled in an array of pixels that convert incident light into an electrical signal [106, 428]. These devices are generally limited to low power or low power densities and a main issue is destroying the detector with the incident beam.

The scanning aperture (pinhole) device diverts a small portion of the laser energy towards a detector at each pass through the beam. A schematic of this device developed by PRIMES GmbH [427] is shown in Fig. 80 [426]. To "map" the beam,

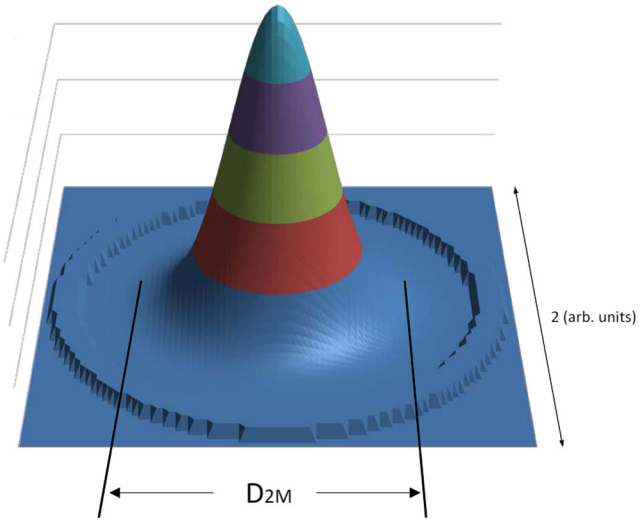

Fig. 74 Simulated low voltage electron beam distribution containing a Gaussian core surrounded by a ring consisting of 10% of the electrons. The computed D2M = 1.2 and 1/e2 = 0.8 (arbitrary units) showing the difference in diameter computations [250]

the detector must be moved relative to the beam axis in the x and y dimensions. The electrical signal produced by the photodiode is saved for each x-y position and used to recreate intensity distributions as shown in Fig. 73. For measuring various wavelengths, different pinhole devices and sensors can be utilized [427].

As with EB, numerous methods have been developed and are continuously improved for detecting laser distributions or mode structures. For more information on detector capabilities the reader is referred to References [106, 428, 429, 427].

4.4 Weld monitoring

The industrial desire for every production weld to meet applicable postweld inspection and/or code requirements has garnered significant investment into developing and implementing real-time weld monitoring and control [431]. Prevention and detection of defect formation is the primary objective of the

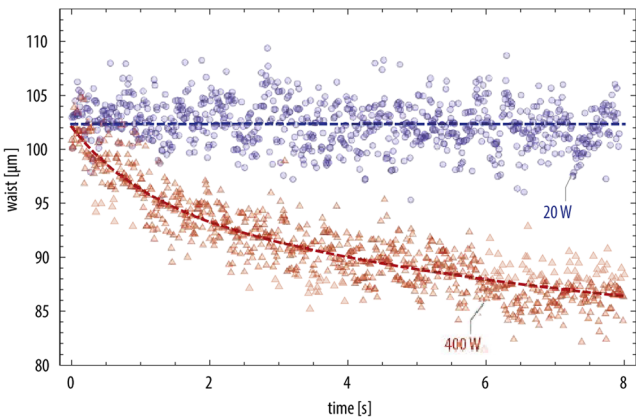

Fig. 75 Focal shift between 20 W and 400 W of beam power for increasing laser-optic transmission time [406]

monitoring technology [432–435]. The addition of weld monitoring systems can lead to further improvement of overall process performance, increased productivity, and cost reduction [433]. This field is advancing quickly and new technologies are being introduced continuously [436–439]. Weld monitoring is performed with optical, thermal, and acoustic sensors, and a single sensor is often insufficient in providing a complete description of weld quality [440]. This facilitates the use of multiple sensors to increase the fidelity of the monitored data. For example, Zhang et al. used a photodiode, high-speed camera, and plume spectral analysis sensor in order to establish a multisensor system in conjunction with neural networks for accurate defect detection [441]. A comprehensive list of commonly used and investigated weld monitoring systems is provided Table 9, and details of these systems are discussed in the following sections.

4.4.1 Inline coherent imaging

Inline coherent imaging (ICI), also known as optical coherence tomography (OCT), is a specialized form of Michelson interferometry. The system operates by emitting a low power, narrow-band laser that is directed toward the workpiece. The reflected, measurement beam allows for detecting changes in surface height, keyhole penetration, and surface irregularities [447, 464].

A more detailed description of ICI operation is shown in Fig. 81. The laser source is directed at a beam splitter that splits the laser into a reference beam and a measurement beam of equal intensity [466–470]. The reference beam is then directed through a fiber to a reference arm with a calibrated distance, and the measurement beam is sent through the laser focusing optics and down onto the workpiece. Light reflected from the surface will then travel back through the weld head where it is recombined with the reference beam. The interference pattern created through the phase shift of waves that travelled different lengths are analyzed via a spectrometer and processed to compute the distance [445, 471].

Webster et al. [446] showed that ICI is capable of detecting weld porosity formation through an increase in noise generated in the graphical output. This is shown in Fig. 82. While Boley et al. [447, 472] proved that the regions with greater noise roughly correspond to the locations of porosity, it is unclear if the plotted points can actually be related to specific pore locations. This indicates that the ICI system is capable of detecting porosity and other subsurface defects but may not be sensitive enough to distinguish pore location.

Boley et al. [447] performed an evaluation of the laser light deflections inside of the keyhole. They found possibilities for laser light to deflect and alter reading capabilities. This allowed for detection of potential keyhole collapse, porosity, and possibly an uneven keyhole surface.

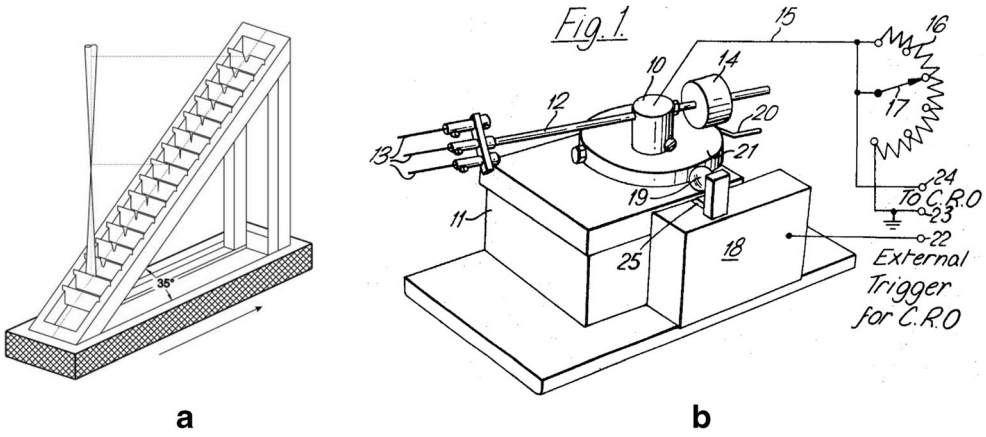

Fig. 76 A physical method developed by Arata to measure the sharp focus beam position (a) [410]. Rotary wire probe system developed by Sanderson and Adams c.1970 (b) [411]

ICI has high temporal and spatial resolution [473], making it ideal for in-situ three-dimensional monitoring of the weld keyhole as well as for closed-loop control. A significant component of this system is the homodyne detection capability [474] as shown in Fig. 83. This aspect allows for real-time control of the weld penetration depth through feedback based off of the detected signal and a preset maximum depth [469]. Through beam scanning, computation of weld head position [468], and analysis of the signal-to-noise ratio [445, 476], ICI has been applied for use in weld seam tracking. This allows for improved uniformity of the weld seam and greater control of seam position. The same process has also been used for improved gap bridging [468] and edge tracking for workpiece positioning [445]. In order to increase component accuracy in additive manufacturing processes, ICI is also being utilized to measure surface roughness [444, 477] and has shown promise for reducing surface roughness through layer-based parameter corrections.

Dorsch et al. [468] has shown that ICI is very effective for monitoring welds in carbon steel and stainless steel alloys. The use of ICI with copper and aluminum alloys is currently limited due to keyhole instability [468, 478, 479], and Schmoeller et al. [478] determined that sensitivity of ICI in aluminum and copper decreases with increasing weld penetration. A comparison of ICI penetration measurements on different alloys is shown in Fig. 84 [468]. The noise generated with different alloys may be due to increased fluctuation in weld pool dynamics. Sudden shifts in the weld morphology are problematic for ICI systems due to an issue known as "fringe wash-out," where the signal-to-noise ratio degrades significantly due to high speed movement of the interfaces [446, 480]. Currently, beam oscillation, beam mode control, and shorter wavelength lasers are being investigated to improve keyhole stability in these highly reflective alloys to enable the use of ICI [378, 480, 481]. Integration of ICI with other types of weld monitoring devices remains in its early stages [438] and further research and development is needed [446, 464, 477, 482].

4.4.2 Photodiode sensors

A photodiode is a form of semiconductor designed to convert light into an electrical signal. Depending on the composition of the photodiode, certain wavelengths of light will be absorbed for conversion. The generated electrical signal is then recorded and compared to reference weld characteristics.

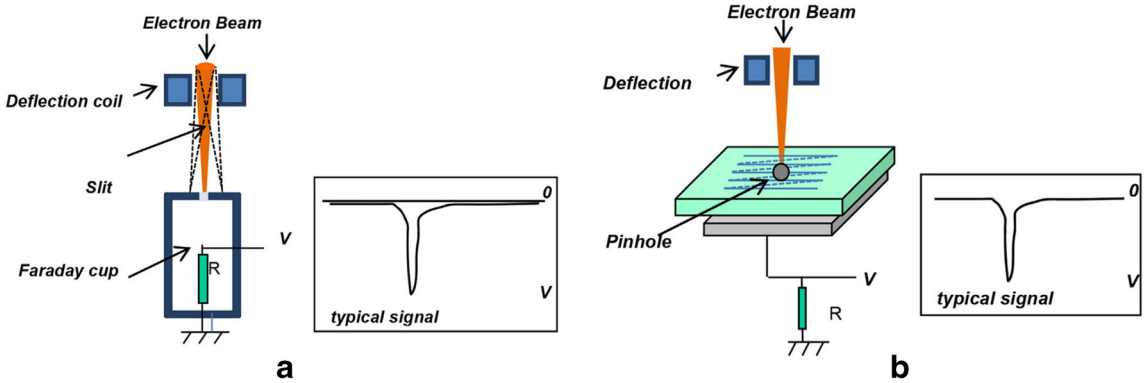

Fig. 77 Electron beam diagnostic device schematics for slit (a) and pinhole (b) type designs [409]

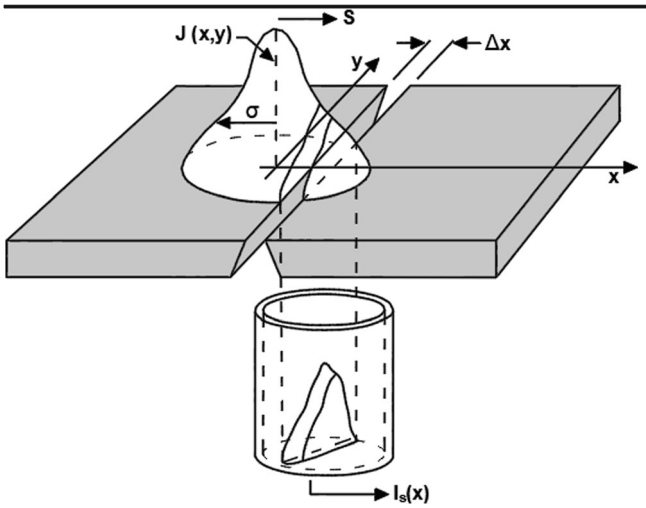

Fig. 78 Illustration of a Gaussian current distribution scanned over a slit of width Δx. Figure recreated from Elmer et al. [15]

In weld monitoring, photodiode sensors are used to detect 1) plume radiation, 2) thermal radiation, and 3) light reflection. Each of these weld related physical phenomena contain characteristic electromagnetic wavelengths [458]. An example of a system using each of these types of photodiodes and the respective detectable wavelength is shown in Fig. 85. There are many different applications for photodiodes in weld monitoring such as in photodiode systems, pyrometers [483], high-speed cameras [484], and plume analysis systems [485].

In photodiode sensors that measure light reflection, laser light directed to the workpiece is reflected toward the optics and collected as backscatter, similar to ICI. According to Kawahito et al. [486], the electrical signal emitted by the photodiode can be used to determine the state of the keyhole such as the start of melting and closure. According to Schmidt et al. [487] light is detected as an optical emission that is recorded as time versus amplitude or frequency as shown in Fig. 86. From the amplitude versus time or frequency outputs, weld defects and weld pool capillary motion can be detected. It is reported that defects cause large shifts in amplitude that last relatively long periods of time; while, capillary movements appear as sharp peaks with a short duration [487]. Defects associated with incorrect beam power, joint contamination, and joint gap have been detected with UV-IR photodiode sensor systems [488].

Thermal radiation photodiode sensors detect differences in the amount of heat based on the amount of infrared light emission [489]. Shifts in the state of the temperature will then be detected by the IR photodiode (generally 750–1700 nm light) and represented as a change in signal intensity. In a system developed by Kawahito et al. [486, 490, 491], infrared photodiode sensors were applied for micro welding applications on aluminum and titanium. Kawahito et al. [486, 490, 491] found a close correlation between weld pool diameter and penetration depth to infrared radiation. However, the photodiode system could only accurately measure the surface condition, and subsurface monitoring was not possible [486]. Porosity, spatter, humping, blowout, underfill, keyhole collapse, and molten ejections are examples of defect types reported being detectable with infrared photodiodes [457, 461, 492].

Low cost is a major benefit to the use of photodiodes for process monitoring [493], and the applicability of photodiodes to any laser welding process including laser AM [494] has permitted exploration into the use of photodiodes for multi-sensor systems [493, 495–498]. However, depending on the application and type of photodiode, sensor sensitivity can be low and a clear signal may not be visible [497, 499, 500]. The

Table 8 Laser beam diagnostic tools

Diagnostics Tool	Sensor	Detectable Waveforms
Power Meter	Thermopile	CW
	Photodiode [417, 418]	Low Power CW
	Pyroelectric [418]	CW, P
	Calorimeter [106]	CW
	Radiation pressure [419–423]	CW
Beam Profiler	Burn paper or Kapton® film [424, 425]	CW, P
	CCD/CMOS camera [426]	CW, P
	Scanning slit/knife edge	CW
	2D scanning pinhole [426, 427]	CW

* CW = continuous wave and P = pulsed

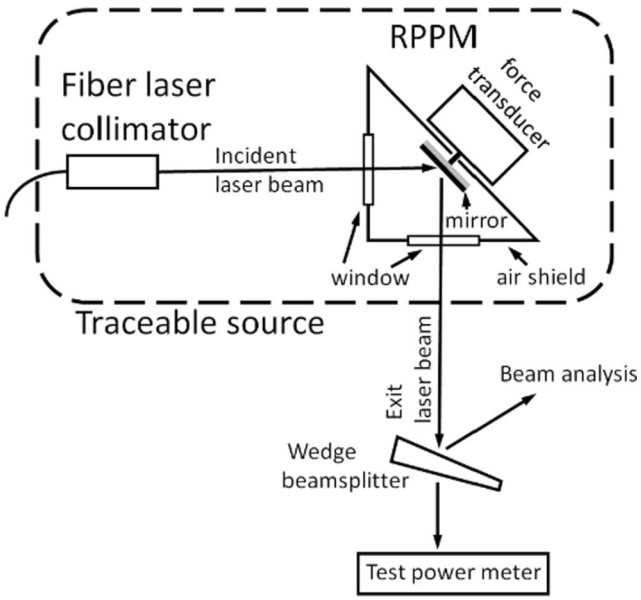

Fig. 79 Schematic of radiation pressure power meter (RPPM) for measurement of laser power in real-time [422]

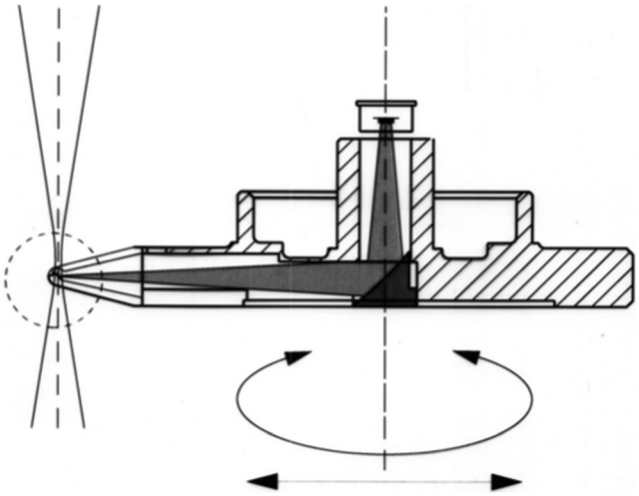

Fig. 80 Schematic cross-section of the rotary pinhole device [426]

correlations drawn by Kawahito et al. [490, 497, 501] to weld pool width and penetration depth are only valid for a fixed laser power, and changes to laser power cause the relationships to fail. According to Norman et al. [502] oxidation on the weld surface can also impact the signal of the photodiode due to changes in emissivity.

Future work involving the use of photodiodes for weld monitoring will require integration with other monitoring systems and neural networks. Such integration will result in high fidelity weld monitoring capable of providing full feedback control and machine learning processes [441, 493, 496].

4.4.3 Pyrometers

A pyrometer detects changes in heat or infrared radiation emitted on its surface through an electrical signal. The intensity of the heat detected by the pyrometer is then correlated to the condition of the weld, and significant changes in the state of the temperature can indicate the presence of a weld defect. There are different types of pyrometers that have been used for welding, including optical pyrometers and infrared photodiode pyrometers. The infrared photodiode pyrometers, in which the photodiode acts as the primary sensor, are the most commonly used [483, 503–507]. Pyrometers can be integrated in many different ways, namely coaxially, weld head mounted, or side mounted [503–507]. When operating a pyrometer coaxially, the sensitivity and accuracy of the system will decrease [505]. This is due to interference caused by heating of the various optical components located within the weld head. In addition, Doubenskaia et al. [508] notes that pyrometers have a low signal-to-noise ratio, requiring multiple measurements for accurate results.

Since pyrometers are sensitive to the emission of heat radiation from the workpiece during welding, weld metal thickness plays a role in the ability of the system to detect changes in temperature. For detectability, thin metals require small temperature changes (<5°C), while thicker metals require larger changes (≈10°C) [505]. The defects that pyrometers are capable of detecting include porosity, lack of fusion, weld disruptions, humping, and improper joint fit-up [504–506, 509]. Forien et al. [504] found that by relating the change in

Table 9 Real-time weld monitoring systems

Monitoring Method	Sampling Frequency (Hz)	Detectable Defects	
Optical Coherence Tomography (OCT) • Interferometer	• 70k – 250k [442, 443]	• Joint Mismatch [443] • Lack of Penetration [443] • Excessive Penetration [443] • Underfill [443] • Blowouts [443]	• Spatter [444] • Weld Seam Deviation [445] • Porosity [446, 447]
High Speed Imaging • Charged Couple Device (CCD) camera • Complementary Metal Oxide Semiconductor (CMOS) camera	• 100 – 2,100k [448, 449] *Note: at max sampling rate resolution is 128x8 pixels [449]	• Lack of Fusion [439] • Weld Disruption [439] • Spatter [450, 451] • Weld Seam Deviation [452], [453] • Surface Porosity [454]	• Blowout [433] • Humping [433] • Underfill [433] • Undercut [433]
Photodiode Sensor • Light sensitive semiconductor	• 0.1 – 1000k [455, 456]	• Joint Mismatch [455] • Excessive Penetration [455] • Spatter [455] • Porosity [456] • Weld Disruption [456]	• Weld Seam Deviation [456] • Lack of Penetration [457] • Humping [458]
Acoustic Emission • Sound transducer • Microphone	• 48k – 4M [438, 459]	• Cracking [438, 460] • Spatter [461] • Humping [461] • Underfill [461]	• Lack of Penetration [462, 463] Porosity [528]

*Note: Defects listed in this table represent those that have been investigated in the literature using the indicated monitoring method. It does not imply that each of these defects will be detectable in all situations or that simultaneous detection is possible.

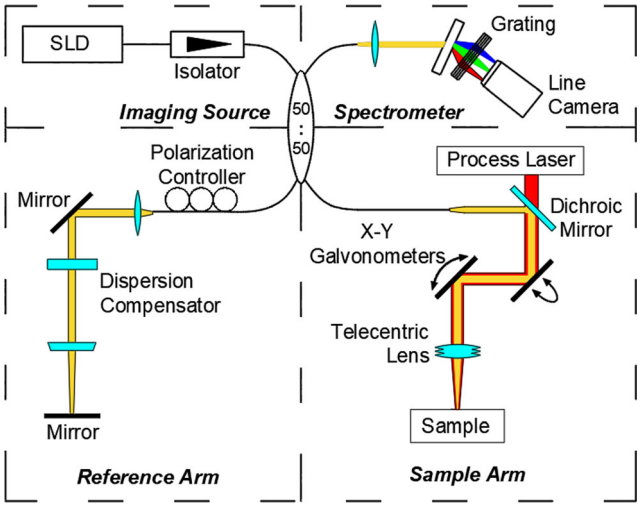

Fig. 81 Schematic of an inline coherent imaging (ICI) or optical computed tomography system recreated from Ji et al. [465]

rate of the signal response from a pyrometer with an increase in normalized enthalpy, a close relationship to pore formation can be developed. From this, a probability curve was developed, and this curve can aid in quantifying the number of weld related defects.

While Xiao et al. [506] determined that a correlation between porosity and subsurface defects could not be drawn, surface geometric defects were readily detectable. An example of this is shown in Fig. 87. A matrix of photodiode based pyrometers have also been used to develop two-dimensional "maps" of the weld pool that will allow for greater defect monitoring [483, 503]. A pyrometer similar to this was developed by Kohler et al. [510] using photodiodes. An infrared photodiode pyrometer has also been used to monitor electron beam welds [483, 511]; however, measurements were captured from outside the vacuum chamber.

4.4.4 High-speed imaging

With high speed image processing capabilities, it is possible to perform in-situ monitoring [453]. Generally, high-speed imaging camera systems use either a charge-coupled device (CCD) or complementary metal oxide semiconductor (CMOS). Although less common, InGaAs cameras can be found for high speed thermal imaging applications [439]. Light is emitted from the weld at various wavelengths, including infrared, visible, and ultraviolet bands [489]. Inclusion of spectral band filters restricts the range of light to isolate specific wavelengths emitted from the weld [451, 487, 512]. For some systems, the use of a separate illumination source, often a laser diode directed toward the camera, is used to illuminate the weld for capturing specific features.

Vapor plume analysis is commonly performed with high speed imaging [513]. Light emitted by the plume is analyzed for variation in intensity or brightness called vapor plume "bursts" or brightness peaks [514]. It was found that the duration of a brightness peak has a strong relationship with keyhole formation. Additionally, the period between peaks can be related to the oscillation of the keyhole, indicating keyhole stability. Brightness peaks seen in CCD camera images may also relate to temperature spikes caused by the topology of the molten surface [514]. The ability to detect or discern changes in the vapor plume is dependent on the material and monitoring systems in use [513]. Measuring spatter generation [515], geometry, and volume is a common application for infrared imaging that often coincides with weld plume monitoring. Monitoring spatter generation and the vapor plume simultaneously aids in understanding plume instability. An example of plume and spatter analysis is shown in Fig. 88.

Infrared cameras mounted coaxially with optics can map heat input into the workpiece [439, 453, 516] as shown in Fig. 89. Thermal distribution of the weld pool can be related to seam position and allow for seam tracking [452, 453]. Therefore, active weld seam tracking with an IR camera can reduce seam mistracking [454, 517]. In these setups, other sensors are "fused" to the camera to provide different analysis or views. Dorsch et al. [439, 517] integrated different bandwidth NIR high speed cameras. By pairing the two cameras together, weld metal emissivity and grey body issues were eliminated.

A drawback for widespread use of high-speed imaging systems is the high cost of equipment [433] and the necessity for extensive filtering to monitor specific events. High-speed cameras are also direct imaging devices and require a clear visual path of the analysis region [518]. Sampling speed and resolution for cameras is another issue, as they are inversely related. Investigations with high-speed cameras involving the use of

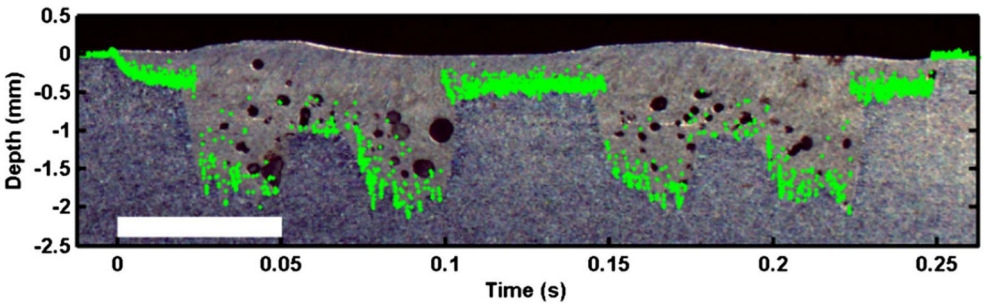

Fig. 82 Graphical overlay of ICI output on the respective longitudinal weld cross-section containing porosity [446]

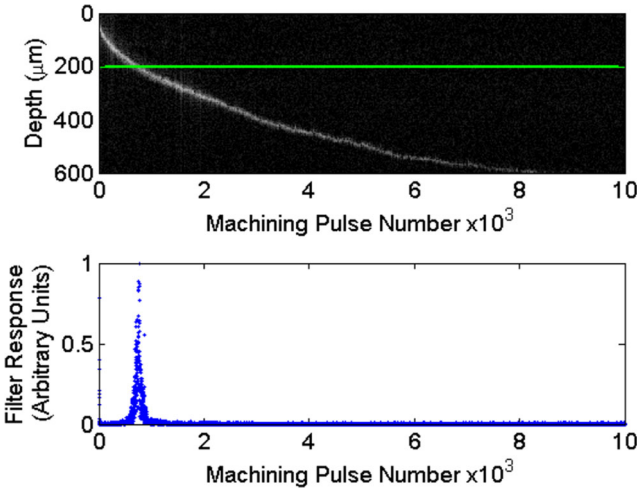

Fig. 83 ICI raw data (top), Homodyne filtered data (bottom) [469, 475]

sensor integration, feedback control, and neural network systems have recently been studied by various investigators including Haubold and Zah [450], Zhang et al. [441, 493], and Liu et al. [496].

4.4.5 Acoustic emission

Acoustic emission (AE) is a form of weld monitoring that involves the use of a direct contact sound transducer (10 kHz–1 MHz) [519–522] or a microphone (20 Hz–20 kHz) [461, 521, 523] to detect acoustic emissions emitted by the welding process [521, 523]. The detected wave is converted to an electronic signal for further processing and analysis. Under defect free steady-state conditions, the amplitude will sustain a specific range [461, 520]. Fluctuations outside the steady-state regime are then indicative of process deviations. An example of a direct contact transducer system is shown in Fig. 90.

AE signals often suffer from extraneous acoustic "noise" that requires signal processing to analyze the actual weld data. One method to reduce the noise is the root mean square (RMS) approach, which averages the signal [521]. Using the RMS of the AE signal, Yi Luo et al. [520] showed a relationship between pulsed laser welding plasma and the acoustic waveform. More complex noise filtering methods involve the use of classification systems and neural networks such as singular value decomposition (SVD) [524] or independent component analysis (ICA) [525]. Shevchik et al. [526] found that defects such as porosity, blowout, keyhole instability, and lack of penetration can be identified using a convolution neural network (CNN), and Farson et al. [523] showed a detectable difference between full and partial penetration welds.

AE monitoring has been performed for a number of applications ranging from laser AM to electron beam welding [460, 462, 527]. Applications such as EBW require direct component contact as the lack of atmosphere prevents propagation of sound waves through space [527]. In the EB application, it was found that the acoustic response signal was a product of either expulsion or violent movement of molten weld metal. Other AE sensors utilize lasers to measure ultrasonic vibrations [436], and microphones called "optical microphones" are employed in analysis of high-frequency AE monitoring [438]. These systems have been paired with other sensor systems for increased defect detection accuracy. [438, 461, 495, 523, 528]

A major limitation of AE monitoring is the propensity for sensor interference from other sources or, as noted above, extraneous "noise." As a consequence, AE is not suited for real-time monitoring in most manufacturing environments [433]. Also, weld parameters cause variations in the sensor sensitivity [519], and transmission of energy by sound is not instantaneous. Therefore, to prevent a lag in system response, it is necessary to consider and minimize the distance between the sensor and the weld. Future advancements for AE monitoring will involve continued development of classification

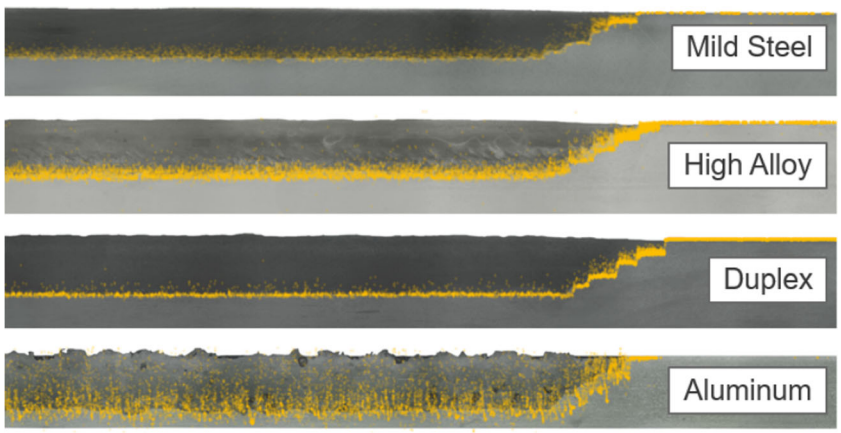

Fig. 84 Comparison of ICI output for various alloys [468]

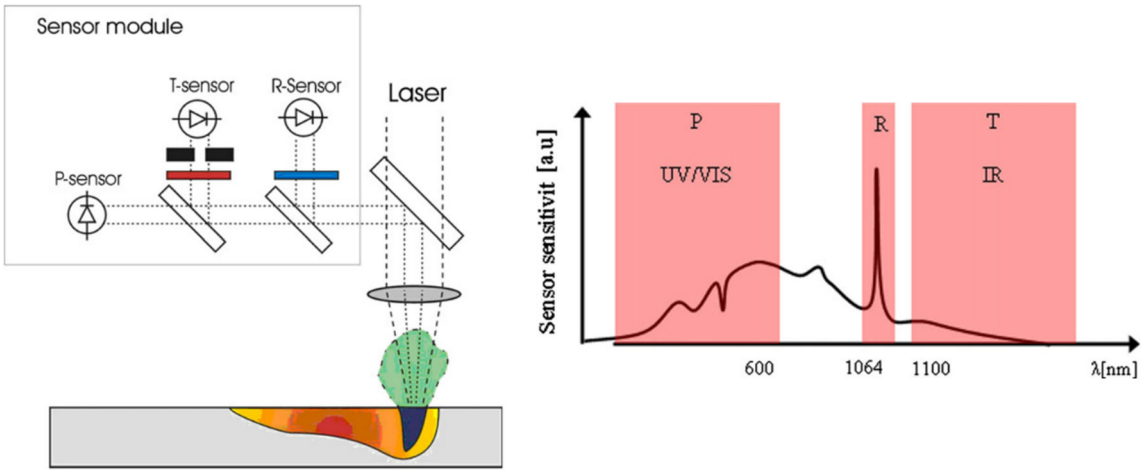

Fig. 85 Photodiode system using a plume radiation sensor (P), thermal radiation sensor (T), and reflected light sensor (R) for detecting different wavebands [457]

and neural network systems as well as an expansion of integrated, multi-component sensor systems [438, 495, 526].

4.4.6 Plume analysis

The vaporization events occurring in HED welding have led to process analysis that considers the evaporating constituents exiting the vapor capillary. At a minimum, it is believed that the metal vaporized in deep penetration welding becomes a weakly-ionized gas within, above, and around the keyhole [513, 514]. This plume aids in relating the transition from the conduction to the keyhole mode, since the conduction mode generates minimal amounts of plume due to limited weld metal vaporization [529]. Therefore, plume fluctuations can be related to keyhole instabilities. There are several methods used for plume monitoring including: plume spectral analysis (optical spectroscopy), vapor charge sensing, high speed imaging, and plume radiation analysis. Some of these methods have been previously discussed as their own monitoring technique. Only plume spectral analysis and vapor charge sensing will be described in this section.

Spectral analysis For plume spectral analysis, the light radiation from the plume is analyzed using a spectrometer to disassociate the wavelength information [485]. By using the Boltzmann method, the electron temperature of the vapor plume can be determined from the spectral response data based on the emission intensity of specific chemical species [530–533]. Changes in the signal intensity can be directly related to changes in the electron temperature. An example illustrating the chemical species over a range of wavelengths is shown in Fig. 91a, and b shows the electron temperature for the plume constituents of Cr, Fe, and Mn. Electron

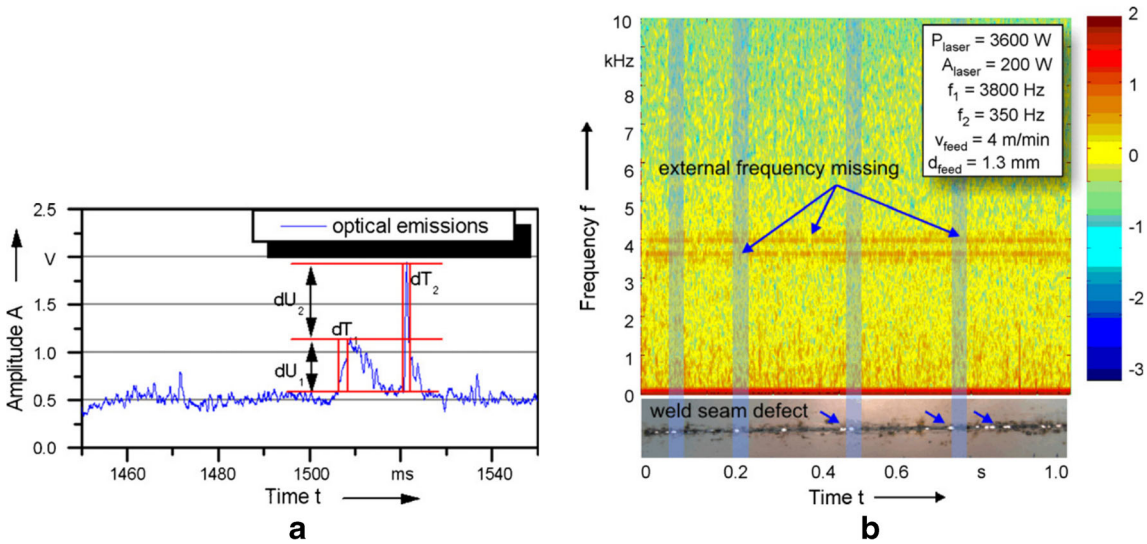

Fig. 86 Amplitude vs. time plot (a) and frequency vs. time plot (b) showing the effect of weld defects on signal intensity from a refletced light photodiode sensor [487]

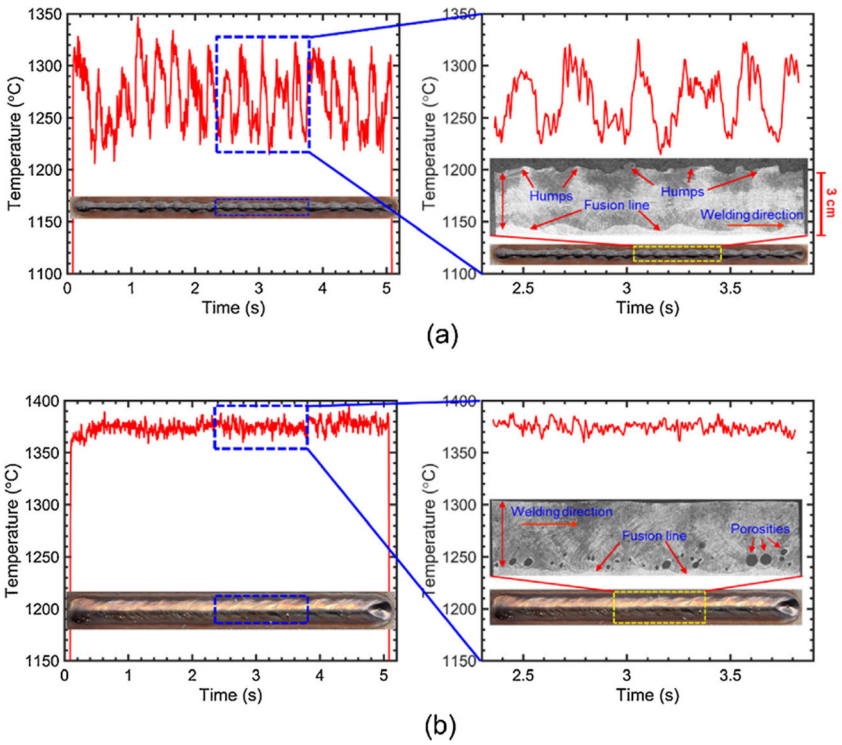

Fig. 87 Response of the pyrometer to surface defects (a) and subsurface defects (b) [506]

temperatures showed a correlation between temperature drops and defect formation, such as spatter generation [535, 536].

Additionally, Ancona et al. [530] determined that the vapor plume is comprised of a core region and outer region that forms depending on the chemical element. Based on this, Ancona et al. [530] found that if the outer plume regions were iron-rich, the plume was less responsive to weld pool fluctuations. It was also reported that changes to power and

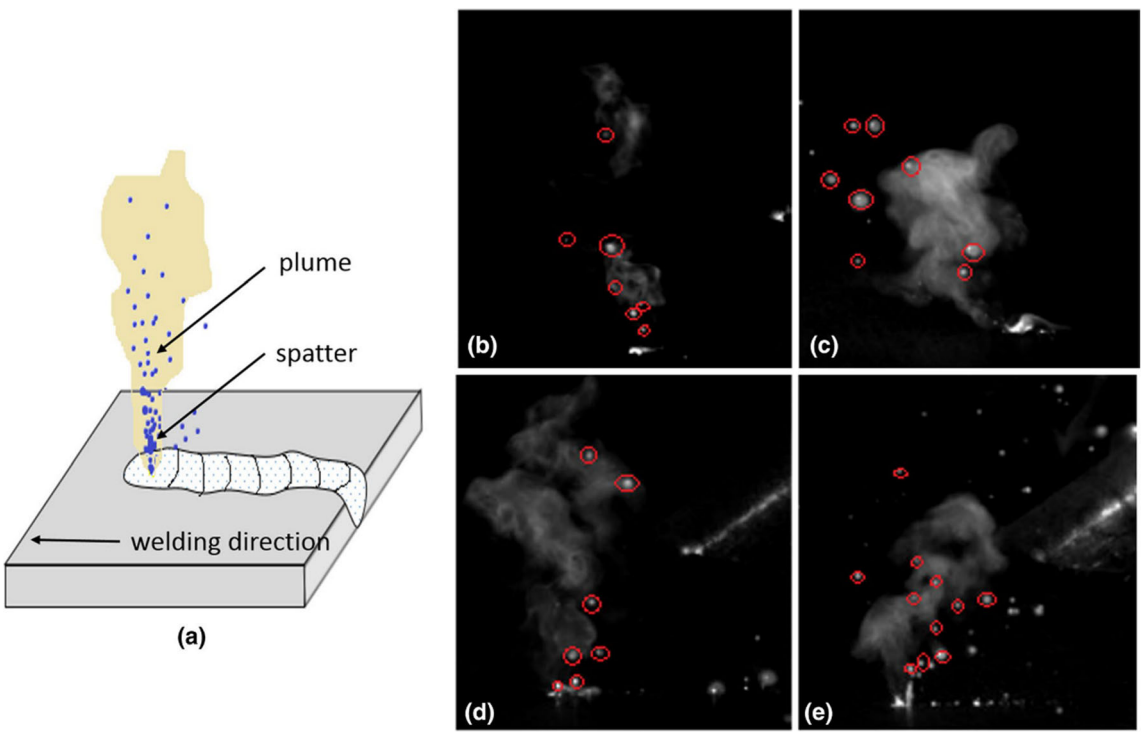

Fig. 88 Infrared images of the weld vapor plume and spatter at different welding speeds: 3 mm/min (b), 5 mm/min (c), 7 mm/min (d), and 9 mm/min (e) [451]

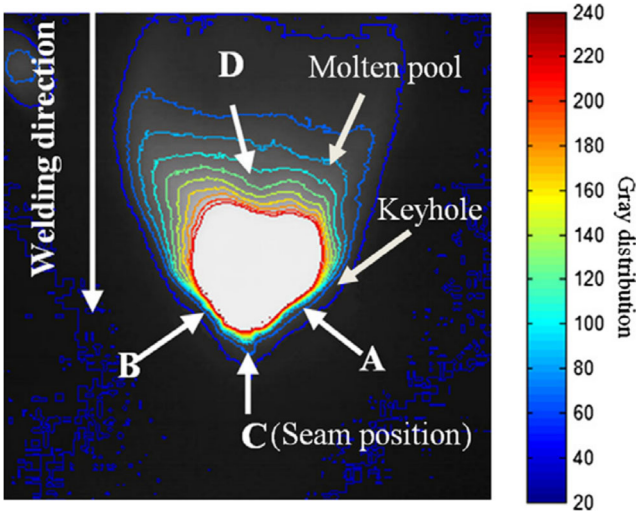

Fig. 89 Infrared map of the molten pool captured from above the weld seam with a high speed CMOS camera sensitive to near-IR light [453]

shielding gas flow rates, lack of penetration, porosity, crater formation, and uneven welding surfaces are detectable.

Using this approach, the penetration depth and weld seam geometry can only be inferred through the correlation of the electron temperature and the laser power. Any penetration measurements recorded through plume analysis only accounts for the chemical change above the weld as opposed to the physical characteristics (i.e., weld penetration, seam width, etc.). This was corroborated by Kong et al. [535], where they concluded that the relationship of weld penetration to the electron temperature is negligible. However, Sibillano et al. [532], found that changes in the weld penetration proportionally relate to changes in electron temperature.

Vapor charge Another form of weld plume monitoring involves detecting a charge generated by the vapor phase and relating this detected charge to vapor temperature. A copper probe inserted between the weld head and the workpiece creates the circuit in contact with the plume, and the charge produced by the plume generates the voltage for analysis [537, 538]. A schematic of this configuration is shown in Fig. 92. The mean voltage from the vapor charge sensor was found to be a direct measure of the weld penetration depth. Large voltage drops from the sensor indicate that the keyhole has collapsed, a failure often associated with porosity and other major weld defects [540]. An unstable signal delivered by the sensor can be associated with fluctuations in the weld plume. This can indicate excessive heating of the workpiece and melt-through defects. Other detectable irregularities include humping, cratering, beam position shifts, and mistracking [539, 540]. Mistracking is measured by increases and decreases in the voltage differential, as shown in Fig. 93. Vapor charge sensors have also been used in electron beam welding by detecting the weak electrical signal produced by the plume. The vapor produced by the electron beam was used to monitor the weld quality and keyhole shape [541].

For effectiveness, plume analysis generally requires high volumes of ionized vapor produced during the welding process. Kawahito et al. [351] and Sibillano et al. [532] found that increasing the power density of CW fiber lasers will allow for weak ionization of the weld vapor plume and greater plume stability. However, plume absorption of the laser beam can reduce the power coupling to the workpiece and cause periodic plume formation [513]. Research into the use of plume spectrometry and charge sensing for feedback control is ongoing [540, 542, 543]. At the time of this writing, there is no commercially available plume spectrometer or charge sensor that can be effectively used for monitoring purposes.

4.5 Feedback control

Most of the weld monitoring technologies mentioned here have been incorporated into feedback control systems in some capacity. ICI has been integrated with feedback systems to provide penetration depth control in partial penetration welds [474]. This system can adjust the laser parameters in real-time to ensure the weld penetration does not exceed a predetermined value. ICI has been successful in real-time

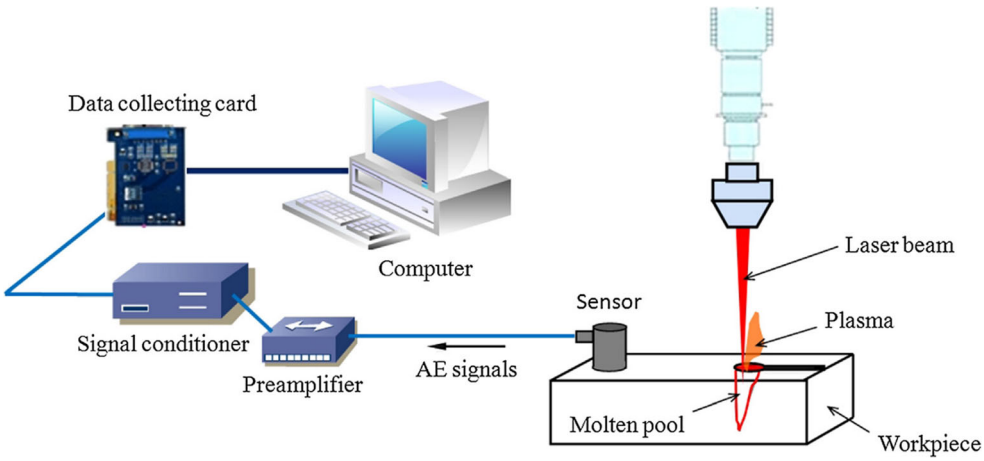

Fig. 90 Schematic of a surface contact acoustic emission system [520]

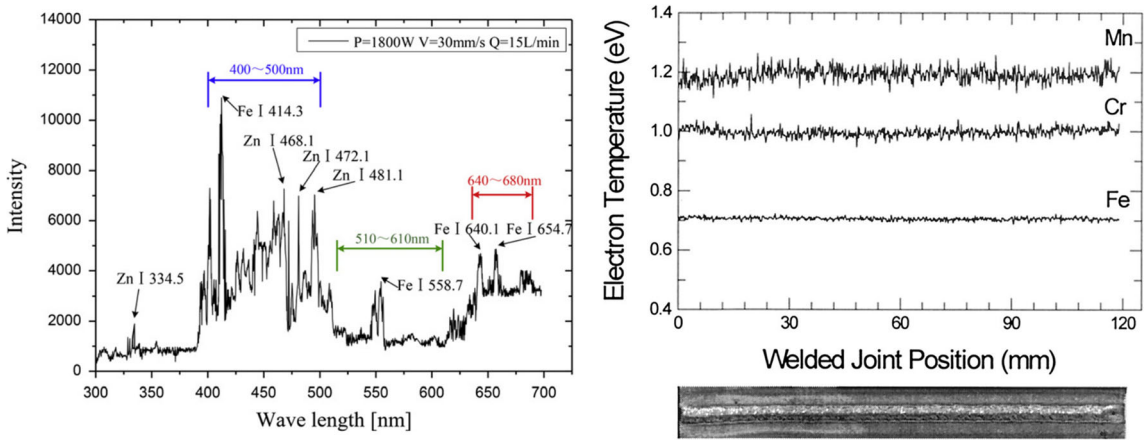

Fig. 91 Plume spectral intensity of chemical species (left) [534]. Electron temperature as a function of position using a Boltzmann method conversion (right) [530]

weld seam and weld profile tracking by preventing deviations from process requirements [445].

A photodiode feedback control system developed by Kawahito et al. [486] combines the use of infrared radiation and the light reflected off of the workpiece to reduce the quantity of spatter and porosity created during the welding process [490, 491]. Controlling the laser power ramp rate was established to increase the amount of time for entrapped gas to escape the weld in order to reduce porosity and underfill [490, 500]. Continuous adjustment of the laser power by the control system improved the weld bead surface geometry. In a P-LBW system, feedback control also permitted the active adjustment of the pulse shape [486, 490]. Kawahito et al. [486] was also able to repair welds containing lack of fusion defects through the use of a closed-loop feedback control.

Examples of systems to analyze weld data in real-time are found for the following weld monitoring devices: acoustic emission [462, 495, 519, 525, 526, 528, 544], photodiode [441, 493], plume spectroscopy [496], and vapor charge [540, 543]. While most of these publications contain extensive data analysis, there are limited examples of the use of neural networks with an adaptive control system in an applied setting [495]. As feedback control and machine learning are the goal of real-time weld monitoring, additional research into the use of weld monitoring devices with neural networks and classification systems is necessary.

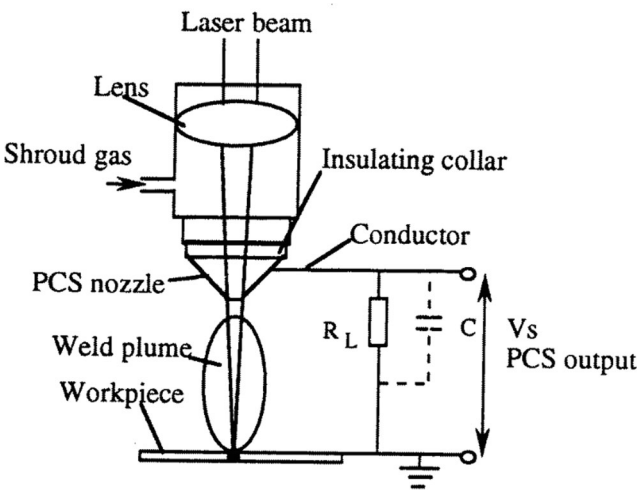

Fig. 92 Schematic of a weld head mounted vapor charge probe [539]

5 Summary and outlook

The fundamental nature and application of laser beam and electron beam welding processes have been reviewed here. Although both welding technologies are considered reasonably mature, continued research and development will allow expanded application and new opportunities. The extensive use of high-energy density beams for additive manufacturing is an example of such an opportunity. The beam processes are unique in that they are extremely flexible, allowing for both deep penetration "keyhole" welding and shallow to intermediate penetration in a conduction heat transfer mode. This flexibility accommodates the manufacturing of large-scale ship panels, and small-scale medical devices often with weld

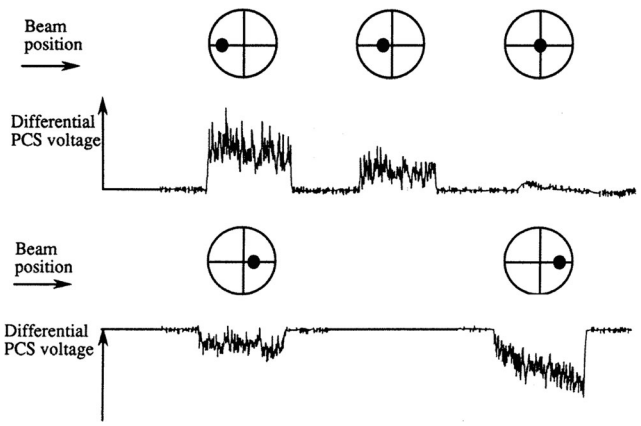

Fig. 93 Example of weld mistracking using a vapor charge sensor [539]

qualities that are unmatched by competing processes. These processes can also provide advantages over standard arc welding when reduced overall heat input is required to control metallurgical properties, to enable dissimilar welding, or to minimize residual stress and distortion.

Much of the current research involving these processes concerns weld monitoring and control. The unique characteristics of the processes that lead to metal vaporization, keyhole formation, and vapor "plumes" provide challenges with respect to in-situ control. Advances in sensor technology and signal processing software over the past 20 years have allowed major advances in the development of more effective control algorithms, but many challenges still exist today. An example of a current challenge in additive manufacturing is the limited characterization of the beam within the work envelope, which results in an uncontrolled process and inconsistent builds across the build area or between different machines. Current research efforts are focused on understanding the change in beam properties across the build area or different machines and incorporating in-situ monitoring to provide the level of process control required for future advancements.

This review is intended to provide the reader with the history, background, and current state-of-the art and establish a basis for future advancements in the use of high-energy density beam technology in welding and advanced manufacturing. The extensive list of references will also allow the reader to pursue the topics discussed in much greater detail with respect to specific materials and applications.

List of terms AE, acoustic emission; AM, additive manufacturing; BPP, beam parameter product; CAD, computer-aided design; CCD, charge-coupled device; CMOS, complementary metal oxide semiconductors; CNC, computer numerical control; CW, continuous wave; DED, direct energy deposition; DSS, duplex stainless steel; EBW, electron beam welding; EMFC, enhanced modified Faraday cup; FWHM, full width at half maximum (beam size measurement); FZ, fusion zone; HAZ, heat-affected zone; HED, high-energy density; HLAW, hybrid laser-arc welding; ICI, inline coherent imaging; LASER, light amplification by stimulated emission of radiation; LBW, laser beam welding; LED, light-emitting diode; LENS™, Laser-engineered net shaping; LPBF, laser powder bed fusion; MASER, microwave amplification by stimulated emission of radiation; NDE, nondestructive evaluation; Nd:YAG, neodymium doped yttrium aluminum garnet; OCT, optical coherence tomography; PBF, powder bed fusion; P-LBW, pulsed laser beam welding; RPPM, radiation pressure power meter; TEM, transverse electromagnetic modes; YAG, yttrium aluminum garnet

Acknowledgements This review was supported through the National Science Foundation (NSF) sponsored Industry/University Cooperative Research Center (I/UCRC): Manufacturing and Materials Joining Innovation Center (MA^2JIC). The authors would like to thank Los Alamos National Laboratory (LANL) for providing financial support and, in particular, Dr. Matt Johnson and Dr. David Tung who have served as mentors for this project. Also, the authors would like to thank Dr. Pat Hochanadel and Dr. Tung from LANL, and Mr. Doug Kautz from Leidos Inc. for reviewing the manuscript and providing valuable input.

References

1. Steigerwald KH et al (2007) An International History of Electron Beam Welding. pro beam
2. McCarthy PT, Reifenberger RG, Fisher TS (2014) Thermionic and photo-excited electron emission for energy-conversion processes. Front. Energy Res. 2(12):1–15
3. Falconer I (1997) J. J. Thomson and the discovery of the electron. Phys. Educ. 32:226–231
4. McMullan D (1995) Scanning Electron Microscopy. Scanning 17: 175–185
5. Crookes W (1878) The Bakerian Lecture - On the Illumination of Lines of Molecular Pressure, and the Trajectory of Molecules
6. von Pirani M (1907) Production of Homogenous Bodies from Tantalum or Other Metals. US 848,600
7. Busch H (1926) Berechnung der Bahn von Kathodenstrahlen im axialsymmetrischen elektromagnetischen Felde. Ann. Phys. 81:974
8. Ruska E, Knoll M (1931) Die magnetische Sammelspule fur schnelle Electronenstrahlen. Z. f. Techn. Phys. 12:389
9. Marko M, Rose H (2010) The contributions of Otto Scherzer (1909-1982) to the development of the electron microscope. Microsc. Microanal. 16(4):366–374
10. Bruche, Scherzer (1934) Geometrische Electronoptik. Julius Springer, Berlin
11. Breton BC. The early history and development of the scanning electron microscope. [Online]. Available: http://www-g.eng.cam.ac.uk/125/achievements/oatley/history.html. Accessed 07 Sept 2020
12. Stohr JA (1956) Procédé de soudure des métaux par bombardement électronique. FR 1,141,535 A
13. Lawrence G (1974) Triode electron gun for electron beam machines
14. Vaughan WH (1978) Direct Measurement of the electron beam of a scanning electron microscope
15. Elmer J, Teruya A, O'Brien D (1993) Tomographic imaging of noncircular and irregular electron beam current density distributions. Weld J 72(11):493s–505s
16. Teruya AT, Elmer JW (1996) Tomographic determination of the power distribution in electron beams. US 5,583,427
17. Elmer JW, Teruya AT (2001) Enhanced modified Faraday cup for determination of power density distribution of electron beams. US 6,300,755 B1
18. Stern DP, Peredo M. History of the electron. [Online]. Available: https://pwg.gsfc.nasa.gov/Education/whelect.html. Accessed 17 Aug 2020
19. Powers DE (2011) Electron Beam Welding in the United States. PTR-Precision Technologies, Enfield
20. Einstein A (1996) Emission and Absorption of Radiation in Quantum Theory. In: Kox AJ, Klein MJ, Schulmann R (eds) The Collected Papers of Alber Einstein The Berlin Years: Writings, 1914-1917, pp 212–216
21. Murphy J (2016) From masers to lasers in space — and at the cinema! Photonics media. [Online]. Available: https://www.photonics.com/Articles/From_Masers_to_Lasers_in_Space_and_at_the/a61182. Accessed 19 July 2020
22. Hecht J (2010) A short history of laser development. Opt. Eng. 49: 99–122
23. Gould G (1968) Apparatus for generating radiation of frequencies higher than those of light. US 3,388,314
24. Schawlow AL, Townes CH (1960) Masers and maser communications system. US 2,929,922
25. Schawlow AL, Townes CH (1958) Infrared and Optical Masers. Phys. Rev. 112(6):1940–1949
26. Gould G (1977) Optically pumped laser amplifiers. US 4,053,845

27. Maiman TH (1967) Ruby laser system. US 3,353,115
28. Hecht J (2005) The Race to Make the Laser. Opt Photon. News. no. July/August, pp. 24–29
29. Einstein A (1996) On the quantum theory of radiation. In: Kox AJ, Klein MJ, Schulmann R (eds) The collected papers of Alber Einstein the Berlin years: writings, 1914–1917, pp 220–233
30. Ladenburg R (1927) Untersuchungen uber die anomale Dispersion angeregter Gase
31. Weber J (1953) Amplification of Microwave Radiation by Substances not in Thermal Equilibrium
32. Gordon JP, Zeiger HJ, Townes CH (1954) Molecular microwave oscillator and new hyperfine structure in the microwave spectrum of NH3. Phys. Rev. 95(1):282–284
33. Javan A, Bennett WR, Herriott DR (1961) Population inversion and continuous optical maser oscillation in a gas discharge containing a He-Ne mixture. Phys. Rev. Lett. 6(3):106–110
34. Snitzer E (1961) Optical maser action of Nd+3 in a barium crown glass. Phys. Rev. Lett. 7(12):444–446
35. Hall RN, Fenner GE, Kingsley JD, Soltys TJ, Carlson RO (1962) Coherent Light Emission from GaAs Junctions. Phys. Rev. Lett. 9(9):366–369
36. Nathan MI, Dumke WP, Burns G, Dill FH, Lasher G (1962) Stimulated emission of radiation from GaAs p-n junctions. Appl. Phys. Lett. 1(3):62–64
37. Quist TM et al (1962) Semiconductor maser of GaAs. Appl. Phys. Lett. 1(4):91–92
38. Newman R (1963) Excitation of the Nd 3+ Fluorescence in CaWO4 by Recombination Radiation in GaAs. J. Appl. Phys. 34(2):437
39. Patel CKN (1964) Continuous-Wave Laser Action on Vibrational-Rotational Transitions of CO2. Phys. Rev. 136(5A): A1187–A1194
40. Geusic JE, Marcos HM, Van Uitert LG (1964) Laser oscillations in nd-doped yttrium aluminum, yttrium gallium and gadolinium garnets. Appl. Phys. Lett. 4(10):182–184
41. Koester CJ, Snitzer E (1964) Amplification in a Fiber Laser. Appl. Opt. 3(10):1182–1186
42. Mears RJ, Reekie L, Poole SB, Payne DN (1985) Neodymium-doped silica single-mode fibre lasers. Electrons Lett. 21(17):738–740
43. Giesen A, Hügel H, Voss A, Wittig K, Brauch U, Opower H (1994) Scalable concept for diode-pumped high-power solid-state lasers. Appl. Phys. B Lasers Opt. 58(5):365–372
44. Giesen A, Speiser J (2011) Thin-Disc Lasers. In: Injeyan H, Goodno DG (eds) High-Power Laser Handbook. McGraw-Hill Companies, Inc., pp 225–266
45. Gapontsev PV, Samartsev I (1999) Coupling arrangement between a multi-mode light source and an optical fiber through an intermediate optical fiber length. US 5,999,673
46. Gapontsev V (2004) Ultra High Power Ytterbium Fiber Lasers. In: 1st Pacific International Conference on Applications of Lasers and Optics
47. Patel CKN (1973) Carbon dioxide laser employing multiple gases including helium. US 3,745,482
48. Patel CKN (1965) CW High Power N2–CO2 Laser. Appl. Phys. Lett. 7(1):15–17
49. Patel CKN, Tien PK, McFee JH (1965) CW High-Power CO2–N2–He Laser. Appl. Phys. Lett 7(11):290
50. Tsukamoto S (2013) Developments in CO2 laser welding. In: Katayama S (ed) Handbook of Laser Technologies. Elsevier, pp 17–46
51. Gottwald T et al (2012) Recent disk laser development at Trumpf. In: Proc. SPIE 8547 - high-power lasers 2012: technology and systems, 85470C
52. Schad S-S et al (2016) Recent development of disk lasers at TRUMPF. In: Proc. 9726 - Solid State Lasers XXV: Technol. Devices, 972615
53. Keyes RJ, Quist TM (1964) CaF2:U3+ with GaAs Diode Lasers. Appl. Phys. Lett. 4(3):50–52
54. Allen RB, Scalise SJ (1969) Continuous operation of a YAlG: Nd laser by injection luminescent pumping. Appl. Phys. Lett. 14(6): 188–190
55. Welch DF (2000) A Brief History of High-Power Semiconductor Lasers. IEEE J. Sel. Top. Quantum Electron. 6(6):1470–1477
56. McDougall SD et al (2020) Advances in diode laser bar power and reliability for multi-kW disk laser pump sources. In: Proc. SPIE 11262 - high-power diode laser technol. XVIII, 1126206
57. Polijanczuk AV, Whitehead DG (1991) Semiconductor Lasers for Microsoldering. In: IEEE Colloquium on Advances in Interconnection Technology
58. Rossin V, Skidmore J, Zucker E (2011) Semiconductor Laser Diodes. In: Injeyan H, Goodno DG (eds) High-power laser handbook. Inc, McGraw-Hill Companies, pp 101–131
59. Treusch H, Pandey R (2011) High-power diode laser arrays. In: Injeyan H, Goodno DG (eds) High-power laser handbook. McGraw-Hill Companies, Inc., pp 133–159
60. Kleine K, Balu P (2017) High-power diode laser sources for materials processing. Proc. 2017 High Power Diode Lasers Syst. Conf:3–4
61. Clarkson WA, Hanna DC (1996) Two-mirror beam-shaping technique for high-power diode bars. Opt. Lett. 21(6):375–377
62. Snitzer E (1961) Proposed Fiber Cavities for Optical Masers. J. Appl. Phys. 32(1):36–39
63. Keck D, Schlutz P (1973) Method of producing optical waveguide fibers. US 3,711,262
64. Wyatt R (1989) High Power Broadly Tunable Erbium-Doped Silica Fibre Laser. Electrons Lett. 25(22):1498–1499
65. Snitzer E, Po H, Hakimi F, Tumminelli R, McCollum BC (1988) Double clad, offset core Nd fiber laser. In: Optical fiber communication conference, PD5:1–3
66. Po H et al (1989) Double clad high brightness Nd fiber laser pumped by GaAlAs phaser array. In: Optical fiber communication conference, PD7:1–4
67. IPG photonics successfully tests world's first 10 kilowatt single-mode production laser. [Online]. Available: https://www.laserfocusworld.com/home/article/16559922/ipg-photonics-successfully-tests-worlds-first-10-kilowatt-singlemode-production-laser. Accessed 23 June 2020
68. Kawahito Y, Wang H, Katayama S, Sumimori D (2018) Ultra high power (100 kW) fiber laser welding of steel. Opt. Lett. 43(19)
69. Ribic B, Palmer TA, DebRoy T (2009) Problems and issues in laser-arc hybrid welding. Int. Mater. Rev. 54(4):223–244
70. Pinto H, Pyzalla A, Hackl H, Bruckner J (2006) A comparative study of microstructure and residual stresses of CMT-, MIG - And laser-hybrid welds. Mater. Sci. Forum 524–525(614):625–632
71. Xu G, Pan H, Liu P, Li P, Hu Q, Du B (2018) Finite element analysis of residual stress in hybrid laser-arc welding for butt joint of 12 mm-thick steel plate. Weld. World 62(2):289–300
72. Gao M, Zeng X, Yan J, Hu Q (2008) Microstructure characteristics of laser-MIG hybrid welded mild steel. Appl Surf Sci. 254(18):5715–5721
73. Liu L, Hao X, Song G (2006) A new laser-arc hybrid welding technique based on energy conservation. Mater Trans. 47(6): 1611–1614
74. Gibson I, Rosen DW, Stucker B (2019) Additive Manufacturing Technologies. Springer
75. Gandy DW (2018) Qualification of Laser Powder Bed Fusion-AM for Nuclear Pressure Retaining Applications. In: Advanced Manufacturing for Nuclear: Applications, Techniques, Needs, and Challenges and AMM Annual Program Review
76. Milewski JO (2017) Additive Manufacturing of Metals. Springer

77. Bourell DL, Marcus HL, Barlow JW, Beaman JJ, Deckard CR (1990) Multiple material systems for selective beam sintering. US 4,944,817
78. Knapp CM (2018) Directed energy deposition characterization and modeling. PhD Thesis. The University of Texas at Austin
79. Sing SL, An J, Yeong WY, Wiria FE (2016) Laser and electron-beam powder-bed additive manufacturing of metallic implants: A review on processes, materials and designs. J. Orthop. Res. 34(3): 369–385
80. Bandyopadhyay A, Bose S (2016) Additive manufacturing, 2nd edn. CRC Press
81. Schade CT, Murphy TF, Walton C (2014) Development of atomized powders for additive manufacturing. In: Adv. Powder Metall. Part. Mater. - 2014, Proc. 2014 World Congr. Powder Metall. Part. Mater. PM 2014, pp 215–225
82. Megahed M, Mindt HW, N'Dri N, Duan H, Desmaison O (2016) Metal additive-manufacturing process and residual stress modeling. Integr. Mater. Manuf. Innov. 5(1):61–93
83. Yang L et al (2017) Electron beam technology. In: Additive manufacturing of metals: the technology, materials, design and production, pp 63–79
84. DebRoy T et al (2018) Additive manufacturing of metallic components – Process, structure and properties. Prog. Mater. Sci. 92:112–224
85. Dass A, Moridi A (2019) State of the Art in Directed Energy Deposition: From Additive Manufacturing to Materials Design. Coatings 9(7):1–26
86. Baker R (1925) Method of making decorative articles. US 1,533, 300
87. Ujiie A (1970) Method of constructing substantially circular cross-section vessel by welding. US 3,665,143
88. Stecker S (2010) Electron Beam Layer Manufacturing. US 8,546, 717 B2
89. American Welding Society C7 Committee (2013) AWS C7.1M/C7.1:2013 recommended practices for electron beam welding and allied processes. American Welding Society
90. Atwood C et al (1998) Laser engineered net shaping (LENS^{TM}): a tool for direct fabrication of metal parts. Sandia National Laboratories
91. Hofmeister W, Griffith M, Ensz M, Smugeresky J (2001) Solidification in Direct Metal Deposition by LENS Processing. Jom 53(9):30–34
92. Taheri H, Shoaib MRBM, Koester LW, Bigelow TA, Collins PC, Bond LJ (2017) Powder-based additive manufacturing - a review of types of defects, generation mechanisms, detection, property evaluation and metrology. Int. J. Addit. Subtractive Mater. Manuf. 1(2):172–209
93. Cordova L, Campos M, Tinga T (2019) Revealing the Effects of Powder Reuse for Selective Laser Melting by Powder Characterization. JOM 71(3):1062–1072
94. Kemerling BL (2018) Development of a weldability testing strategy for laser powder-bed fusion applications. PhD Thesis. The Ohio State University
95. Luft A, Pflueger S (2011) Body-in-white diode laser brazing. [Online]. Available: https://www.industrial-lasers.com/welding/article/16485690/bodyinwhite-diode-laser-brazing. Accessed 05 July 2020
96. Mattulat T, Kügler H, Vollertsen F (2020) Investigations on the occurrence of different wetting regimes in laser brazing of zinc-coated steel sheets. Weld. World 64:449–456
97. Shapiro LA, Shapiro AE (2007) Brazing and Soldering Today. Weld. J. 86(3):74–78
98. Saida K, Song W, Nishimoto K (2006) Laser brazing of alloy 600 with precious filler metals. Sci. Technol. Weld. Join. 11(6):694–700
99. Reimann W, Dobler M, Goede M, Schmidt M, Dilger K (2017) Three-beam laser brazing of zinc-coated steel. Int. J. Adv. Manuf. Technol. 90(1–4):317–328
100. Reimann W, Pfriem S, Hammer T, Päthe D, Ungers M, Dilger K (2017) Influence of different zinc coatings on laser brazing of galvanized steel. J. Mater. Process. Technol. 239:75–82
101. Ogura T, Yokochi T, Netsu S, Saida K (2016) Microstructure and mechanical properties in laser brazing of A5052/AZ31 dissimilar alloys. Weld. World 60(5):1047–1054
102. Nelson GE (1965) Electron beam cutting control. US 3,172,989
103. Sullivan ABJ, Houldcroft PT (1967) Gas-jet laser cutting. Br. Weld. J. 14(8):443–445
104. Anon (1969) Cutting and Welding with the CO2 Laser. Met. Form 36:258–260
105. American Welding Society (2007) Laser beam welding, cutting, and associated processes. In: O'Brien GA, Guzman C (eds) Welding handbook volume 3 welding processes, part 2, 9th ed. American Welding Society, Miami, pp 504–530
106. Steen W, Mazumder J (2010) Laser Material Processing, 4th edn. Springer
107. American Welding Society C7 Committee (2010) AWS C7.2M: 2010 Recommended Practices for Laser Beam Welding, Cutting, and Allied Processes. American Welding Society
108. O'Neill W, Gabzdyl JT (2000) New developments in laser-assisted oxygen cutting. Opt. Lasers Eng. 34:355–367
109. Powell J, Tan WK, Maclennan P, Rudd D, Wykes C, Engstrom H (2000) Laser cutting stainless steel with dual focus lenses. J. Laser Appl. 12:224–231
110. Nielsen SE, Elllis N (2002) Dual-Focus Laser Cutting. Weld. World 46:33–40
111. Macken J (1992) Dual focus laser welding. US 5,155,323
112. Andreasch W, Huber R, Mock D (2011) Two concentric fiber diameters in one laser light cable: The 2in1 fiber makes it possible to weld and cut by means of simple optical exchange. Laser Tech. J. 8(1):38–41
113. Steigerwald KH (1957) Drilling by electrons. US 2,793,281
114. SPI lasers "A history of laser drilling." [Online]. Available: https://www.spilasers.com/application-drilling/history-laser-drilling/#:~:text=The link between laser cutting and laser drilling&text=This is unsurprising%2C given that,the laser drilling of diamonds. Accessed 08 Aug 2020
115. Beck T (2011) Laser drilling in gas turbine blades: Shaping of holes in ceramic and metallic coatings. Laser Tech. J. 8(3):40–43
116. Ancona A et al (2009) Femtosecond and picosecond laser drilling of metals at high repetition rates and average powers. Opt. Lett. 34(21):3304
117. Ancona A, Rademaker K, Röser F, Limpert J, Nolte S, Tünnermann A (2008) Laser drilling using a high repetition rate and high average power femtosecond fiber CPA system. Opt. Express 16(12):593–596
118. Grad L, Možina J (1998) Laser pulse shape influence on optically induced dynamic processes. Appl. Surf. Sci. 127–129:999–1004
119. Low DKY, Li L, Byrd PJ (2001) The influence of temporal pulse train modulation during laser percussion drilling. Opt. Lasers Eng. 35(3):149–164
120. Locke EV, Hella RA (1974) Metal Processing with a High-Power CO2 Laser. IEEE J. Quantum Electron. QE-10(2):179–185
121. Zenker R (2004) Structure and properties as a result of electron beam surface treatment. Adv. Eng. Mater. 6(7):581–588
122. Ion JC (2005) Surface hardening. In: Laser processing of engineering materials, 221–249
123. Zenker R, Buchwalder A (2013) Electron beam surface hardening. In: Dossett J, Totten GE (eds) ASM handbook, volume 4A, steel heat treating fundamentals and processes, vol 4A. ASM International, pp 76–77
124. Wilmoth M (2012) Laser paint stripping technology promising for heavy manufacturers [Online]. Available: https://ewi.org/video-laser-paint-stripping/. Accessed 30 June 2020

125. Chen GX, Kwee TJ, Tan KP, Choo YS, Hong MH (2010) Laser cleaning of steel for paint removal. Appl. Phys. A Mater. Sci. Process. 101(2):249–253
126. Schawlow AL (1971) Method and apparatus for erasing. US 3, 553,421
127. Hill JW, Lee MJ, Spalding IJ (1974) Surface treatments by laser. Opt. Laser Technol. 340:276–278
128. Lu YF, Takai M, Komuro S, Shiokawa T, Aoyagi Y (1994) Surface cleaning of metals by pulsed-laser irradiation in air. Appl. Phys. A Solids Surfaces. 59:281–288
129. Brygo F, Dutouquet C, Le Guern F, Oltra R, Semerok A, Weulersse JM (2006) Laser fluence, repetition rate and pulse duration effects on paint ablation. Appl. Surf. Sci. 252(6):2131–2138
130. Seo C, Ahn D, Kim D (2015) Removal of oxides from copper surface using femtosecond and nanosecond pulsed lasers. Appl Surf Sci. 349:361–367
131. Elmer JW, Hochanadel PW, Lachenberg K, Webber T (2011) Introduction to high energy density electron and laser beam welding. In: Lienert T, Siewert T, Babu S, Acoff V (eds) ASM handbook, volume 6A, welding fundamentals and processes, vol 6A. ASM International, pp 507–513
132. Assunção EG (2012) Investigation of conduction to keyhole mode transition. PhD Thesis. Cranfield University
133. Assunção EG, Williams S (2014) Effect of material properties on the laser welding mode limits. J. Laser Appl. 26(1). https://doi.org/10.2351/1.4826153
134. Webber T, Mazumder J, Lieb T (2011) Laser beam welding. In: Lienert T, Siewert T, Babu S, Acoff V (eds) ASM handbook, volume 6A, welding fundamentals and processes, vol 6A. ASM International, pp 86–89
135. Bransch HN, Weckman DC, Kerr HW (1994) Effects of Pulse Shaping on Nd:YAG Spot Welds in Austenitic Stainless Steel. Weld. World (June):141–151
136. Fuerschbach PW, Hinkley DA (1997) Pulsed Nd:YAG laser welding of Cardiac pacemaker batteries with reduced heat input. Weld. J. 76(12):103s–109s
137. Cho JH, Farson DF, Reiter MJ (2009) Analysis of penetration depth fluctuations in single-mode fibre laser welds. J. Phys. D. Appl. Phys 42(11)
138. Lee JY, Ko SH, Farson DF, Yoo CD (2002) Mechanism of keyhole formation and stability in stationary laser welding. J. Phys. D. Appl. Phys. 35(13):1570–1576
139. Matsunawa A (2002) Science of laser welding - mechanisms of keyhole and pool dynamics. In: ICALEO 2002 - 21st International Congress on Applications of Laser and Electro-Optics, Congress Proceedings, 290
140. Matsunawa A, Kim J-D, Seto N, Mizutani M, Katayama S (1998) Dynamics of keyhole and molten pool in laser welding. J. Laser Appl. 10(6):247–254
141. Dowden J (2009) Laser keyhole welding: the vapour phase. In: Dowden J (ed) The theory of laser materials processing: heat and mass transfer in modern technology. Springer, pp 113–151
142. Jouvard JM, Girard K, Perret O (2001) Keyhole formation and power deposition in Nd:YAG laser spot welding. J. Phys. D. Appl. Phys. 34(18):2894–2901
143. Fujinaga S, Takenaka H, Narikiyo T, Katayama S, Matsunawa A (2000) Direct observation of keyhole behaviour during pulse modulated high-power Nd:YAG laser irradiation. J. Phys. D. Appl. Phys. 33(5):492–497
144. Patterson T, Hochanadel JE (2019) Ohio State University Unpublished Data. Columbus, OH
145. Kaplan A (1994) A model of deep penetration laser welding based on calculation of the keyhole profile. J. Phys. D. Appl. Phys. 27(9):1805–1814
146. Jiang M, Chen YB, Chen X, Toa W, Debroy T (2020) Enhanced Penetration Depth during Reduced Pressure Keyhole-Mode Laser Welding. Weld. J 99(4)
147. Fabbro R, Hirano K, Pang S (2016) Analysis of the physical processes occurring during deep penetration laser welding under reduced pressure. J. Laser Appl. 28(2)
148. Katayama S, Kawahito Y, Mizutani M (2012) Latest Progress in Performance and Understanding of Laser Welding. Phys. Procedia 39:8–16
149. Shcheglov PY, Gumenyuk AV, Gornushkin IB, Rethmeier M, Petrovskiy VN (2013) Vapor-plasma plume investigation during high-power fiber laser welding. Laser Phys. 23(1)
150. Zou J, Yang W, Wu S, He Y, Xiao R (2016) Effect of plume on weld penetration during high-power fiber laser welding. J Laser Appl. 28(2)
151. Knight CJ (1979) Theoretical Modeling of Rapid Surface Vaporization with Back Pressure. AIAA J. 17(5):519–523
152. He X, Norris JT, Fuerschbach PW, Debroy T (2006) Liquid metal expulsion during laser spot welding of 304 stainless steel. J. Phys. D. Appl. Phys. 39(3):525–534
153. Semak V, Matsunawa A (1997) The role of recoil pressure in energy balance during laser materials processing. J Phys D Appl Phys. 30:2541–2552
154. Heiple CR, Roper JR, Stagner RT, Aden RJ (1983) Surface Active Element Effects on the Shape of Gta, Laser, and Electron Beam Welds. Weld. J. 62(3):72–77
155. Kou S, Limmaneevichitr C, Wei PS (2011) Oscillatory Marangoni flow: a fundamental study by conduction-mode laser spot welding. Weld. J. 90(12):229s–240s
156. Kou S (2003) Welding Metallurgy, 2nd edn. John Wiley & Sons, Inc.
157. Heiple CR, Roper JR (1982) Mechanism for Minor Element Effect on Gta Fusion Zone Geometry. Weld. J. 61(4)
158. Kaplan A (2009) Keyhole welding: the solid and liquid phases. In: Dowden J (ed) The theory of laser materials processing: heat and mass transfer in modern technology. Springer, pp 71–93
159. Katayama S, Seto N, Do Kim J, Matsunawa A (1997) Formation mechanism and reduction method of porosity in laser welding of stainless steel. Laser Inst. Am. Proc. 83(2)
160. Miyagi M, Wang J (2020) Keyhole dynamics and morphology visualized by in-situ X-ray imaging in laser melting of austenitic stainless steel. J Mater Process Technol. 282
161. Tenner F, Berg B, Brock C, Klämpfl F, Schmidt M (2015) Experimental approach for quantification of fluid dynamics in laser metal welding. J. Laser Appl. 27(S2):1–8
162. Eriksson I, Powell J, Kaplan AFH (2013) Melt behavior on the keyhole front during high speed laser welding. Opt. Lasers Eng. 51(6):735–740
163. De A, DebRoy T (2004) A smart model to estimate effective thermal conductivity and viscosity in the weld pool. J. Appl. Phys. 95(9):5230–5240
164. Rai R, Elmer JW, Palmer TA, Debroy T (2007) Heat transfer and fluid flow during keyhole mode laser welding of tantalum, Ti-6Al-4V, 304L stainless steel and vanadium. J. Phys. D. Appl. Phys. 40(18):5753–5766
165. Rai R, Burgardt P, Milewski JO, Lienert TJ, Debroy T (2009) Heat transfer and fluid flow during electron beam welding of 21Cr-6Ni-9Mn steel and Ti-6Al-4V alloy. J. Phys. D. Appl. Phys. 42(2)
166. Dowden J, Davis M, Kapadia P (1985) The flow of heat and the motion of the weld pool in penetration welding with a laser. J. Appl. Phys. 57(9):4474–4479
167. Choo RTC, Szekely J (1994) Possible role of turbulence in GTA weld pool behavior. Weld. J. 73(2):25–31
168. Nakamura H, Kawahito Y, Nishimoto K, Katayama S (2015) Elucidation of melt flows and spatter formation mechanisms

during high power laser welding of pure titanium. J. Laser Appl. 27(3):1–10
169. Mackwood AP, Crafer RC (2005) Thermal modelling of laser welding and related processes: A literature review. Opt. Laser Technol. 37(2):99–115
170. Svenungsson J, Choquet I, Kaplan AFH (2015) Laser welding process - a review of keyhole welding modelling. Phys. Procedia. In: 15th Nordic laser materials processing conference
171. Rosenthal D (1941) Mathematical Theory of Heat Distribution During Welding and Cutting. Weld. J. 20(5):220s–234s
172. Rosenthal D (1946) The Theory of Moving Sources of Heat and Its Application to Metal Treatments. Trans. ASME 68:848–866
173. Swift-Hook DT, Gick AEF (1973) Penetration Welding with Lasers. Weld. J. (11):492s–499s
174. Klemens PG (1976) Heat balance and flow conditions for electron beam and laser welding. J. Appl. Phys. 47(5):2165–2174
175. Mazumder J, Steen WM (1980) Heat transfer model for cw laser material processing. J. Appl. Phys. 51(2):941–947
176. Miyazaki T, Giedt WH (1982) Heat transfer from an elliptical cylinder moving through an infinite plate applied to electron beam welding. Int. J. Heat Mass Transf. 25(6):807–814
177. Goldak J, Chakravarti A, Bibby M (1984) A new finite element model for welding heat sources. Metall. Trans. B 15B(6):299–305
178. Sudnik W, Radaj D, Erofeew W (1996) Computerized simulation of laser beam welding, modelling and verification. J. Phys. D. Appl. Phys. 29(11):2811–2817
179. Matsunawa A, Semak V (1997) The simulation of front keyhole wall dynamics during laser welding. J. Phys. D. Appl. Phys. 30(5): 798–809
180. Ki H, Mohanty PS, Mazumder J (2002) Role of recoil pressure, multiple reflections, and free surface evolution during laser keyhole welding. Metall. Mater. Trans. A 33(June):1817–1830
181. Rai R, Kelly SM, Martukanitz RP, DebRoy T (2006) Experimental and computational investigation of fusion zone geometries during autogenous keyhole mode laser welds. In: ICALEO 2006 - 25th international congress on applications of laser and electro-optics, congress proceedings, 805
182. Amara EH, Fabbro R (2008) Modelling of gas jet effect on the melt pool movements during deep penetration laser welding. J. Phys. D. Appl. Phys. 41(5)
183. Hann DB, Iammi J, Folkes J (2011) A simple methodology for predicting laser-weld properties from material and laser parameters. J. Phys. D. Appl. Phys. 44(44)
184. Trivedi R et al (2003) In situ observations of weld pool solidification using transparent metal-analog systems. J. Appl. Phys. 93(8): 4885–4895
185. Rappaz M, David SA, Vitek JM, Boatner LA (1989) Development of microstructures in Fe-15Ni-15Cr single crystal electron beam welds. Metall. Trans. A 20(6):1125–1138
186. Rappaz M, David SA, Vitek JM, Boatner LA (1990) Analysis of solidification microstructures in Fe-Ni-Cr single-crystal welds. Metall. Trans. A 21(6):1767–1782
187. David SA, Vitek JM, Babu SS, Boatner LA, Reed RW (1997) Welding of nickel base superalloy single crystals. Sci. Technol. Weld. Join. 2(2):79–88
188. Liu H, Nakata K, Zhang JX, Yamamoto N, Liao J (2012) Microstructural evolution of fusion zone in laser beam welds of pure titanium. Mater. Charact. 65:1–7
189. Lu W, Shi Y, Lei Y, Li X (2012) Effect of electron beam welding on the microstructures and mechanical properties of thick TC4-DT alloy. Mater. Des. 34:509–515
190. Akman E, Demir A, Canel T, Sinmazçelik T (2009) Laser welding of Ti6Al4V titanium alloys. J. Mater. Process. Technol. 209(8): 3705–3713
191. Wei HL, Elmer JW, DebRoy T (2017) Three-dimensional modeling of grain structure evolution during welding of an aluminum alloy. Acta Mater. 126:413–425
192. Wei HL, Elmer JW, DebRoy T (2017) Crystal growth during keyhole mode laser welding. Acta Mater. 133:10–20
193. Baeslack WA, Davis JR, Cross CE (1993) Selection and weldability of conventional titanium alloys. In: Olson DL, Siewert TA, Liu S, Edwards GR (eds) ASM handbook, volume 6: welding, brazing, and soldering, vol 6. ASM International, pp 507–523
194. Lippold JC, Kotecki DJ (2005) Welding Metallurgy and Weldability of Stainless Steels. John Wiley & Sons, Inc.
195. Cam G, Erim S, Yeni Ç, Koçak M (1999) Determination of mechanical and fracture properties of laser beam welded steel joints. Weld J. 78(6):193s–201s
196. Coelho RS, Kostka A, Pinto H, Riekehr S, Koçak M, Pyzalla AR (2008) Microstructure and mechanical properties of magnesium alloy AZ31B laser beam welds. Mater. Sci. Eng. A 485:20–30
197. Riofrío PG, Capela CA, Ferreira JAM, Ramalho A (2020) Interactions of the process parameters and mechanical properties of laser butt welds in thin high strength low alloy steel plates. Proc. Inst. Mech. Eng. Part L J. Mater. Des. Appl. 234(5):665–680
198. Benyounis KY, Olabi AG, Hashmi MSJ (2005) Effect of laser welding parameters on the heat input and weld-bead profile. J. Mater. Process. Technol. 164–165:978–985
199. David SA, Vitek JM (1989) Correlation between solidification parameters and weld microstructures. Int. Mater. Rev. 34(1):213–245
200. Elmer JW, Eagar TW, Allen SM (1990) Single-phase solidification during rapid-resolidification of stainless steel alloys. In: Proc. of the materials weldability symposium, pp 143–150
201. Elmer JW, Allen SM, Eagar TW (1989) Microstructural Development during Solidification of Stainless Steel Alloys. Metall. Trans. A 20A(October):2117–2131
202. Vitek JM, Dasgupta A, David SA (1983) Microstructural Modification of Austenitic Stainless Steels By Rapid Solidification. Metall Trans A, Phys Metall Mater. Sci. 14 A(9): 1833–1841
203. Schaeffler AL (1949) Constitution Diagram for Stainless Steel Weld Metal. Met. Prog 56(11):680, 680B
204. Long CJ, Delong WT (1973) The Ferrite Content of Austenitic Stainless Steel Weld Metal. Weld. J. (7):281s-297s
205. Kotecki DJ, Siewart TA (1992) WRC-1992 Constitution Diagram for Stainless Steel Weld Metals : A Modification of the WRC-1988 Diagram. Weld. J. (5):171s-178s
206. Brooks JA, Baskes MI, Greulich FA (1991) Solidification Modeling and Solid-State Transformations in High-Energy Density Stainless Steel Welds. Metall. Trans. A 22A(4):915–926
207. David SA, Vitek JM, Hebble TL (1987) Effect of Rapid Solidification on Stainless Steel Weld Metal Microstructures and Its Implications on the Schaeffler Diagram. Weld. J. (8): 289s-300s
208. Lippold JC (1994) Solidification Behavior and Cracking Susceptibility of Pulsed-Laser Welds in Austenitic Stainless Steels. Weld. J. 73(6):129s-139s
209. Lippold JC (1985) Centerline Cracking in Deep Penetration Electron Beam Welds in Type 304L Stainless Steel. Weld. J. (5):127s–136s
210. Kujanpaa V, Suutala N, Takalo T, Moisio T (1979) Correlation between solidification cracking and microstructure in austenitic and austenitic-ferritic stainless steel welds. Weld. Res. Int. 9(2):55–75
211. Lienert TJ, Lippold JC (2003) Improved weldability diagram for pulsed laser welded austenitic stainless steels. Sci. Technol. Weld. Join. 8(1):1–9
212. Hammar O, Svennson U (1979) Influence of steel composition on segregation and microstructure during solifification of austenitic stainless steels. Solidif. Cast. Met. 192:401–410

213. Hochanadel P, Lienert T, Martinez R, Martinez J, Johnson M (2011) Weld solidification cracking in 304 to 304L stainless steel. In: Lippold JC, Bollinghaus T, Cross CE (eds) Hot cracking phenomena in welds III. Springer, pp 145–160
214. Kumar P, Sinha AN (2019) Effect of heat input in pulsed Nd:YAG laser welding of titanium alloy (Ti6Al4V) on microstructure and mechanical properties. Weld. World 63(3):673–689
215. Saresh N, Pillai MG, Mathew J (2007) Investigations into the effects of electron beam welding on thick Ti-6Al-4V titanium alloy. J. Mater. Process. Technol. 192–193:83–88
216. Kohyamaa A, Arata Y, Tomie M, Igata N (1984) Electron Beam Welding of Titanium and Ti-6Al-4V Thick Plates. J. Nucl. Mater. 122(1–3):772–776
217. Casalino G, Mortello M, Campanelli SL (2015) Ytterbium fiber laser welding of Ti6Al4V alloy. J. Manuf. Process. 20:250–256
218. Karlsson L (2012) Welding duplex stainless steels - A review of current recommendations. Weld. World 56(5–6):65–76
219. Verma J, Taiwade RV (2017) Effect of welding processes and conditions on the microstructure, mechanical properties and corrosion resistance of duplex stainless steel weldments—A review. J. Manuf. Process. 25:134–152
220. Muthupandi V, Bala Srinivasan P, Seshadri SK, Sundaresan S (2003) Effect of weld metal chemistry and heat input on the structure and properties of duplex stainless steel welds. Mater. Sci. Eng. A 358(1–2):9–16
221. Sieurin H, Sandström R (2006) Austenite reformation in the heat-affected zone of duplex stainless steel 2205. Mater. Sci. Eng. A 418(1–2):250–256
222. Bolut M, Kong CY, Blackburn J, Cashell KA, Hobson PR (2016) Yb-fibre laser welding of 6 mm duplex stainless steel 2205. Phys. Procedia 83:417–425
223. Kolenič F, Kovac L, Drimal D (2011) Effect of laser welding conditions on austenite/ferrite ratio in duplex stainless steel 2507 welds. Weld. World 55(5–6)
224. Taban E, Kaluc E (2011) Welding behaviour of duplex and superduplex stainless steels using laser and plasma arc welding processes. Weld. World 55(7–8):48–57
225. Collur MM, Paul A, Debroy T (1987) Mechanism of alloying element vaporization during laser welding. Metall. Trans. B 18(4):733–740
226. Pastor M, Zhao H, Martukanitz RP, Debroy T (1999) Porosity, underfill and magnesium loss during continuous wave Nd:YAG laser welding of thin plates of aluminum alloys 5182 and 5754. Weld. J. 78(6):207s–216s
227. Khan PAA, Debroy T, David SA (1988) Laser Beam Welding of High-Manganese Stainless Steels - Examination of Alloying Element Loss and Microstructural Changes. Weld. J. (1):2s-7s
228. Berger J (2018) Effect of preferential vaporization during laser rewelding on the solidification and cracking response of type 304L stainless steel alloys with systematically varied manganese contents. Masters Thesis. The Ohio State University
229. American Welding Society (2001) Survey of joining, cutting, and allied processes. In: Welding handbook volume 1 welding science and technology, 9th edn. American Welding Society, pp 1–50
230. Bauer B, Matija B (2011) High Energy Density Welding Processes. In: Welding Engineering and Technology
231. Benedict GF (1987) Nontraditional Manufacturing Processes, 1st ed. CRC Press
232. W glowski MS, Błacha S, Phillips A (2016) Electron beam welding - Techniques and trends - Review. Vacuum 130(5):72–92
233. Eagar TW, Mazzeo AD (2011) Welding Process Fundamentals. In: Lienert T, Siewert T, Babu S, Acof V (eds) ASM Handbook, Volume 6A, Welding Fundamentals and Processes, vol 6A. ASM International, pp 29–34
234. Schultz H (1994) Electron Beam Welding. Woodhead Publishing
235. "How do I produce a vacuum for EB welding?," The Welding Institute. [Online]. Available: https://www.twi-global.com/technical-knowledge/faqs/faq-how-do-i-produce-a-vacuum-for-eb-electron-beam-welding. Accessed 17 Aug 2020
236. Koleva EG, Mladenov GM (2011) Experience on electron beam welding. In: Nemtanu MR, Brasoveanu M (eds) Practical aspects and applications of electron beam irradiation. pp 95–133
237. Energy Beam Sciences (2020) Hamiliton Standard and Leybold Heraeus, [Online]. Available: https://ebsciences.com/product-category/electron-beam-welding-filaments/hamiliton-standard-and-lybold-heraeus/. Accessed 17 Aug 2020
238. Burgardt P (2017) "Personal correspondence on coupling efficiency and HED depth of penetration"
239. Burgardt P (2017) HED Welding Lecture Series: Electron Beam Sessions. Los Alamos National Laboratory
240. Iqbal M, Rafiq M, Bhatti SA, Aleem FE (2004) The electron beam gun with thermionic hairpin-like cathode for welding and surface modifications. Vacuum 77(1):19–26
241. Pratihar DK, Dey V (2012) Electron Beams for Macro- and Microwelding Applications. In: Jain VK (ed) Micromanufacturing Processes. Taylor & Francis Group, pp 221–240
242. Wang S, Wu X (2012) Investigation on the microstructure and mechanical properties of Ti-6Al-4V alloy joints with electron beam welding. Mater. Des. 36:663–670
243. Dora J, Felba J, Sielanko W (2005) A new generation of power supplies for electron beam welding machines. Vacuum 77(4): 463–467
244. Sanderson A (2007) Four decades of electron beam development at TWI. Weld. World 51(1–2):37–49
245. Baechler WG (1987) Cryopumps for research and industry. Vacuum 37(1–2):21–29
246. The Welding Institute (2020) The correct electron beam (EB) welding chamber pump vacuum. [Online]. Available: https://www.twi-global.com/technical-knowledge/faqs/faq-why-wont-my-electron-beam-eb-welding-chamber-pump-down-to-the-usual-vacuum. Accessed 17 Aug 2020
247. Kautz D, Olson D, Burgardt P, Edwards G (1991) A Characterization of Pulsed Electron Beam Welding Parameters. Weld. J. 70(4):100
248. Qi B, Fan J, Zhang W, Liu F, Wang H (2016) A novel control grid bias power supply for high-frequency pulsed electron beam welding. Vacuum 133:46–53
249. Dong C et al (2003) Surface treatment by high current pulsed electron beam. Jinshu Rechuli/Heat Treat. Met. 33(1):620–624
250. Burgardt P, Pierce SW, Dvornak MJ (2016) Definition of beam diameter for electron beam welding. Los Alamos National Laboratory
251. Ferrario M, Migliorati M, Palumbo L (2013) Space charge effects. In: Proceedings of the CAS-CERN accelerator school: advanced accelerator physics, pp 331–356
252. Anderson SG, Rosenzweig JB, LeSage GP, Crane JK (2002) Space-charge effects in high brightness electron beam emittance measurements. Phys. Rev. Spec. Top. - Accel. Beams 5(1):12–23
253. Hochanadel JE, Patterson T, Lippold JC, Panton B, Johnson MQ, Tung DC (2021) Influence of Focus and Deflection when Comparing Electron Beam Welds to Laser Welds at Varying Parameters in 304 SS. Weld. World
254. Ho CY (2005) Fusion zone during focused electron-beam welding. J. Mater. Process. Technol. 167(2–3):265–272
255. Murphy JL, Mustaleski TM, Watson LC (1988) Multipass, Autogenous Electron Beam Welding. Weld. J. 67(9):187s-195s
256. Chowdhury S, Yadaiah N, Mujaheed Khan S, Ozah R, Das B, Muralidhar M (2018) A Perspective Review on Experimental Investigation and Numerical Modeling of Electron Beam Welding Process. Mater. Today Proc. 5(2):4811–4817

257. Alyackrinskiy ON et al (2018) Experiments with EBW setup with possibility of right angle beam turn. Electrotech. Electron. 53:5–6
258. Pierce SW, Burgardt P (2016) Comparison of Beam Defocus and Beam Oscillation for Ta-10W EB Welding. Los Alamos National Laboratory
259. Pierce SW (1993) Thermocapillarity and arc phenomena in stainless steel welds. Masters Thesis. Colorado School of Mines
260. Pierce SW, Burgardt P, Olson DL (1999) Thermocapillary and arc phenomena in stainless steel welding. Weld. J. (2):45s–52s
261. Elmer JW, Giedt WH, Eagar TW (1990) The Transition from Shallow to Deep Penetration during Electron Beam Welding Empirical. Weld. J. (5):167s–176s
262. Tong H, Giedt WH (1970) A Dynamic Interpretation of Electron Beam Welding. Weld. J. 49:259–266
263. Petrov P, Georgiev C, Petrov G (1998) Experimental investigation of weld pool formation in electron beam welding. Vacuum 51(3): 339–343
264. Mara GL, Funk ER, McMaster RC, Pence PE (1974) Penetration Mechanisms of Electron Beam Welding and the Spiking Phenomenon. Weld. J. 53(6)
265. Tong H, Giedt WH (1969) Radiographs of the electron beam welding cavity. Rev. Sci. Instrum. 40(10):1283–1285
266. Arata V (1986) Fundamental characteristics of high energy density beams in material processing. In: International congress on applications of lasers & electro-optics 73:73–79
267. Schauer DA, Giedt WH (1978) Prediction of Electron Beam Welding Spiking Tendency. Weld. J. 57(7):189–195
268. Kubo T, Ajima Y, Nagata T, Saeki T (2012) Relations between electron beam welding parameters and appearances of weld beads on Nb plates. In: 9th meeting of particle accelerator society of Japan, pp 1137–1142
269. Nunes JAC (1985) A comparison of the physics of gas tungsten arc welding (GTAW), electron beam welding (EBW), and laser beam welding (LBW). National Aeronautics and Space Administration
270. Rai R (2008) Modeling of heat transfer and fluid flow in keyhole mode welding. PhD Dissertation. Pennsylvania State University
271. Burgardt P, Heiple C (1992) Weld penetration sensitivity to welding variables when near full joint penetration. Weld. J. 71(9):341
272. Giedt WH, Tallerico LN (1988) Prediction of electron beam depth of penetration. Weld. J. 67(12):299s-306s
273. Yost TE (2015) Effects of select parameters on electron beam welding of AA6061-T6 alloy. Masters Thesis. Colorado School of Mines
274. Thomas G, Ramachandra V, Nagarajan KV, Pant B, Sarkar BK, Vasudevan R (1989) Electron Beam Welding Studies of 25-mm-Thick Ti-6Al-4V Sections. Weld. J. 68(8):336–341
275. Grecu L, Demian G, Demian M, Grecu V (2009) The Influence of Welding Parameters on Temperature Distribution in Case of EBW. In: Katalinic B (ed) DAAAM International Scientific Book. DAAAM International, Vienna, Austria, pp 35–44
276. Dragunov VK, Terentyev EV, Sliva AP, Goncharov AL, Zhgut DA (2019) Analytical methods of electron beam power evaluation for electron-beam welding with deep penetration. IOP Conf. Ser. Mater. Sci. Eng. 681(1)
277. Sarafan S, Wanjara P, Champliaud H, Mathieu L, Lanteigne J (2013) Characteristics of electron beam welded CA6NM. In: Materials Science and Technology Conference and Exhibition 2013, MS and T 2013, pp 720–732
278. Patel V, Sali A, Hyder J, Corliss M, Hyder D, Hung W (2020) Electron Beam Welding of Inconel 718. Procedia Manuf. 48:428–435
279. Electron beam welding, The Open University, 2018. [Online]. Available: https://www.open.edu/openlearn/science-maths-technology/engineering-technology/manupedia/electron-beam-welding. Accessed 17 Aug 2020
280. Weidner CW, Shuler LE (1973) Effect of Process Variables on Partial Penetration Electron Beam Welding. Weld. J. (3):115s-119s
281. Dragunov VK, Terentev EV, Sliva AP, Goncharov AL, Marchenkov AY (2017) Determination of welding speed in electron beam welding of thick components with continuous penetration. Weld. Int. 31(4):307–311
282. Trushnikov DN, Belenki'y VY, Mladenov GM, Portnov NS (2012) Secondary-Emission signal for weld formation monitoring and control in eletron beam welding (EBW). Materwiss. Werksttech. 43(10):892–897
283. Schubert G (2009) Electron beam welding - Process, applications and equipment. Weld. World 53:283–288
284. Burgardt P, Hochanadel PW, Duffield AN, Kautz DO (2008) Electron beam welding of 21-6-9 stainless steel using both circle deflection and defocus settings. Los Alamos National Laboratory
285. Trushnikov DN, Koleva EG, Mladenov GM, Belenkiy VY (2013) Effect of beam deflection oscillations on the weld geometry. J. Mater. Process. Technol. 213(9):1623–1634
286. Varushkin S, Trushnikov D, Permyakov G (2017) Optimal Mode of Beam Oscillation for Melt-Through Mode in Electron Beam Welding and Its Influence on Penetration Control System. Procedia Eng. 206:1360–1364
287. Vadolia GR, Premjit Singh K (2017) Electron Beam Welding: study of process capability and limitations towards development of nuclear components. Journal of Physics: Conference Series 823(1)
288. Mohandas T, Banerjee D, Kutumba Rao VV (1999) Fusion Zone Microstructure and Porosity in Electron Beam Welds of an $\alpha + \beta$ Titanium Alloy. Metall. Mater. Trans. A Phys. Metall. Mater. Sci. 30A:789–798
289. Kaplan AFH, Powell J (2011) Spatter in laser welding. J Laser Appl. 23(3):032005
290. Brooks JA (1975) Weldability of High N, High Mn Austenitic Stainless Steel. Weld. J. 54(6):189s-195s
291. Baufeld B, Priest J, Dutilleul T (2019) EBW of nuclear pressure vessel steels. Electrotech. Electron. 53(12):5–6
292. Iwashita Y et al (2013) Update on study of welding porosity in Nb EBW. In: Proceedings of SRF2013, pp 567–569
293. Kar J, Chakrabarti D, Roy SK, Roy GG (2019) Beam oscillation, porosity formation and fatigue properties of electron beam welded Ti-6Al-4V alloy. J. Mater. Process. Technol. 266:165–172
294. Sliva AP, Dragunov VK, Terentyev EV, Goncharov AL (2018) EBW of aluminium alloys with application of electron beam oscillation. J. Phys. Conf. Ser. 1089:012005
295. Dinda SK, Kar J, Jana S, Gopal Roy G, Srirangam P (2019) Effect of beam oscillation on porosity and intermetallics of electron beam welded DP600-steel to Al 5754-alloy. J. Mater. Process. Technol. 265(10):191–200
296. Bandi B, Dinda SK, Kar J, Roy GG, Srirangam P (2018) Effect of weld parameters on porosity formation in electron beam welded Zircaloy-4 joints: X-ray tomography study. Vacuum 158(7):172–179
297. Hershcovitch A (2005) Non-vacuum electron beam welding through a plasma window. Nucl. Instruments Methods Phys. Res. Sect. B Beam Interact. with Mater. Atoms 241(1–4):854–857
298. Bach FW, Szelagowski A, Versemann R, Zelt M (2003) Non vacuum electron beam welding of light sheet metals and steel sheets. Weld. World 47(3–4):4–10
299. Hadley P. Emmision current, *TU Graz*. [Online]. Available: http://lamp.tu-graz.ac.at/~hadley/sem/faraday/faraday.php. Accessed 07 Aug 2020
300. Burgardt P (2007) Vacuum effects in electron beam welding, Los Alamos National Laboratory
301. Schwarz H (1962) Power Density of Optimally Focused Space-Charge-Limited Electron Beams. J Appl Phys. 33(12):3464–3470
302. America IAM (2016) Laser Welding Fundamentals. Amada Miyachi America, INC., Monrovia, California, USA

303. Stellwag WL (2012) Fiber laser wedling of 304 stainless steel and the effects of various parameters on materials coupling and back-reflection. Masters Thesis. The Ohio State University
304. Gahan BC, Shiner B (2004) New High-Power Fiber Laser Enables Cutting-Edge Research. Laser Technol.:29–31
305. Koechner W (2007) Solid-state laser engineering. In: Rhodes WT (ed) 6th edn. Springer
306. Kruse J (2013) Introduction: fundamentals of laser welding. In: Katayama S (ed) Handbook of Laser Welding Technologies. Woodhead Publishing, pp 3–16
307. Bidin N, Kee LP (2010) Comparison of ND : YAG laser beam quality between free running and Q-switched modes. J Fiz Malaysia 31(1–4):15–20
308. IPG Photonics Inc. (2020) Diode laser systems [Online]. Available: https://www.ipgphotonics.com/en/products/lasers/diode-laser-systems. Accessed 19 May 2020
309. Trumpf (2020) Diode lasers [Online]. Available: https://www.trumpf.com/en_US/products/laser/diode-lasers/. Accessed 19 May 2020
310. Sharma RS, Molian P (2011) Weldability of advanced high strength steels using an Yb: YAG disk laser. J Mater Process Technol. 211(11):1888–1897
311. Löffler K (2013) Developments in disk laser welding. Handb. Laser Weld. Technol.:73–102
312. Zhang LJ, Zhang JX, Gumenyuk A, Rethmeier M, Na SJ (2014) Numerical simulation of full penetration laser welding of thick steel plate with high power high brightness laser. J. Mater. Process. Technol. 214(8):1710–1720
313. Smrz M, Divoky M (2019) Diode pumped high power lasers. In: Divliansky I (ed) Advances in High-Power Fiber and Diode Laser Engineering. The Institution of Engineering and Technology, London, pp 156–197
314. Zervas MN, Codemard CA (2014) High Power Fiber Lasers: A Review. IEEE J. Sel. Top. Quantum Electron. 20(5)
315. IPG Photonics Inc. (2020) YLS, 1-120+ kW [Online]. Available: https://www.ipgphotonics.com/en/products/lasers/high-power-cw-fiber-lasers/1-micron/yls-1-120-kw. Accessed 14 Nov 2020
316. Richter K, Behr W, Reisgen U (2007) Low Heat Welding of Titanium Materials with a Pulsed Nd:YAG Laser. Materwiss. Werksttech. 38(1):51–56
317. Zediker MS, Fritz RD, Finuf MJ, Pelaprat JM (2019) Stable key-hole welding of 1 mm thick copper with a 600 W blue laser system. J Laser Appl. 31(2)
318. Deile J, Villarreal FJ (2011) Carbon Dioxide Lasers. In: Injeyan H, Goodno GD (eds) High-Power LaserPower Laser. Inc, McGraw-Hill Companies, pp 3–16
319. Mazumder J, Webber T (2011) Laser Beam Weld Design , Codes , and Quality Assessment. In: Lienert T, Siewert TA, Babu S, Acoff V (eds) ASM Handbook, Volume 6A, Welding Fundamentals and Processes, vol 6A. ASM International
320. Rath W (2007) CO2 Lasers : Modern Workhorses in the World of Industrial Manufacturing. Laser Tech. J. 3(6):34–39
321. IPG Photonics Inc. YLS-AMB adjustable mode beam lasers [Online]. Available: https://www.ipgphotonics.com/en/217/FileAttachment/AMB+Welding+Benefits.pdf. Accessed 25 Aug 2020
322. Goodno GD, Hagop (2011) Introduction to High-Power Solid-State Lasers. In: Injeyan H, Goodno GD (eds) High-Power Laser Handbook
323. Kanskar M (2019) Diode laser: fundamentals and improving brightness. In: Divliansky I (ed) Advances in high-power fiber and diode laser engineering, pp 1–36
324. Laserline GmbH (2020) LDF series - mobile high power diode laser [Online]. Available: https://www.laserline.com/en-int/ldfseries/. Accessed 25 Aug 2020
325. Smrž M et al (2017) Advances in high-power, Ultrashort pulse DPSSL technologies at HiLASE. Appl. Sci. 7(10)
326. Koechner W (2006) Mode locking. In: Rhodes WT (ed) Solid-state laser engineering, 6th edn. Springer, pp 534–586
327. Dong L, Fermann ME (2011) Introduction to Optical Fiber Lasers. In: Injeyan H, Goodno GD (eds) High-Power Laser Handbook. McGraw-Hill Companies, Inc., pp 413–462
328. Blecher J, Palmer TA, Kelly SM, Martukanitz RP (2012) Identifying performance differences in transmissive and reflective laser optics using beam diagnostic tools. Weld. J. 91(7)
329. Reitemeyer D, Seefeld T, Vollertsen F (2010) Online focus shift measurement in high power fiber laser welding. Phys Procedia 5:455–463
330. Klein CA (2007) Materials for high-energy laser windows: how thermal lensing and thermal stresses control the performance. Opt. Mater. Struct. Technol. III
331. Miyamoto I, Nanba H, Maruo H (1990) Analysis of thermally induced optical distortion in lens during focusing high-power CO2 laser beam. In: CO2 Lasers and Applications II, pp 112–121
332. Fuerschbach PW (1996) Measurement and prediction of energy transfer efficiency in laser beam welding. Weld. J. 75(1):24s–34s
333. Ream SL (2004) Laser welding efficiency and cost: CO2, YAG, fiber, and disc. In: Proceedings of the 23rd international congress on applications of lasers and electro-optics
334. Webber TC (1996) Laser welding melt efficiency comparison: cw and Q-switched Nd:YAG. Lasers as Tools Manuf. Durable Goods Microelectron 2703:162–169
335. Xie J, Kar A, Rothenflue JA, Latham WP (1997) Temperature-dependent absorptivity and cutting capability of CO2, Nd:YAG and chemical oxygen–iodine lasers. J. Laser Appl. 9(2):77–85
336. Quintino L, Costa A, Miranda R, Yapp D, Kumar V, Kong CJ (2007) Welding with high power fiber lasers - A preliminary study. Mater. Des. 28(4):1231–1237
337. Mazumder J (1982) Laser Welding: State of the Art Review. JOM J. Miner. Met. Mater. Soc. 34(7):16–24
338. Cai C, Peng GC, Li LQ, Chen YB, Qiao L (2014) Comparative study on laser welding characteristics of aluminium alloy under atmospheric and subatmospheric pressures. Sci. Technol. Weld. Join. 19(7):547–553
339. Schneider M, Berthe L, Fabbro R, Muller M (2008) Measurement of laser absorptivity for operating parameters characteristic of laser drilling regime. J Phys D Appl Phys. 41(15)
340. Kaplan AFH (2012) Fresnel absorption of 1 μm- and 10 μm-laser beams at the keyhole wall during laser beam welding: Comparison between smooth and wavy surfaces. Appl. Surf. Sci. 258(8):3354–3363
341. Sánchez-Amaya JM, Delgado T, De Damborenea JJ, Lopez V, Botana FJ (2009) Laser welding of AA 5083 samples by high power diode laser. Sci. Technol. Weld. Join 14(1):78–86
342. Hess A, Schuster R, Heider A, Weber R, Graf T (2011) Continuous wave laser welding of copper with combined beams at wavelengths of 1030 nm and of 515 nm. Phys. Procedia 12:88–94
343. Bergmann JP, Bielenin M, Feustel T (2015) Aluminum welding by combining a diode laser with a pulsed Nd:YAG laser. Weld. World 59(2):307–315
344. Volpp J, Vollertsen F (2015) Modeling keyhole oscillations during laser deep penetration welding at different spatial laser intensity distributions. Prod. Eng. 9(2):167–178
345. Kaplan AFH (2012) Absorptivity modulation on wavy molten steel surfaces: The influence of laser wavelength and angle of incidence. Appl Phys Lett. 101(15)
346. Gao M, Chen C, Hu M, Guo L, Wang Z, Zeng X (2015) Characteristics of plasma plume in fiber laser welding of aluminum alloy. Appl. Surf. Sci. 326:181–186

347. Scholz T, Dickmann K, Ostendorf A, Uphoff H, Michalewicz M (2015) Effect of process parameters on the formation of laser-induced nanoparticles during material processing with continuous solid-state lasers. J Laser Appl. 27(3):032001
348. Walsh CA (2002) LASER WELDING - Literature Review. England, Cambridge
349. Chiang S, Albright CE (1992) CO2 laser beam - Materials interactions in the welding of mild steel part 2: effects of plume suppression on heat transfer efficiencies in argon - shielded laser beam welding. Laser Inst Am 75:491–522
350. Rockstroh TJ, Mazumder J (1987) Spectroscopic studies of plasma during cw laser materials interaction. J Appl Phys. 61(3):917–923
351. Kawahito Y, Matsumoto N, Mizutani M, Katayama S (2008) Characterisation of plasma induced during high power fibre laser welding of stainless steel. Sci Technol Weld Join. 13(8):744–748
352. Kawahito Y, Kinoshita K, Matsumoto N, Mizutani M, Katayama S (2008) Effect of weakly ionised plasma on penetration of stainless steel weld produced with ultra high power density fibre laser. Sci Technol Weld. Join. 13(8):749–753
353. Cai Y, Heng H, Li F, Wang M (2018) The influences of welding parameters on the metal vapor plume in fiber laser welding based on 3D reconstruction. Opt Laser Technol. 107:1–7
354. Pang S, Hirano K, Fabbro R, Jiang T (2015) Explanation of penetration depth variation during laser welding under variable ambient pressure. J Laser Appl. 27(2)
355. Shcheglov PY, Uspenskiy SA, Gumenyuk AV, Petrovskiy VN, Rethmeier M, Yermachenko VM (2011) Plume attenuation of laser radiation during high power fiber laser welding. Laser Phys. Lett. 8(6):475–480
356. Reisgen U, Olschok S, Jakobs S, Turner C (2016) Laser beam welding under vacuum of high grade materials. Weld. World 60(3):403–413
357. Greses J, Hilton PA, Barlow CY, Steen WM (2004) Plume attenuation under high power Nd:yttritium–aluminum–garnet laser welding. J Laser Appl. 16(1):9–15
358. Shcheglov P (2012) Study of vapour-plasma plume during high power fiber laser beam influence on metals. PhD Thesis. BAM Bundesanstalt für Materialforschung und-prüfung
359. Schneider A, Gumenyuk A, Lammers M, Malletschek A, Rethmeier M (2014) Laser beam welding of thick titanium sheets in the field of marine technology. Phys. Procedia 56:582–590
360. Baardsen EL, Schmatz DJ, Bisaro RE (1973) High Speed Welding of Sheet Steel with a CO2 Laser. Weld J. (4):226–228
361. Ai Y et al (2017) The prediction of the whole weld in fiber laser keyhole welding based on numerical simulation. Appl Therm Eng. 113:980–993
362. Fuerschbach PW, Norris JT, He X, Debroy T (2003) Understanding metal vaporization from laser welding. Sandia National Laboratories
363. Suder WJ, Williams SW (2012) Investigation of the effects of basic laser material interaction parameters in laser welding. J Laser Appl. 24(3):1–10
364. Suder W, Williams S (2010) Parameter selection in laser welding using the power factor concept. 29th Int. Congr. Appl. Lasers Electro-Optics, ICALEO 2010 - Congr. Proc. 103
365. Ayoola WA, Suder WJ, Williams SW (2017) Parameters controlling weld bead profile in conduction laser welding. J. Mater. Process. Technol. 249:522–530
366. Suder WJ, Williams S (2014) Power factor model for selection of welding parameters in CW laser welding. Opt Laser Technol. 56: 223–229
367. Börner C, Krüssel T, Dilger K (2013) Process characteristics of laser beam welding at reduced ambient pressure. In: High-power laser materials processing: lasers, beam delivery, diagnostics, and applications II, 86030M
368. Katayama S, Kobayashi Y, Seto N, Mizutani M, Matsunawa A (2001) Effect of vacuum on penetration and defects in laser welding. J Laser Appl. 13(5):187–192
369. Jiang M, Chen X, Chen Y, Tao W (2019) Increasing keyhole stability of fiber laser welding under reduced ambient pressure. J Mater Process Technol. 268:213–222
370. Olsen FO, Alting L (1995) Pulsed Laser Materials Processing, ND-YAG versus CO2 Lasers. CIRP Ann. - Manuf. Technol. 44(1):141–145
371. Torkamany MJ, Hamedi MJ, Malek F, Sabbaghzadeh J (2006) The effect of process parameters on keyhole welding with a 400 W Nd:YAG pulsed laser. J Phys D Appl Phys. 39(21): 4563–4567
372. Assunção E, Williams S (2013) Comparison of continuous wave and pulsed wave laser welding effects. Opt Lasers Eng. 51(6): 674–680
373. Fuerschbach PW, Eisler GR (2002) Effect of laser spot weld energy and duration on melting and absorption. Sci Technol Weld Join. 7(4):241–246
374. Grünenwald S, Unt A, Salminen A (2018) Investigation of the influence of welding parameters on the weld geometry when welding structural steel with oscillated high-power laser beam. Procedia CIRP 74:461–465
375. Köhler M, Tóth T, Kreybohm A, Hensel J, Dilger K (2020) Effects of reduced ambient pressure and beam oscillation on gap bridging ability during solid-state laser beam welding. J Manuf Mater Process. 4(40):1–13
376. Müller A, Goecke SF, Rethmeier M (2018) Laser beam oscillation welding for automotive applications. Weld. World 62(5):1039–1047
377. Fetzer F, Sommer M, Weber R, Weberpals JP, Graf T (2018) Reduction of pores by means of laser beam oscillation during remote welding of AlMgSi. Opt. Lasers Eng. 108:68–77
378. Wang L, Gao M, Zhang C, Zeng X (2016) Effect of beam oscillating pattern on weld characterization of laser welding of AA6061-T6 aluminum alloy. Mater Des. 108:707–717
379. Mrňa L, Horník P, Jedlička P, Pavelka J (2017) Study of laser wobbling welding process through the radiation of plasma plume. In: *Lasers in Manufacturing Conference 2017*
380. Hann DB, Iammi J, Folkes J (2010) Keyholing or Conduction – Prediction of Laser Penetration Depth. Proc. 36th Int. MATADOR Conf 22:309–317
381. Courtois M, Carin M, Le Masson P, Gaied S, Balabane M (2013) A new approach to compute multi-reflections of laser beam in a keyhole for heat transfer and fluid flow modelling in laser welding. J Phys D Appl Phys. 46(50)
382. Coroado J et al (2017) Fundamental understanding of the interaction of continuous wave laser with aluminium. Int J Adv Manuf Technol 93:3165–3174
383. Norris JT, Robino CV, Hirschfeld DA, Perricone MJ (2011) Effects of laser parameters on porosity formation: Investigating millimeter scale continuous wave Nd:YAG laser welds. Weld J. 90(10):198s–204s
384. Blecher JJ, Palmer TA, Debroy T (2016) Porosity in thick section alloy 690 welds - Experiments, modeling, mechanism, and remedy. Weld J. 95(1):17s-26s
385. Matsunawa A, Do Kim J, Katayama S (1997) Porosity formation in laser welding - mechanisms and suppression methods. Laser Inst. Am. Proc. 83(2)
386. Gong H, Rafi K, Gu H, Starr T, Stucker B (2014) Analysis of defect generation in Ti-6Al-4V parts made using powder bed fusion additive manufacturing processes. Addit Manuf 1–4:87–98
387. Tammas-Williams S, Zhao H, Léonard F, Derguti F, Todd I, Prangnell PB (2015) XCT analysis of the influence of melt strategies on defect population in Ti-6Al-4V components

manufactured by Selective Electron Beam Melting. Mater. Charact. 102:47–61
388. Ion JC (2000) Laser beam welding of wrought aluminium alloys. Sci. Technol. Weld. Join. 5(5):265–276
389. Zhang J, Weckman DC, Zhou Y (2008) Effects of temporal pulse shaping on cracking susceptibility of 6061-T6 aluminum Nd: YAG laser welds. Weld. J. (Miami, Fla) 87(1):18s–30s
390. Katayama S, Yohei A, Mizutani M, Kawahito Y (2011) Development of deep penetration welding technology with high brightness laser under vacuum. Phys Procedia 12:75–80
391. Luo Y, Tang X, Lu F, Chen Q, Cui H (2015) Effect of subatmospheric pressure on plasma plume in fiber laser welding. J Mater Process Technol. 215(1):219–224
392. Kawahito Y, Mizutani M, Katayama S (2007) Elucidation of high-power fibre laser welding phenomena of stainless steel and effect of factors on weld geometry. J Phys D Appl Phys. 40(19):5854–5859
393. Albright CE, Chiang S (1988) High-Speed Laser Welding Discontinuities. J Laser Appl. 1(1):18–24
394. Arata Y, Abe N, Oda T (1985) Fundamental Phenomena in High Power CO2 Laser (Report II) : Vacuum Laser Welding. Trans JWRI
395. Börner C, Dilger K, Rominger V, Harrer T, Krüssel T, Löwer T (2011) Influence of ambient pressure on spattering and weld seam quality in laser beam welding with the solid-state laser. 30th Int. Congr. Appl. Lasers Electro-Optics, ICALEO 2011 (614):621–629
396. Jiang M, Tao W, Chen Y (2017) Laser welding under vacuum: a review. Appl. Sci. 7(909):1–17
397. Elmer JW, Vaja J, Carlton HD (2016) The effect of reduced pressure on laser keyhole weld porosity and weld geometry in commercially pure titanium and nickel. Weld. J. 95(11):419s-430s
398. Jiang M, Tao W, Wang S, Li L, Chen Y (2017) Effect of ambient pressure on interaction between laser radiation and plasma plume in fiber laser welding. Vacuum 138:70–79
399. Reisgen U, Olschok S, Holtum N, Jakobs S (2017) Laser beam welding in mobile vacuum. In: Lasers in Manufacturing Conference 2017
400. Schneider A, Gumenyuk A, Rethmeier M (2015) Mobile Vacuum in Pocket Format. Laser Tech. J. 12(4):43–46
401. Chiang S, Albright C (1993) The limit of joint penetration in high energy density beam welding. Weld J. 72(3):118s–121s
402. Duocastella M, Arnold CB (2012) Bessel and annular beams for materials processing. Laser Photonics Rev. 6(5):607–621
403. Lachenberg K, Hochanadel P, Elmer JW (2011) Design considerations for electron beam welding. In: Lienert T, Siewert T, Babu S, Acoff V (eds) ASM handbook, volume 6A, welding fundamentals and processes, vol 6A. ASM International, pp 532–539
404. Pierce SW, Burgardt P (2014) Evaluation of two devices for electron beam profiling. Los Alamos National Laboratory
405. International Standards Organization (2005) ISO 11146-1:2005 Lasers and laser-related equipment – Test methods for laser beam widths, divergence angles and beam propagation ratios – Part1: Stigmatic and simple astigmatic beams. International Standards Organization
406. Koglbauer A (2018) More Than Beam Profiling. Laser Tech. J. 15(3):40–44
407. Palmer TA, Hochanadel PW, Lachenburg K (2011) Quality control of electron beams and welds. In: Lienert T, Siewert T, Babu S, Acoff V (eds) ASM handbook, volume 6A, welding fundamentals and processes, vol 6A. ASM International, pp 548–555
408. Palmer TA, Elmer JW (2008) Improving process control in electron beam welding using the enhanced modified faraday cup. J. Manuf. Sci .Eng. Trans. ASME 130(4):0410081–04100815
409. Kaur A, Ribton C, Balachandaran W (2015) Electron beam characterisation methods and devices for welding equipment. J Mater Process Technol. 221:225–232
410. Dilthey U, Goumeniouk A, Nazarenko OK, Akopjantz KS (2001) Mathematical simulation of the influence of ion-compensation, self-magnetic field and scattering on an electron beam during welding. Vacuum 62:87–96
411. Sanderson A, Adams MJ (1970) Electron Beam Welding US 3, 534,387
412. Hicken G, Giedt W, Bentley A (1991) Correlation of joint penetration with electron beam current distribution. Weld J. 70(3):69
413. Prudnikov IA, Toropov AS, Chickikalov YF, Khokhryakov IV (1974) Device for Determination of Charged Particle Beam Profile and Position. Nucl. Instruments Methods 14:101–104
414. Ragheb M, Zakhary S (2000) Study of the electron beam diagnostics and beam waist. Radiat Phys Chem. 58(1):1–8
415. Dilthey U, Goumeniouk A, Böhm S, Welters T (2001) Electron beam diagnostics: a new release of the diabeam system. Vacuum 62(2–3):77–85
416. W. H. Giedt and R. Campiotti (1996) Method of automatic measurement and focus of an electron beam apparatus therefor. US 5, 843,036
417. Krishnan S, Bindra KS, Oak SM (2008) A sensitive and high dynamic range cw laser power meter. Rev Sci Instrum. 79(12)
418. Slutzki M (2004) How is laser Power/Energy measurement affected by incidence angle? Appl, Note
419. Holloway CL et al (2018) Measurement of radio-frequency radiation pressure: the quest for a new SI traceable power measurement. In: 2018 international symposium on electromagnetic compatibility (EMC Europe), pp 386–390
420. Williams PA, Rogers K, Hadler JA, Lee R, and Lehman JH (2019) Using photon momentum to measure high CW laser power and pulse energy. In: Proc. SPIE 11033 - high-power, high-energy, and high intensity laser tech IV, V110330A
421. Artusio-Glimpse AB, Ryger I, Azarova NA, Williams PA, Hadler JA, Lehman JH (2020) Miniature force sensor for absolute laser power measurements via radiation pressure at hundreds of watts. Opt Express 28(9):13310–13322
422. Williams PA et al (2019) Radiation-Pressure-Enabled Traceable Laser Sources at CW Powers up to 50 kW. IEEE Trans. Instrum. Meas. 68(6):1833–1839
423. Williams P, Simonds B, Sowards J, Hadler J (2016) Measuring laser power as a force: a new paradigm to accurately monitor optical power during laser-based machining operations. In: Proc. SPIE 9741 - high-power laser mater. Process. Lasers, Beam Deliv. Diagnostics, Appl. V97410L
424. Fuerschbach PW, Norris JT, Dykhuizen RC, Mahoney AR (2004) Development and evaluation of an in-situ beam measurement for spot welding lasers. Weld J 83(5):154s–159s
425. Wang ZY, Liu JT, Hirak DM, Weckman DC, Kerr HW (1993) Determining the Spot Size and Gaussian Distribution Coefficient of Pulsed Laser Beams Using KAPTON Films. J Laser Appl. 5(1): 5–12
426. Kramer R, Hänsel K, Schwede H, Brandl V, Klos M (2002) Logarithmic CMOS camera microscope for beam diagnostics - profiling of high power Q - switch lasers. In: ICALEO 2002 - 21st international congress on applications of laser and electro-optics, congress proceedings, V51778
427. PRIMES GmbH (2018) PRIMES FocusMonitor FM+. Operating manual
428. Green LI, Herrit GL, Reedy HE (2003) New method for in-line beam profiling high-power CO2 lasers with an IR camera-based system. In: Proc. SPIE 4969 - laser resonators and beam control VI
429. Lim GC, Steen WM (1984) Instrument for instantaneous in situ analysis of the mode structure of a high-power laser beam. J. Phys. E. 17:999–1007
430. Wang ZY, Liu JT, Hirak DM, Weckman DC, Kerr HW (1992) Measurement of pulsed laser beam dimensions using KAPTON films. LIA Laser Inst. Am. 74(614):74–83

431. Tapia G, Elwany A (2014) A Review on Process Monitoring and Control in Metal-Based Additive Manufacturing. J. Manuf. Sci. Eng. 136(6)
432. Kaierle S, Ungers M, Franz C, Mann S, Abels P (2010) Understanding the Laser Process. Laser Tech. J. 7(2):49–52
433. You DY, Gao XD, Katayama S (2014) Review of laser welding monitoring. Sci. Technol. Weld. Join. 19(3):181–201
434. Stavridis J, Papacharalampopoulos A, Stavropoulos P (2018) Quality assessment in laser welding: a critical review. Int. J. Adv. Manuf. Technol. 94(5–8):1825–1847
435. Cai W, Wang J, Jiang P, Cao L, Mi G, Zhou Q (2020) Application of sensing techniques and artificial intelligence-based methods to laser welding real-time monitoring: A critical review of recent literature. J. Manuf. Syst. 57:1–18
436. Millon C, Vanhoye A, Obaton A-F, Penot J-D (May 2018) Development of laser ultrasonics inspection for online monitoring of additive manufacturing. *Weld. World* 62(3):653–661
437. Yu JXZ, Webster PJL, Leung BYC, Fraser JM (2010) High-quality percussion drilling of silicon with a CW fiber laser. In: Proc. SPIE 7584 - laser appl. microelectron. optoelectron. Manuf. XV, V75840W
438. Authier N, Touzet E, Lücking F, Sommerhuber R, Bruyere V, Namy P (2020) Coupled membrane free optical microphone and optical coherence tomography keyhole measurements to setup welding laser parameters. In Proc. SPIE 11273 - high-power laser materials processing: applications, diagnostics, and systems IX, V1127308
439. Dorsch F, Braun H, Keßler S, Pfitzner D, Rominger V (2013) Online characterization of laser beam welds by NIR-camera observation. In: Proc. SPIE 8603 - high-power laser materials processing: lasers, beam delivery, diagnostics, and applications II, V86030R
440. Stritt P et al (2016) Comprehensive process monitoring for laser welding process optimization. In: SPIE 9741 - high-power laser mater. Process. Lasers, Beam Deliv. Diagnostics, Appl. V97410Q
441. Zhang Y, You D, Gao X, Katayama S (2019) Online monitoring of welding status based on a DBN model during laser welding. Engineering 5(4):671–678
442. Precitec GmbH & Co. KG. Monitoring and control of welding depth during laser welding [Online]. Available: https://www.precitec.com/laser-welding/products/process-monitoring/precitec-idm/. Accessed 20 Oct 2020
443. IPG Photonics Corporation (2018) LDD-700 inline welding process monitor [Online]. Available: https://www.ipgphotonics.com/en/215/FileAttachment/LDD-700+Application+Note.pdf. Accessed 26 Sept 2020
444. DePond PJ et al (Sep. 2018) In situ measurements of layer roughness during laser powder bed fusion additive manufacturing using low coherence scanning interferometry. Mater. Des. 154(614): 347–359
445. Stadter C, Schmoeller M, Zeitler M, Tueretkan V, Munzert U, Zaeh MF (2019) Process control and quality assurance in remote laser beam welding by optical coherence tomography. J Laser Appl. 31(2):022408
446. Webster PJL et al (2014) Automatic laser welding and milling with in situ inline coherent imaging. Opt. Lett. 39(21):6217–6220
447. Boley M, Webster P, Heider A, Weber R, Graf T (2014) Investigating the keyhole behavior by using x-ray and optical depth measurement techniques. In: ICALEO 2014 - international congress on applications of lasers & electro-optics, pp 426–430
448. Slangen PR, Essaidi Z, Chanut C, Lauret P, Heymes F, Aprin L (2018) Recent developments in high speed imaging and applications in speckle light. In: Proc. SPIE 10834 - VII international conference on speckle metrology, V108340T
449. Photron, "FASTCAM SA-Z." [Online]. Available: https://photron.com/wp-content/uploads/2020/10/SA-Z10.16.2020_LR.pdf. Accessed 15 Nov 2020
450. Haubold MW, Zäh MF (2019) Real-time spatter detection in laser welding with beam oscillation. Procedia CIRP 79(614):159–164
451. Liu T, Hu R, Chen X, Gong S, Pang S (2018) Localized boiling-induced spatters in the high-power laser welding of stainless steel: three-dimensional visualization and physical understanding. Appl. Phys. A 124(9):654
452. Kratzsch C, Abels P, Kaierle S, Poprawe R, Schulz W (2000) Coaxial process control during laser beam welding of tailored blanks. In: SPIE 3888 - high-power lasers manuf
453. Gao X, You D, Katayama S (2012) Infrared image recognition for seam tracking monitoring during fiber laser welding. Mechatronics 22(4):370–380
454. Fiedler W, Drenker A, Kaierle S (2010) Process monitoring and control during hybrid laser-ARC welding of medium section steel sheets. In: ICALEO 2010 - international congress on applications of lasers & electro-optics, pp 78–84
455. AMADA WELD TECH (2019) MM-L300A laser weld monitor [Online]. Available: https://amadaweldtech.com/product/mm-l300/. Accessed 20 Sept 2020
456. Precitec GmbH & Co. KG. Monitoring your laser welding processes in real time [Online]. Available: https://www.precitec.com/laser-welding/products/process-monitoring/laser-welding-monitor/. Accessed 8 Oct 2020
457. Olsson R, Eriksson I, Powell J, Langtry AV, Kaplan AFH (2011) Challenges to the interpretation of the electromagnetic feedback from laser welding. Opt. Lasers Eng. 49(2):188–194
458. Eriksson I, Kaplan AFH (2009) Evaluation of laser weld monitoring - a case study. In: ICALEO 2009 - 28th Int. Congr. Appl. Lasers Electro-Optics, Congr. Proc. 102:1419–1425
459. Xiris automation, microphone for integration with a Xiris weld camera [Online]. Available: https://www.xiris.com/xiris-weldmic/. Accessed 12 Sept 2020
460. Koester LW, Taheri H, Bond LJ, Faierson EJ (2019) Acoustic monitoring of additive manufacturing for damage and process condition determination. In: AIP Conf. Proc. 2102, 38:0200051-0200056
461. Lee C-J, Kim J-D, Kim Y-C (Mar. 2015) Study on monitoring of plasma emission signal in lap welding of Zn coated steel sheet using CO2 laser. Int. J. Precis. Eng. Manuf. 16(3):495–500
462. Eschner N, Weiser L, Häfner B, Lanza G (2020) Classification of specimen density in Laser Powder Bed Fusion (L-PBF) using in-process structure-borne acoustic process emissions. Addit. Manuf. 34:101324
463. Bastuck M, Herrmann H, Wolter B (2016) Acoustic inline process monitoring for laser welding applications. In: 19th world conf. non-destructive test 2016, pp 1–10
464. Kanko JA, Sibley AP, Fraser JM (2016) In situ morphology-based defect detection of selective laser melting through inline coherent imaging. J. Mater. Process. Technol. J. 231:488–500
465. Ji Y, Grindal AW, Webster PJL, Fraser JM (2015) Real-time depth monitoring and control of laser machining through scanning beam delivery system. J. Phys. D. Appl. Phys. 48(15)
466. Fraser JM (2012) Laser process monitoring and automatic control at kHz rates through inline coherent imaging. AIP Conf. Proc. 1464:492–496
467. Schmitt R, Mallmann G, Peterka P (2011) Development of a FD-OCT for the inline process metrology in laser structuring systems. In: Proc. SPIE 8082 - Opt. Meas. Syst. Ind. Insp. VII, 808228
468. Dorsch F et al (2019) Controlling laser processing via optical coherence topography. In: Proc. SPIE 10911 - high-power laser materials processing: applications, diagnostics, and systems VIII, 109110G

469. Webster PJLL, Wright LG, Mortimer KD, Leung BY, Yu JXZZ, Fraser JM (2011) Automatic real-time guidance of laser machining with inline coherent imaging. J. Laser Appl. 23(2):022001
470. Kogel-Hollacher M, André S, Beck T (2018) Low-coherence interferometry in laser processing: a new sensor approach heading for industrial applications. In: Proc. SPIE 10749 - interferometry XIX, 1074912
471. Webster PJL, Leung BYC, Yu JXZ, Anderson MD, Hoult TP, Fraser JM (2010) Coaxial real-time metrology and gas assisted laser micromachining: process development, stochastic behavior, and feedback control. In: Proc. SPIE 7590 - Micromach. Microfabr. Process Technol. XV, 759003
472. Boley M, Fetzer F, Weber R, Graf T (2019) Statistical evaluation method to determine the laser welding depth by optical coherence tomography. Opt. Lasers Eng. 119:56–64
473. Kogel-Hollacher M, André S, Beck T New horizons in laser material processing: how OCT sets new standards. In: Proc. SPIE 10911 - high-power laser materials processing: applications, diagnostics, and systems VIII, 109110F
474. Webster PJL, Wright LG, Mortimer KD, Leung BY, Yu JXZ, Fraser JM (2010) Automatic real-time guidance of laser machining with inline coherent imaging. In: 29th Int. Congr. Appl. Lasers Electro-Optics, ICALEO 2010 Congr. Proc. 103:1386–1393
475. Webster PJL, Yu JXZ, Leung BYC, Wright LG, Mortimer KD, Fraser JM (2010) Inline coherent imaging of laser micromachining. In: 2010 international symposium on optomechatronic technologies, 5687305
476. Mittelstädt C, Mattulat T, Seefeld T, Kogel-Hollacher M (2019) Novel approach for weld depth determination using optical coherence tomography measurement in laser deep penetration welding of aluminum and steel. J. Laser Appl. 31(2):022007
477. Fleming TG, Nestor SGL, Allen TR, Boukhaled MA, Smith NJ, Fraser JM (2020) Tracking and controlling the morphology evolution of 3D powder-bed fusion in situ using inline coherent imaging. Addit. Manuf. 32: 100978
478. Schmoeller M, Stadter C, Liebl S, Zaeh MF (2019) Inline weld depth measurement for high brilliance laser beam sources using optical coherence tomography. J. Laser Appl. 31(2):022409
479. Blecher JJ et al (Oct. 2014) Real time monitoring of laser beam welding keyhole depth by laser interferometry. Sci. Technol. Weld. Join. 19(7):560–564
480. Yun SH, Tearney GJ, de Boer JF, Bouma BE (2004) Motion artifacts in optical coherence tomography with frequency-domain ranging. Opt. Express 12(13):2977
481. Webster PJL, Muller MS, Fraser JM (2007) High speed in situ depth profiling of ultrafast micromachining. Opt. Express 15(23): 14967
482. Wiesner M, Ihlemann J, Müller HH, Lankenau E, Hüttmann G (2010) Optical coherence tomography for process control of laser micromachining. Rev. Sci. Instrum 81(3):033705
483. Smurov I (2001) Pyrometry applications in laser machining. In: Proc. SPIE 4157 - Laser-Assisted Microtechnology 2000, pp 55–66
484. Fossum ER (1997) CMOS Image Sensors: Electronic Camera-On-A-Chip. IEEE Trans. Electron Devices 44(10):1689–1698
485. Harooni M, Carlson B, Kovacevic R (2014) Detection of defects in laser welding of AZ31B magnesium alloy in zero-gap lap joint configuration by a real-time spectroscopic analysis. Opt. Lasers Eng. 56:54–66
486. Kawahito Y (Feb. 2006) In-Process Monitoring and Adaptive Control during Pulsed YAG Laser Spot Welding of Aluminum Alloy Thin Sheets. J. Laser Micro/Nanoengineering 1(1):33–38
487. Schmidt M, Otto A, Kägeler C (2008) Analysis of YAG laser lap-welding of zinc coated steel sheets. CIRP Ann. 57(1):213–216
488. De Bono P, Allen C, D'Angelo G, Cisi A (2017) Investigation of optical sensor approaches for real-time monitoring during fibre laser welding. J. Laser Appl 29(2):022417
489. Schmidt M et al (2007) Process control in laser manufacturing–dream or reality? In: International congress on applications of lasers & electro-optics 1907:1087
490. Kawahito Y (2006) In-process monitoring and adaptive control for laser spot and seam welding of pure titanium. J. Laser Micro/Nanoengineering 1(3):269–274
491. Kawahito Y, Kito M, Katayama S, Nakamura H (2005) In-process monitoring and adaptive control in YAG laser butt micro-welding of titanium. In: 24th Int. Congr. Appl. Lasers Electro-Optics, ICALEO 2005 - Congr. Proc., P504:276–285
492. Geiger M, Kägeler C, Schmidt M (2008) High-power laser welding of contaminated steel sheets. Prod. Eng. 2(3):235–240
493. Zhang Y, Gao X, You D, Ge W (2019) A Low-Cost Welding Status Monitoring Framework for High-Power Disk Laser Welding (December 2018). IEEE Access 7:17365–17376
494. Gökhan Demir A, De Giorgi C, Previtali B (2018) Design and Implementation of a Multisensor Coaxial Monitoring System With Correction Strategies for Selective Laser Melting of a Maraging Steel. J Manuf Sci Eng 140(4):1–14
495. Masinelli G, Le-Quang T, Zanoli S, Wasmer K, Shevchik SA (2020) Adaptive Laser Welding Control: A Reinforcement Learning Approach. IEEE Access 8:103803–103814
496. Liu G, Gao X, You D, Zhang N (2019) Prediction of high power laser welding status based on PCA and SVM classification of multiple sensors. J. Intell. Manuf. 30(2):821–832
497. Kawahito Y, Ohnishi T, Katayama S (2009) In-process monitoring and feedback control for stable production of full-penetration weld in continuous wave fibre laser welding. J. Phys. D. Appl. Phys. 42(8):085501
498. You D, Gao X, Katayama S (2014) Multisensor fusion system for monitoring high-power disk laser welding using support vector machine. IEEE Trans. Ind. Informatics 10(2):1285–1295
499. Kawahito Y, Kawasaki M, Katayama S (2008) In-process monitoring and adaptive control during micro welding with CW fiber laser. J. Laser Micro/Nanoengineering 3(1):46–51
500. Kawahito Y, Kito M, Katayama S (2007) In-process monitoring and adaptive control for gap in micro butt welding with pulsed YAG laser. J. Phys. D. Appl. Phys. 40(9):2972–2978
501. Kawahito Y, Katayama S (2005) In-process monitoring and adaptive control for lap welds of aluminum alloy sheets. In: International congress on applications of lasers & electro-optics, ICALEO 2005 - Congr. Proc. 2305:905–914
502. Norman P, Engström H, Kaplan AFH (2008) Theoretical analysis of photodiode monitoring of laser welding defects by imaging combined with modelling. J. Phys. D. Appl. Phys. 41(19)
503. Bertrand P, Smurov I, Ignatiev M, Grevey D (2003) Application of near infrared pyrometry for CW Nd:YAG laser welding of stainless steel and laser cladding of stellite. Laser Process. Adv. Mater. Laser Microtechnologies 5121(614):346
504. Forien J-B, Calta NP, DePond PJ, Guss GM, Roehling TT, Matthews MJ (2020) Detecting keyhole pore defects and monitoring process signatures during laser powder bed fusion: A correlation between in situ pyrometry and ex situ X-ray radiography. Addit. Manuf. 35:101336
505. Schmailzl A, Quandt B, Schmidt M, Hierl S (2018) In-Situ process monitoring during laser transmission welding of PA6-GF30. Procedia CIRP 74:524–527
506. Xiao X, Liu X, Cheng M, Song L (2020) Towards monitoring laser welding process via a coaxial pyrometer. J. Mater. Process. Technol. 277:116409
507. Smurov I, Doubenskaia M, Zaitsev A (2013) Comprehensive analysis of laser cladding by means of optical diagnostics and numerical simulation. Surf. Coatings Technol. 220:112–121

508. Doubenskaia M, Grigoriev S, Zhirnov I, Smurov I (2016) Parametric analysis of SLM using comprehensive optical monitoring. Rapid Prototyp. J. 22(1):40–50
509. Mamuschkin V, Haeusler A, Engelmann C, Olowinsky A, Aehling H (2017) Enabling pyrometry in absorber-free laser transmission welding through pulsed irradiation. J. Laser Appl. 29(2):022409
510. Köhler H, Thomy C, Vollertsen F (2016) Contact-less temperature measurement and control with applications to laser cladding. Weld. World 60(1):1–9
511. Ignatiev M, Smurov IY, Flamant G, Senchenko VN, Dozhdikov VS (1997) Surface Temperature Monitoring During Pulsed Laser, Electron Beam and Plasma Action. High Temp. Mater. Process.: 109–123
512. Cho C-H, Hsieh Y-C, Chen H-Y (2015) Welding pool measurement using thermal array sensor. In: Proc. SPIE 9609 - infrared sensors, devices, Appl. V, 960912
513. Mrna L, Sarbort M, Rerucha S, Jedlicka P (2017) Autocorrelation analysis of plasma plume light emissions in deep penetration laser welding of steel. J. Laser Appl. 29(1):012009
514. Kaplan AFH (2015) Local flashing events at the keyhole front in laser welding. Opt. Lasers Eng. 68:35–41
515. You D, Gao X, Katayama S (2014) Monitoring of high-power laser welding using high-speed photographing and image processing. Mech. Syst. Signal Process. 49(1–2):39–52
516. Lu R, Wei H, Li F, Zhang Z, Liang Z, Li B (2020) In-situ monitoring of the penetration status of keyhole laser welding by using a support vector machine with interaction time conditioned keyhole behaviors. Opt. Lasers Eng. 130
517. Dorsch F, Braun H, Keßler S, Pfitzner D, Rominger V (2014) Online NIR diagnostic of laser welding processes and its potential for quality assuring sensor systems. In: Proc. SPIE 8963 - high-power laser materials processing: lasers, beam delivery, diagnostics, and applications III, 89630R
518. Kim C-H, Ahn D-C (2012) Coaxial monitoring of keyhole during Yb:YAG laser welding. Opt. Laser Technol. 44(6):1874–1880
519. Lee S, Ahn S, Park C (2014) Analysis of Acoustic Emission Signals During Laser Spot Welding of SS304 Stainless Steel. J. Mater. Eng. Perform. 23(3):700–707
520. Luo Y, Zhu L, Han J, Xie X, Wan R, Zhu Y (2019) Study on the acoustic emission effect of plasma plume in pulsed laser welding. Mech. Syst. Signal Process. 124:715–723
521. Farson DF (2000) Progress in real time laser process monitoring: Theory and practice. Sci. Technol. Weld. Join. 5(3):194–201
522. Fang C-K, Kannatey-Asibu E, Barber JR (1997) Far-field initial response of acoustic emission from cracking in a weldment. J. Manuf. Sci. Eng. 119(3):281–289
523. Farson DF, Ali A, Li XC (1999) Laser weld penetration monitoring with multiple emission signal measurements. J. Laser Appl. 11(2):47–53
524. Sun A, Asibu EK, Gartner M (2002) Real-time monitoring of laser weld penetration using sensor fusion. J. Laser Appl. 14(2):114–121
525. Wasmer K et al (2018) Laser processing quality monitoring by combining acoustic emission and machine learning: A high-speed X-ray imaging approach. Procedia CIRP 74:654–658
526. Shevchik S et al (2020) Supervised deep learning for real-time quality monitoring of laser welding with X-ray radiographic guidance. Sci. Rep. 10(1):3389
527. Miyazaki T, Yoshioka S, Shirai Y, Kanekama N, Kimura T, Taniguchi N (1985) Monitoring Electron Beam Machining by Generated Acoustic Emission. CIRP Ann. 34(1):503–506
528. Shevchik SA et al (2019) Laser Welding Quality Monitoring via Graph Support Vector Machine With Data Adaptive Kernel. IEEE Access 7:93108–93122
529. Arnot RS, Albright CE (1983) Plasma plume effects in pulsed carbon dioxide laser spot welding. In: International congress on applications of lasers & electro-optics, ICALEO 1983 - Congr. Proc. 38:51–58
530. Ancona A, Spagnolo V, Lugarà PM, Ferrara M (2001) Optical sensor for real-time monitoring of CO2 laser welding process. Appl. Opt. 40(33):6019
531. Sibillano T et al (2012) Spectroscopic closed loop control of penetration depth in laser beam welding process. In: Proc. SPIE 8239 - high power laser mater. process. lasers, beam deliv. diagnostics, appl., 82390S
532. Sibillano T et al (2012) Spectroscopic monitoring of penetration depth in CO2 Nd:YAG and fiber laser welding processes. J. Mater. Process. Technol 212(4):910–916
533. Sibillano T, Ancona A, Berardi V, Lugarà PM (2005) Correlation analysis in laser welding plasma. Opt. Commun. 251(1–3):139–148
534. Zhang Y, Zhang C, Tan L, Li S (2013) Coaxial monitoring of the fibre laser lap welding of Zn-coated steel sheets using an auxiliary illuminant. Opt. Laser Technol. 50:167–175
535. Kong F, Ma J, Carlson B, Kovacevic R (2012) Real-time monitoring of laser welding of galvanized high strength steel in lap joint configuration. Opt. Laser Technol. 44(7):2186–2196
536. Liu W, Liu S, Ma J, Kovacevic R (2014) Real-time monitoring of the laser hot-wire welding process. Opt. Laser Technol. 57:66–76
537. Zhang YM, Zhang SB, Liu YC (2001) A plasma cloud charge sensor for pulse keyhole process control. Meas. Sci. Technol. 12(8):1365–1370
538. Lu W, Zhang YM, Emmerson J (2004) Sensing of weld pool surface using non-transferred plasma charge sensor. Meas. Sci. Technol. 15(5):991–999
539. Li L, Brookfield DJ, Steen WM (1996) Plasma charge sensor for in-process, non-contact monitoring of the laser welding process. Meas. Sci. Technol. 7(4):615–626
540. Huang Y, Xu S, Yang L, Zhao S, Liu Y, Shi Y (2019) Defect detection during laser welding using electrical signals and high-speed photography. J. Mater. Process. Technol. 271:394–403
541. Trushnikov D, Belenkiy V, Shchavlev V, Piskunov A, Abdullin A, Mladenov G (2012) Plasma Charge Current for Controlling and Monitoring Electron Beam Welding with Beam Oscillation. Sensors 12(12):17433–17445
542. Lee SH, Mazumder J, Park J, Kim S (2020) Ranked feature-based laser material processing monitoring and defect diagnosis using k-NN and SVM. J. Manuf. Process. 55(2020):307–316
543. Huang Y, Hou S, Xu S, Zhao S, Yang L, Zhang Z (2019) EMD-PNN based welding defects detection using laser-induced plasma electrical signals. J. Manuf. Process. 45:642–651
544. Kuo B-S, Lu M-C (2020) Analysis of a Sound Signal for Quality Monitoring in Laser Microlap Welding. Appl. Sci. 10(6):1934